# THE PHOTOMETRIC VARIABILITY
# OF PLASKETT'S STAR

# LA VARIABILITÉ PHOTOMÉTRIQUE
# DE L'ÉTOILE DE PLASKETT

A Thesis Submitted to the Division of Graduate Studies
of the Royal Military College of Canada
by

## Erik Stacey, BScH

In Partial Fulfillment of the Requirements for the Degree of
Master of Science in Physics

October, 2022

*To Szarlotka and Goblin*

# Acknowledgements

Firstly, I'd like to extend my sincere gratitude to my academic supervisor, Dr. Gregg Wade, whose mentorship and guidance has been invaluable to both the research presented in this thesis as well as my professional development as a scientist. I'd also like to thank Dr. Kathryn McWilliams, Dr. Ron Vincent, and Dr. L Sanghalli for coordinating the NSERC CREATE International Space Mission Training Program, which has both funded my research and enabled me to meet and collaborate with many wonderful people. I'm gracious to have had the full support of my parents, Carmen and Roger, who have encouraged me throughout my academic career. Finally, I'd like to extend a special thanks to my partner, Lilianna, who has patiently entertained my tales of trials and tribulations in preparing this work.

# Abstract

HD 47129 (Plaskett's Star) is a double-lined spectroscopic binary that has been historically modelled as an O+O post-Roche-lobe overflow system consisting of two $M \approx 50$ M$_\odot$ stars in an approximately circular 14.4 d orbit. The detection of a magnetic field in the broad-line component of Plaskett's Star was reported by Grunhut et al. (2013), revitalizing interest in this system and establishing this star as the most rapidly rotating known magnetic O-type star by a significant margin. Follow-up observations analyzed by Grunhut et al. (2022) presented strong evidence against significant radial velocity variations of the broad-line component, a result which is incompatible with the historical interpretation of this system as a near-equal-mass binary. This has motivated a fundamental revision of the composition and structure of Plaskett's Star.

Plaskett's Star was recently observed by the Transiting Exoplanet Survey Satellite (TESS), and has archival data collected 10 years prior from the Convection, Rotation, and Planetary Transits (CoRoT) mission. The objective of this work was to perform a self-consistent frequency analysis of these two sets of high-precision satellite photometry in the interest of assessing compatibility between the observed photometric variability and the two current hypotheses for revised models of Plaskett's Star. A Lomb-Scargle-based pre-whitening program implemented in Python was developed and tested for application with the photometric variability of Plaskett's Star. This program identified fourteen significant frequencies in the TESS photometry and fifteen significant frequencies in each of the simple aperture photometry TESS data and the CoRoT data. The dominant source of variability in both datasets was found to be attributable to the rotation of the magnetic star and its co-rotating centrifugal magnetosphere. Variability at the orbital frequency of the system was detected in the CoRoT photometry, however this was not detected in the TESS photometry likely due to its short duration. Frequencies with no known physical origin were detected at 0.63 c/d, 1.10 c/d, 0.71 c/d, and 0.40 c/d in the TESS photometry and at 0.36 c/d in the CoRoT photometry. Potential

physical origins of these frequencies were explored, however ultimately no evidence was found in favour of either hypothesis concerning a revised structure for Plaskett's Star.

# Résumé

HD 47129 (l'étoile de Plaskett) est une binaire spectroscopique à double ligne qui a été historiquement modélisée comme un système de débordement O+O post-Roche-lobe composé de deux étoiles $M \approx 50$ M$_\odot$dans une orbite approximativement circulaire de 14,4 d. La détection d'un champ magnétique dans la composante à large raie de l'étoile de Plaskett a été rapportée par Grunhut et al. (2013), relançant l'intérêt pour ce système et établissant cette étoile comme l'étoile magnétique de type O à rotation la plus rapide connue, et ce, de manière significative. Des observations de suivi analysées par Grunhut et al. (2022) ont présenté des preuves solides contre des variations significatives de la vitesse radiale de la composante à large raie, un résultat qui est incompatible avec l'interprétation historique de ce système comme une binaire de masse presque égale. Cela a motivé une révision fondamentale de la composition et de la structure de l'étoile de Plaskett.

L'étoile de Plaskett a été récemment observée par le Transiting Exoplanet Survey Satellite (TESS) et dispose de données d'archives recueillies 10 ans auparavant par la mission Convection, Rotation et Transits planétaires (CoRoT). L'objectif de ce travail était d'effectuer une analyse de fréquence auto-consistante de ces deux ensembles de photométrie satellitaire de haute précision dans le but d'évaluer la compatibilité entre la variabilité photométrique observée et les deux hypothèses actuelles de modèles révisés de l'étoile de Plaskett. Un programme de préblanchiment basé sur Lomb-Scargle et implémenté en Python a été développé et testé pour être appliqué à la variabilité photométrique de l'étoile de Plaskett. Ce programme a identifié quatorze fréquences significatives dans la photométrie de TESS et quinze fréquences significatives dans chacune des données de photométrie à simple ouverture de TESS et des données CoRoT. La source dominante de variabilité dans les deux ensembles de données est attribuable à la rotation de l'étoile magnétique et à sa magnétosphère centrifuge en co-rotation. La variabilité à la fréquence orbitale du système a été détectée dans la photométrie de CoRoT, cependant elle n'a

pas été détectée dans la photométrie de TESS, probablement en raison de sa courte durée. Des fréquences sans origine physique connue ont été détectées à 0.63 c/d, 1.10 c/d, 0.71 c/d, et 0.40 c/d dans la photométrie TESS et à 0.36 c/d dans la photométrie CoRoT. Les origines physiques potentielles de ces fréquences ont été explorées, mais finalement aucune preuve n'a été trouvée en faveur de l'une ou l'autre des hypothèses concernant une structure révisée de l'étoile de Plaskett.

# Contents

# List of Figures

# List of Tables

# Glossary

**ASAS** All-Sky Automated Survey. 45, 46

**BH** black hole. 3, 21, 87, 89, 91
**BinaMIcS** Binarity and Magnetic Interactions in various classes of Stars. 11
**BLC** broad-line omponent. 14–23, 40, 51, 76, 77, 79, 80, 82, 84, 87, 88, 91, 93, 95, 147
**BRITE** BRIght Target Explorer. 47

**CBV** co-trending basis vector. 34, 36, 37, 118–125
**CCD** charge-coupled device. 25, 33, 34, 40, 122–126
**CNES** Centre National D'études Spatiales. 40
**CNO** carbon-nitrogen-Oxygen. 2, 3
**CoRoT** Convection, Rotation, and Planetary Transits. 13, 23, 24, 40–42, 51–53, 65, 67, 68, 72, 75, 77–79, 82–88, 90, 92, 93, 121, 143, 146

**ESPaDOnS** Echelle SpectroPolarimetric Device for the ObservatioN of Stars. 16, 19, 20, 84, 85, 147

**FFI** full-frame image. 34, 36, 121

**GLS** generalized Lomb-Scargle. 49, 50

**Hipparcos** High Precision PARallax COllecting Satellite. 43, 44, 47
**HR diagram** Hertzsprung-Russell diagram. 2

**LS** Lomb-Scargle. 48–50, 52, 53, 58, 61–64, 79, 135, 136

**MiMeS** Magnetism in Massive Stars. 16
**MS** main sequence. 2–4, 6, 10, 12

**NLC** narrow-line component. 14–16, 19–23, 79, 84, 86–91, 93, 94, 147

**PDC** pre-search data conditioning. 34, 36

**PHOEBE** PHysics Of Eclipsing BinariEs. 94, 95
**PSD** power spectral density. 53
**PyPW** Python program for Pre-Whitening. 52, 64–67, 92

**RLOF** Roche Lobe overflow. 10, 12, 16, 20, 91

**SAP** simple aperture photometry. 25, 34, 36, 67, 68, 71, 74, 77, 79, 82, 83, 118–123, 126, 143, 145
**SLF** stochastic low-frequency. 24, 62–65, 67, 68, 70, 76–80, 83, 88, 92, 93
**SNR** signal to noise ratio. 61, 63, 78, 126

**TESS** Transiting Exoplanet Survey Satellite. 13, 23, 24, 33, 34, 36, 38, 39, 41, 47, 51–53, 56, 58, 64, 65, 67–71, 73, 74, 76–79, 82, 83, 87, 88, 92, 93, 118–126, 143–145
**TPF** target pixel file. 34–38, 121, 127, 130–132

**ZAMS** zero-age main sequence. 2
**ZDI** Zeeman-Doppler Imaging. 17

# 1 Introduction

## 1.1 Massive Stars

Stars are dense astrophysical objects consisting of gravitationally bound plasma supported against collapse by thermal and radiation pressure from nuclear fusion in the stellar core. Stars demonstrate a variety of observable and often inter-dependent properties, which are widely variable between stars and even between evolutionary stages of similar stars. Some particularly important examples of such properties include luminosity, surface temperature, metallicity, and surface gravity. The directly observable properties can yield insight into properties that are not directly measurable. One of the most powerful tools an astronomer has is that of simile; stars with similar basic physical characteristics tend to demonstrate similar behaviours. This is most readily demonstrated with the Sun: solar phenomena are vastly easier to observe in comparison to extrasolar stars, and regular comparisons are drawn between so-called "solar analogs" and the Sun itself (e.g. Willmer, 2018; Messina and Guinan, 2002; Gaidos et al., 2000). In other stellar populations, easily observed or otherwise peculiar examples can reveal physical processes that are not apparent in the general population. Therefore, the literature of stellar physics generally relies on studying general trends as well as specific outliers of categorically similar populations of stars.

The most generally significant physical characteristic with respect to determining stellar behaviour is initial mass. With increasing mass, stars exhibit stronger self-gravitation and therefore require a stronger outward radiation pressure to maintain hydrostatic equilibrium. As a consequence, massive stars demonstrate higher core temperatures and pressures, which significantly increases the rate of nuclear fusion such that hydrostatic equilibrium can be established. As a consequence, basic stellar properties such as luminosity, surface/core temperature, and expected lifetime have a strong relationship with stellar mass. Therefore, internal structures and evolutionary behaviours

tend to be similar across stars of similar mass at a given age.

Massive stars are a particularly interesting and influential subset of the stellar population, and are typically defined as stars with masses greater than 8 $M_\odot$. These objects demonstrate luminosities that exceed that of the Sun by four to seven orders of magnitude (Ekström et al., 2012; Crowther et al., 2010). Due to their high core temperatures, hydrogen fusion via the carbon-nitrogen-Oxygen (CNO) cycle is the dominant mechanism of nuclear fusion on the main sequence (MS). This is an efficient fusion process which establishes steep temperature gradients due to its strong dependence on temperature. As a result, massive star cores are unstable to convection. However, their envelopes tend to be highly ionized due to their high temperatures and tend to be radiative, stable, and relatively quiescent. This is a bulk structure that is also shared with intermediate-mass stars (1.5 $M_\odot$> $M$ > 8 $M_\odot$), however these groups are distinguished in their later evolutionary stages.

Massive stellar evolution can be qualitatively understood through studying how massive stars proceed across the Hertzsprung-Russell diagram (HR diagram) during their lifetime. The HR diagram is a common tool used in astronomy to study the properties of stellar populations, and consists of a scatter plot in effective temperature on the X-axis and luminosity on the Y-axis. Fig. 1.1 illustrates evolutionary tracks from numerical simulations performed by Ekström et al. (2012) for stars with masses from 0.8 $M_\odot$ to 120 $M_\odot$. A particularly important property of the HR diagram which is relevant to interpreting evolutionary tracks arises from the Stefan-Boltzmann law. The Stefan-Boltzmann law gives the total wavelength-integrated power per surface area $P^*$ emitted from a black-body with temperature $T$ as

$$P^* = \sigma_s T^4, \tag{1.1}$$

where $\sigma_s$ is the Stefan-Boltzmann constant. Multiplying Eq. 1.1 by the surface area $A = 4\pi R^2$ of a spherical star of radius $R$ yields a relationship of total luminosity $L$ with $R$ and $T$ of

$$L \propto R^2 T^4. \tag{1.2}$$

This implies that a change in effective temperature at a given luminosity also requires a change in radius: a cooler star at the same luminosity must necessarily be larger.

As depicted in Fig. 1.1, all stars begin in a roughly diagonal region in the HR diagram known as the zero-age main sequence (ZAMS). All classes of

stars spend the majority of their life on the MS and tend to exhibit structural changes after leaving the MS. As a result, stars that have left the MS are known as "evolved". Massive stars demonstrate luminosities that are several orders of magnitude higher than solar-like stars, and as a result demonstrate lifetimes of order millions to tens of millions of years (see Sect. 30.3 of Kippenhahn et al., 2012), with less than 10% of that time being spent as evolved stars (Langer, 2012).

As they evolve across the MS, massive stars tend to slowly increase in luminosity and radius. Once leaving the MS, massive stars rapidly proceed towards significantly lower surface temperatures as a result of their expansion, and those with masses greater than approximately 15 $M_\odot$ maintain their MS luminosity during their post-MS evolution. From Fig. 1.1, massive stars decrease in temperature by up to approximately an order of magnitude in their post-MS evolution. By Eq. 1.2, a decrease in temperature by one order of magnitude implies an increase in radius by two orders of magnitude. Therefore, evolved massive stars are aptly referred to as "giants" or, in the case of the most luminous examples, "supergiants". At masses of around 1.2 $M_\odot$ and greater, CNO cycling becomes a significant mechanism for core hydrogen fusion which produces enhancements in nitrogen in the core. Physical processes in highly evolved stars can bring this excess nitrogen to the surface, which is reflected in the abundances depicted in Fig. 1.1 for all stars where CNO cycling is significant.

By definition, evolved stars have exhausted their core hydrogen and halted core hydrogen fusion. At this point, they exhibit core helium fusion to carbon and oxygen (as well as envelope hydrogen fusion) to maintain hydrostatic equilibrium. Uniquely, massive stars establish sufficient core temperature to continue nuclear fusion beyond carbon and oxygen up to iron and nickel (beyond which fusion becomes energetically disfavoured). As a result, evolved massive stars are internally structured as stratified layers where, from the surface to the core, progressively heavier elements are fused (Woosley et al., 2002; Kippenhahn et al., 2012). An example schematic of this structure is depicted in Fig. 1.2. This process naturally produces a growing, inert iron core supported against collapse by electron degeneracy pressure. Once the core becomes sufficiently massive to overcome the electron degeneracy pressure, a core collapse supernova occurs leaving behind either a neutron star or black hole (BH) (Woosley et al., 2002).

The evolutionary tracks presented in Fig. 1.1 are specific to the case of
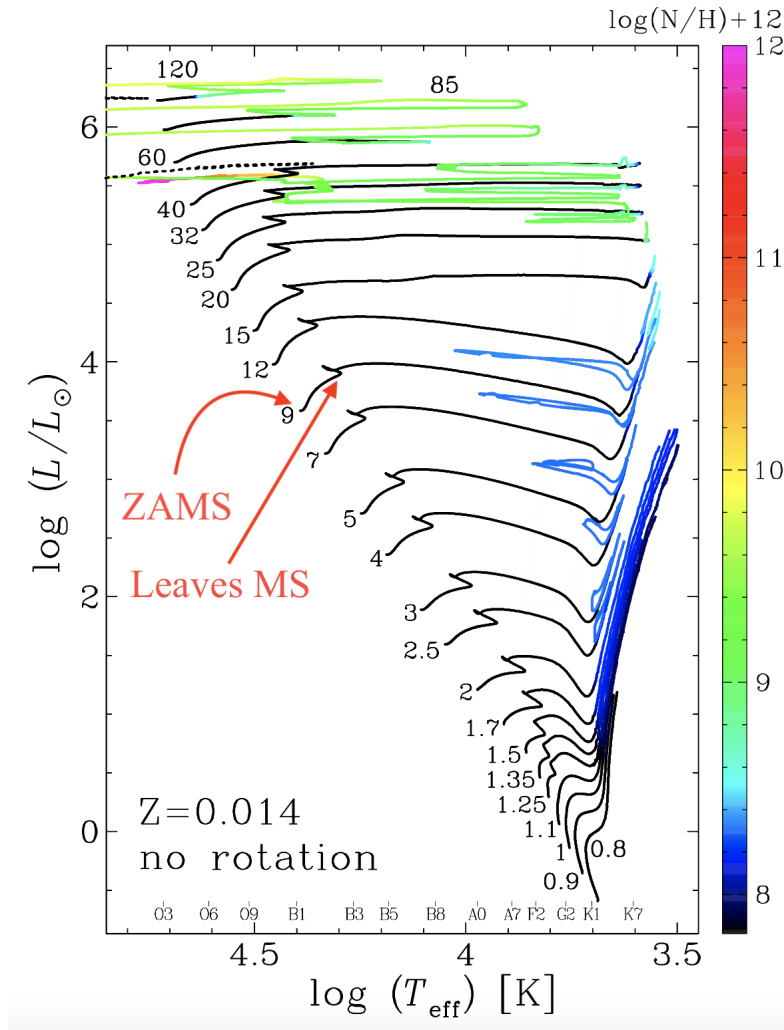
Figure 1.1: Theoretical evolutionary tracks of non-rotating stars with various masses. The line colour gives the logarithmic surface nitrogen abundance relative to hydrogen, which has an abundance of 12 on this scale. Approximate MS spectral types are indicated along the bottom axis. This figure was adapted from the original published by Ekström et al. (2012).
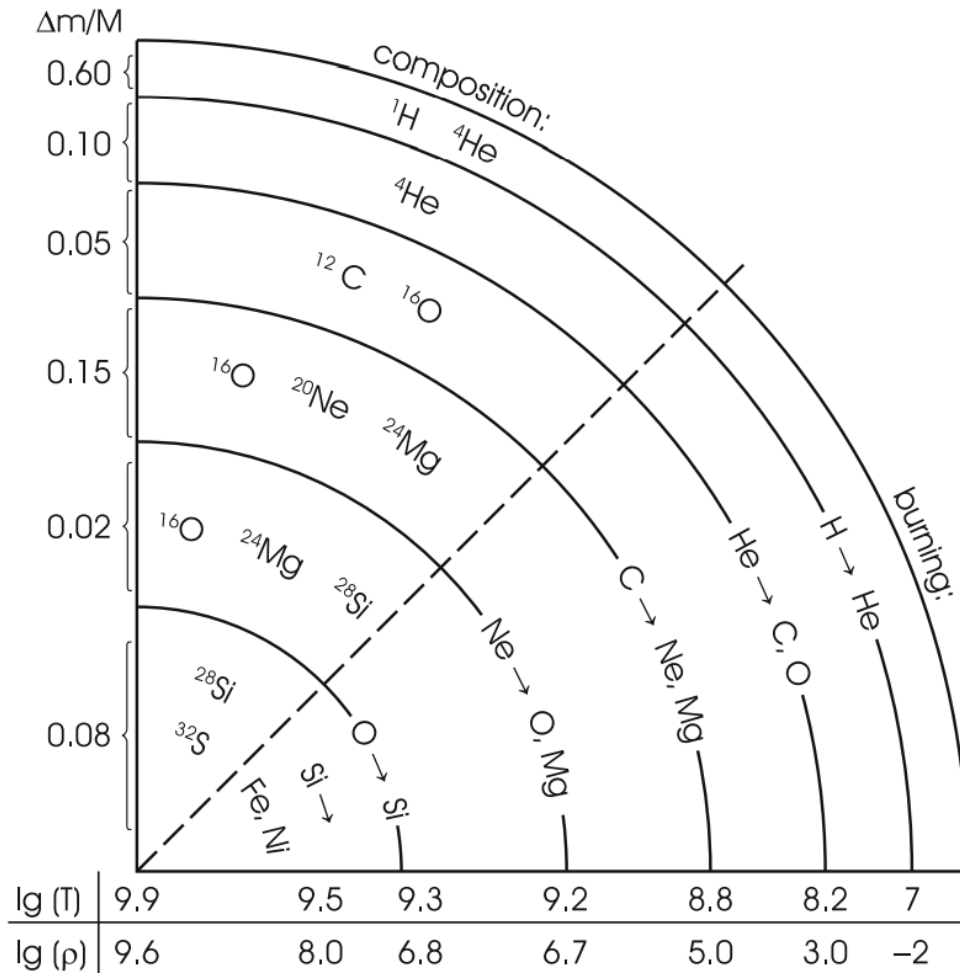
Figure 1.2: From Kippenhahn et al. (2012), the internal composition and nuclear processes of a highly evolved massive star. Along the horizontal axis, typical logarithmic (base 10) temperatures (K) and pressures (g/cm$^3$) are denoted. The vertical axis indicates the fractional mass of each layer.

non-rotating, single stars with the specified metallicity. In reality, massive stars exist in a wide variety of conditions with a diverse range of basic stellar properties. Several of these properties are known to affect their evolution and some examples in literature include rotation (Maeder and Meynet, 2000; Ekström et al., 2012), binarity (see Sect. 1.1.4 Hurley et al., 2002), magnetism (Keszthelyi et al., 2019), metallicity (Heger et al., 2003; Ekström et al., 2012), and mass loss (Chiosi and Maeder, 1986; Smith, 2014). Of these, it's important to emphasize the role of binarity in stellar evolution as the majority of massive stars are thought to interact with a binary companion during their lifetime. The evolutionary implications of this are discussed in detail in Sect. 1.1.4.

Massive stars are known to synthesize elements up to and including those in the iron group in their post-MS evolution (Kippenhahn et al., 2012). However, it has become clear that their concluding supernovae are likely the principal mechanism of nucleosynthesis for elements heavier than the iron group in the Universe (through the S and R processes; Thielemann et al., 2018). This matter is introduced to the intergalactic medium either by stellar winds (see Sect. 1.1.3) or supernovae, and massive stars serve a prolific role in enriching the interstellar medium. Finally, their extreme luminosities tend to ionize material in their local environment and through supernovae they interact dynamically with galactic material. For the reasons discussed here and multiplied by their short lifetimes, massive stars are known to play a significant role in galactic evolution through their own evolutionary processes (Grisdale, 2017; Zhang, 2018). Despite this, massive stellar evolution is highly complex and many aspects still remain poorly understood (see review by Langer, 2012). Nevertheless, evolved massive stars have been shown to exhibit significant influence over their environments and host galaxies, and the importance of further developing an understanding of their evolutionary processes is clear.

### 1.1.1 Magnetic Fields of Massive Stars

Stellar matter is generally composed of dynamically active plasma and it is therefore unsurprising that magnetism plays an important role in stellar behaviour and evolution. The first observation of a stellar magnetic field was made by Hale (1908), who observed circular polarization in sunspots on the surface of the Sun and determined the presence of magnetic fields of approximately 3 kG. Sunspots, alongside solar activity like flares and outbursts, are now known to be a consequence of magnetic fields generated in the envelope and surface layers through small-scale convective dynamos and large-scale shear dynamos. Behaviour associated with magnetism in our sun has also been

observed in other cool stars (Donati et al., 2000; Berdyugina and Järvinen, 2005; Donati et al., 2008) and these stars are known to exhibit magnetic fields that are qualitatively similar to those of the Sun (Donati and Landstreet, 2009). As a consequence of their dynamo origin, these fields are topologically complex, locally strong, highly variable, and demonstrate a strong dependence on the rotation rate of the star.

The first detection of an extrasolar magnetic field is attributed to Babcock (1947), who directly observed Zeeman splitting in spectral lines to infer the presence of a kG-order magnetic field in the chemically peculiar A2 star 78 Vir, which Babcock interpreted to be fundamentally different from the solar magnetic fields observed by Hale. Babcock's interpretation was correct and magnetic fields of intermediate and high-mass stars are now understood to be (1) topologically simple and global with respect to their host stars, (2) stable on long timescales with no short-term variability, (3) independent of the rotation rate of the star, and (4) oblique to the rotation axis of the star (Donati and Landstreet, 2009). Magnetic fields in OBA stars are also relatively rare and its well established that only approximately 10% of OBA stars host magnetic fields with the properties described above (Alecian et al., 2013; Fossati et al., 2015; Grunhut et al., 2017). Additionally, some A-type stars have been shown to exhibit weak, complex surface magnetic fields. The first star identified to exhibit this phenomenon was Vega (Lignières et al., 2009; Petit et al., 2010). Early-type stars are now thought to exhibit a bimodal distribution of magnetic fields between ultra-weak fields more similar to those of low-mass stars, and the topologically simple and strong fields originally measured by Babcock (1947).

### 1.1.2 The Origin of Magnetic Fields in Massive Stars

While the magnetic fields of cool stars have clear and reasonably well-understood dynamo origins, such a prescription is not suitable for massive stars as they lack the requisite convective envelopes. Early attempts to understand the origins of these magnetic fields were based around dynamos in the convective cores of massive stars, which were shown to be capable of producing strong axisymmetric magnetic fields by Charbonneau and MacGregor (2001). However, these models fell out of favour as it was shown that the transport of magnetic flux from the core to the surface could not be achieved on reasonable timescales (MacGregor and Cassinelli, 2003; MacDonald and Mullan, 2004). Differential rotation-driven shear dynamos were also hypothesized as the ori-

gin of magnetic fields in massive stars (Spruit, 2002), however these dynamos were subject to numerous instabilities (Spruit, 1999; Zahn et al., 2007) which caused many to question the applicability of these models.

The most widely accepted theory for the origin of magnetic fields in hot stars today is the *fossil origin*, where a magnetic field is embedded in the star very early in its lifetime (Braithwaite and Spruit, 2004). The classical fossil-field hypothesis assumes the magnetic fields are the result of flux conservation of a collapsing molecular cloud in the presence of a weak magnetic field. However, this theory fails to account for ultra-weak Vega-like fields. Braithwaite and Cantiello (2013) introduced the concept of "failed" fossil fields to address this problem, hypothesizing that the fossil fields are converted to Vega-like fields by dynamos in subsurface convection zones. Jermyn and Cantiello (2020) showed the subsurface convection processes that destroy fossil fields in the failed fossil model are disrupted for field strengths exceeding 300 G, providing a mechanism for a small fraction of stars to retain their fossil fields as observed. This is particularly consistent with the lack of detections of strong, topologically simple magnetic fields in massive stars with strengths less than approximately 300 G (Aurière et al., 2007; Fossati et al., 2015).

Recently, it has been hypothesized that stellar mergers may be responsible for magnetic fields in massive stars (Schneider et al., 2019). A major motivation of this hypothesis is that magnetic massive stars and binary merger products are thought to occur with similar incidence rates (de Mink et al., 2014). This is further supported by the low incidence rate of magnetic fields in massive binaries (see Sect. 1.1.5). Schneider et al. (2019) conducted magnetohydrodynamic simulations of binary mergers and showed them to be capable of producing strong magnetic fields. However, additional evidence supporting this hypothesis is limited.

### 1.1.3  Stellar Winds and Magnetospheres

Stars are generally assumed to be in hydrostatic equilibrium, at least on a macroscopic scale. In reality, phenomena that clearly arise from a departure from hydrostatic equilibrium conditions are regularly observed. One such example is that of stellar winds, which are material flows with high outward radial velocities originating from near the stellar surface. The winds of massive stars are primarily driven by the absorption of ultraviolet photons by metallic species in the outer layers of the star (Castor et al., 1975). Winds arising from this phenomenon are called "line-driven winds", and are a key

part of massive star evolution as they carry away both mass and angular momentum from the star (Cassinelli, 1979; Smith, 2014).

In non-magnetic stars, material in the stellar atmosphere is affected by inward gravitational force and outward gas pressure, radiative pressure, and centrifugal forces. The addition of a magnetic field extending above the stellar surface introduces another force which dynamically interacts with the material and establishes structures of ionized plasma above the stellar surface called magnetospheres. The first type of magnetosphere identified in massive stars is the "dynamical" magnetosphere, which sees wind-driven material channeled along magnetic field lines from the surface and returning to the surface along closed magnetic field lines (Townsend and Owocki, 2005). Early attempts at modelling dynamical magnetospheres proceeded according to the rigidly rotating magnetosphere model, where it was assumed that the magnetosphere corotated rigidly with its host star (Townsend et al., 2007). As discussed by ud-Doula (2021), this is a reasonable approximation at high rates of rotation, however at lower rates of rotation this assumption yields simpler structures than more complex treatments.

In the most rapidly rotating stars, the centrifugal force on corotating magnetically channeled wind plasma can approach and exceed the binding force from the magnetic field. This introduces the "centrifugal" magnetosphere, where material accumulates in dynamical potential minima along the paths of magnetically confined winds (Petit et al., 2013). Approximately 25% of magnetic B stars possess centrifugal magnetospheres (Shultz et al., 2014), however there is only one O-type star known to host such a structure - Plaskett's Star, the subject of this thesis. To understand the rarity of magnetic O-stars hosting centrifugal magnetospheres, it's necessary to introduce the concept of magnetic braking. The magnetic fields of massive stars exert a torque on the stellar wind, which tends to spin down the star over time (Friend and MacGregor, 1984; ud-Doula et al., 2009). Due to their substantially higher mass loss rates, this effect is much stronger for O-type stars than for B-type stars. As a consequence, magnetic O-type stars shed angular momentum very quickly and tend to be slowly rotating. Plaskett's Star is highly anomalous in this respect, as further discussed in Sect. 2.

### 1.1.4 Binarity of Massive Stellar Systems

A particularly interesting characteristic of massive stellar systems, particularly those of O and B spectral types, is their tendency to exist in multiple star systems. Sana (2016) presented a summary of the results of several recent multiplicity surveys (2012+) and computed binary fractions for each of them. They found binary fractions of approximately 0.19 for late B-type stars (B4-B9) and 0.46 for early B-type stars (B0-B3) observed by Chini et al. (2012). O-type stars demonstrated even higher binary fractions ranging from approximately 0.42 to 0.69 in their own sample as well as the samples of Chini et al. (2012); Sana et al. (2012); Sota et al. (2014); Kobulnicky et al. (2014); Aldoretta et al. (2015).

Having established binarity to be very common amongst massive stars, it's pertinent to discuss the evolutionary implications of the presence of a binary companion. The most significant consequence of binary interaction is mass transfer, which typically occurs as a consquence of ordinary single-star evolution (within a binary context). To understand this, it's necessary to define the *Roche Lobe* of a star with a binary companion, which is the teardrop-shaped region around the star where material is stably gravitationally bound. Stellar evolution can either cause the expansion of the star or contraction of its Roche Lobe such that stellar material becomes gravitationally unbound and mass transfer to its companion occurs (see reviews by Paczyński, 1971; Thomas, 1977; Vanbeveren et al., 1998). This process is often referred to as a Roche Lobe overflow (RLOF) and is expected to affect the evolution of many binary systems. RLOF can be avoided under certain circumstances (e.g. low metallicities; Song et al., 2016), in which case the mass transfer would be limited to accretion from stellar winds.

The RLOF process imparts significant material and angular momentum to the receiving star, causing substantial mixing of the stellar interior and affecting its evolutionary path (Brott et al., 2011; Sana et al., 2012). The donor star can lose significant mass, in some cases evolving to a compact object (Lauterborn, 1970) and/or triggering a phase of common-envelope evolution with its companion (Taam and Sandquist, 2000). Sana et al. (2012) estimated that 70% of massive stars interact through mass exchange with a companion while on the MS, with 20-30% of these cases leading to mergers and 40-50% of these cases leading to envelope stripping and accretion for O-type stars. It's clear that binary evolution plays a significant role in the evolution of massive star populations as a whole, and the study of massive binary systems is

therefore a key part of understanding both stellar evolution and characterizing how these objects influence their surroundings.

### 1.1.5 Magnetism and Binarity

Binarity has been long understood to have a relationship with magnetism of intermediate and high-mass stars. Particularly, magnetic stars are less likely to belong to a binary system compared to the general non-magnetic population (Abt and Snowden, 1973). For example, no detections were produced in a sample of 200 OBA systems ($\approx$ 400 stars) observed by the Binarity and Magnetic Interactions in various classes of Stars (BinaMIcS) survey (Neiner et al., 2015). Of course, approximately 20 detections would be expected in 200 single-star systems assuming an approximate rate of incidence of magnetic fields of 10%. This has been interpreted as evidence that magnetic fields are generated by stellar mergers, as multiple systems that do not host a merger product would not expected to be magnetic. However this has also been interpreted, in the context of fossil fields, as the shedding of angular momentum by strongly magnetized molecular clouds reducing their likelihood of forming a binary system (Braithwaite, 2014). Nevertheless, there are a handful of known magnetic massive binaries with interesting properties. A particularly pertinent example is $\epsilon$ Lupi, a B+B binary system where both components have been detected as magnetic (Shultz et al., 2015).

### 1.1.6 Synchronization and Circularization in Massive Binaries

Close binary systems are known to exhibit synchronization of rotational periods with the orbital period, as well as the circularization of orbits over time (Plavec, 1970; Levato, 1976; Giuricin et al., 1984). There are two primary theories in the literature for the physics underpinning these phenomena, both of which recognize tidal torquing as the principal method of synchronization. The theory developed by Zahn (1977) interpreted this as damping of tidal distortions in the stellar surface layers. This was described as viscous and radiative damping for convective and radiative envelopes, respectively. The "tidal friction" prescription of Zahn (1977) has challenges with addressing the circularization component of tidal circularization and synchronization. This partially motivated the second theory of Tassoul (1987) and Tassoul (1988), which interpreted the energy dissipation as the interaction of tidal distortions with large-scale meridional flows. The Tassoul (1987)/Tassoul (1988) approach was also motivated by the rapid action of such a mechanism, which

was estimated to operate nearly 3 orders of magnitude faster than those of Zahn (1977). The theoretical predictions of Zahn (1977) have generally been more consistent with observations for early-type main-sequence eclipsing binaries (Pan, 1997; Khaliullin and Khaliullina, 2010).

According to Zahn (1977) the synchronization timescale $t_{\text{sync}}$ for a convective-core star is given in terms of the gravitational constant $G$, the mass of the star $M$, the radius of the star $R$, the mass ratio of the system $q$, the semimajor axis $a$, and the tidal factor $E_2$ by

$$\frac{1}{t_{\text{sync}}} = (5)(2^{5/3}) \left( \frac{GM}{R^3} \right)^{1/2} q(1+q)^{11/6} E_2 \left( \frac{R}{a} \right)^{21/2}. \qquad (1.3)$$

The tidal factor $E_2$ is particular to convective-core stars and is dependent on the internal structure of the star. Additionally, it is much more sensitive to the internal structure of the star than the analogous coefficient for stars with convective envelopes. Consequently, as the star evolves and its internal structure changes, the synchronization timescale given by Eq. 1.3 will change dramatically. For a 15 $M_\odot$ star, Zahn (1977) estimated $E_2$ to decrease by approximately 5 orders of magnitude over the main-sequence lifetime of a star, which was partially offset by the predicted increase in radius. Nevertheless, the conclusion of Zahn (1977) was that most of the tidal synchronization tends to occur early in the MS lifetime of the star. This is likely the reason why studies of tidal synchronization for early-type stars in literature tends to focus on main-sequence stars. It's consequently unclear in literature if synchronous rotation can be maintained or quasi-maintained through the post-MS evolution of early-type stars in binary systems. This is particularly relevant to systems that experience a RLOF event during their evolution, due to the expected transfer of angular momentum.

## 1.2 Objectives and Motivations of This Work

The subject of this work is the evolved spectroscopic binary system HD 47129, also known as "Plaskett's Star". This stellar system, historically interpreted as a binary star system containing two $\approx$ 50 $M_\odot$ O-type stars, demonstrates several anomalous properties which are not well understood according to current models. In fact, new observations have been presented by Grunhut et al. (2022) which provide strong evidence against the historical interpretation of this system, and have motivated a fundamental revision of the structure of The Plaskett's Star system. As a result, Plaskett's Star is a particularly in-

teresting example of an evolved, magnetic, binary stellar system which has been identified as a candidate to probe poorly understood aspects of stellar evolution and magnetism in massive stars.

The objective of this work was to provide a comprehensive analysis of the photometric variability of Plaskett's Star in the context of recent discoveries introduced by Grunhut et al. (2022), based principally on the high-resolution satellite photometry collected by the Convection, Rotation, and Planetary Transits (CoRoT) and Transiting Exoplanet Survey Satellite (TESS) missions. More specifically, this work sought to inform the development of a revised model for Plaskett's Star by identifying frequencies of photometric variability, assessing their potential underlying physical sources and ultimately determining compatibility with two new hypothesized models of Plaskett's Star. Plaskett's Star, including its historical and candidate revised models, is discussed in detail in Chapter 2. Chapter 3 describes the photometric data considered or analyzed in this work. A new *Python*-based frequency analysis tool was developed specifically for this work and is detailed in Chapter 4. The frequency analysis process and results are discussed in detail in Chapter 5, and the variability is interpreted in Chapter 6. Finally, a summary is provided in Chapter 7 alongside some discussion of the next steps for this work.

# 2  Plaskett's Star

Plaskett's Star (HD 47129) was first identified as double-lined spectroscopic binary by Canadian astronomer John Stanley Plaskett in 1922 (Plaskett, 1922). The system was observed to demonstrate a nearly circular orbit with an orbital period of approximately 2 weeks and a spectral class between O0 and O5. However, this system attracted Plaskett's attention, and the attention of the broader scientific community, due to its remarkably high mass ($M \sin^3 i = 138.9$ M$_\odot$). Following Plaskett's initial measurements, HD 47129 has now been studied extensively for over 100 years. Despite this, Plaskett's Star remains enigmatic and many aspects of this system are poorly understood, including its fundamental physical composition and configuration.

## 2.1  Historical Model

Plaskett's Star has been historically understood as an, non-eclipsing, near-equal mass O8 III/I + O7.5 III spectroscopic binary with projected total mass of $M \sin^3 i = (92.7 \pm 2.7)$ M$_\odot$ (Linder et al., 2008). The orbit of the system has been described as approximately circular (Stickland, 1987) with an orbital period of $(14.396257 \pm 0.000953)$ days (Linder et al., 2008). The two spectral components appear blended at all orbital phases, however the O7.5 component demonstrates substantial rotational broadening of its spectral lines ($v \sin i = 360 \pm 40$ km/s;  Grunhut et al., 2022) while the lines of the O8 component are comparatively narrow ($v \sin i \approx 60 - 75$ km/s;  Linder et al., 2008). These components will be henceforth referred to as the broad-line omponent (BLC) and narrow-line component (NLC) respectively. Linder et al. (2008) disentangled the BLC and NLC contributions to the composite line profile using the methodology described by González and Levato (2006) and measured the radial velocity variations to be consistent with a near-equal-mass, near-circular binary (see Fig. 2.1).
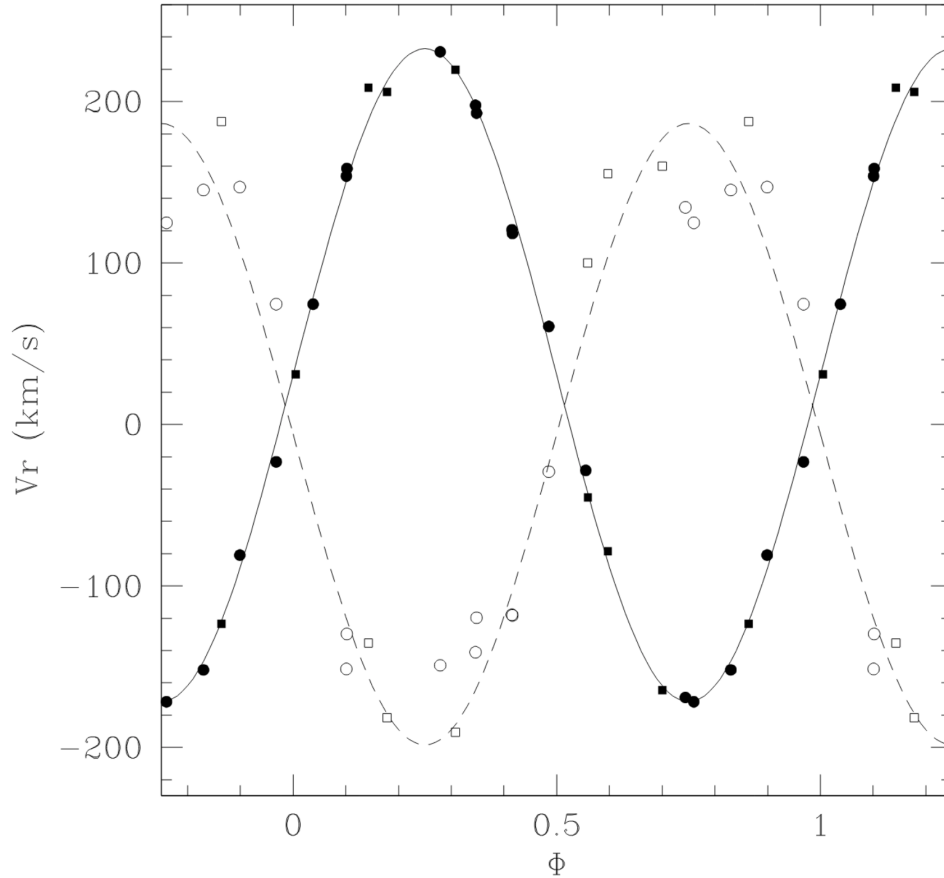
Figure 2.1: The radial velocities measured for both components of Plaskett's Star from Linder et al. (2008) phased according to their reported orbital period. The filled and unfilled points correspond to the NLC and BLC measurements respectively. The circle and square points indicate whether the measurement was from spectra collected with the FEROS or Sophie instrument, respectively. This figure was originally published by Linder et al. (2008).

Plaskett's Star is located in close proximity to the constellation of Monoceros (Mon) in the celestial sphere and is considered a probable member of the Mon OBII association. The Mon OBII association consists of several subgroups of O and B-type stars distributed in and around the Rosette Nebula, thought to exist at a heliocentric distance of 1.4-1.7 kpc (Chen et al., 2007).

Precise parallax measurements by the Gaia space observatory revealed Plaskett's Star to be at a distance of $1.283 \pm 0.122$ kpc, which is consistent with membership in the Mon OBII association.

Linder et al. (2008) measured enhancement in He for both components ($He_{NLC}/He_{\odot} = 1.17 \pm 0.35$, $He_{BLC}/He_{\odot} = 1.76 \pm 0.53$) and strong N enhancement ($N_{NLC}/N_{\odot} = 16.6 \pm 5.0$) in the NLC. They also measured depletions in C ($C_{NLC}/C_{\odot} = 0.2 \pm 0.1$) and Mg ($Mg_{NLC}/Mg_{\odot} = 0.6 \pm 0.2$) for the NLC and in N ($N_{BLC}/N_{\odot} = 0.2 \pm 0.1$) for the BLC. Bagnuolo and Barry (1996) qualitatively assessed N enhancements and C/O depletions for the NLC in optical spectra. Finally, a fractional N overabundance of $N_X/N_{\odot} \approx 6$ was measured in XMM-Newton X-ray spectra by Linder et al. (2006). Linder et al. (2008) concluded this was consistent with their measurements, noting the components could not be separated in the X-ray data and therefore the X-ray measurement pertains to the entire system. Linder et al. (2006) also measured Plaskett's Star to demonstrate an X-ray luminosity of approximately $8.34 \times 10^{32}$ erg/s.

At the time of the publication of Linder et al. (2008), Plaskett's Star was considered to be well understood as a double-line spectroscopic binary in a post-RLOF evolutionary stage, where the NLC had transferred mass to the BLC. In this context, the high rotation of the BLC was attributable to the accumulation of angular momentum during the mass transfer from the NLC. Furthermore, the X-ray luminosity was thought to be the result of wind shocks in regions where the winds of the stars were colliding. This model is now referred to as the *historical model*, for reasons discussed in Sect. 2.1.1.

### 2.1.1 Magnetic Field of Plaskett's Star

Eight spectropolarimetric observations of Plaskett's Star, collected with Echelle SpectroPolarimetric Device for the ObservatioN of Stars (ESPaDOnS) spectropolarimeter at the Canada-France-Hawaii telescope as a part of the Magnetism in Massive Stars (MiMeS) survey (Wade et al., 2016) and analyzed by Grunhut et al. (2013), revealed the presence of a magnetic field in the BLC of Plaskett's Star. Based on the high rate of rotation inferred from its broad spectral lines, Grunhut et al. (2013) hypothesized the BLC to host a centrifugal magnetosphere. A set of 55 follow-up observations collected and analyzed by Grunhut et al. (2022) confirmed this to be the case, making this star the only known O-type star hosting a centrifugal magnetosphere. The rotation period of the BLC was inferred from variability in the mean longitudi-

nal magnetic field and spectral line equivalent widths to be $1.21551^{+0.00028}_{-0.00034}$ d, firmly establishing HD 47129 as the most rapid rotator amongst the 11 known magnetic O-type stars (Grunhut et al., 2017). It's important to emphasize the anomalously high rotation rate of Plaskett's Star compared to other magnetic O-type stars; all other examples demonstrate rotation periods exceeding 7 days with a median rotation period of 68.49 d (Wade and MiMeS Collaboration, 2015). The large number of phase-resolved observations permitted Grunhut et al. (2022) to map the surface magnetic field geometry of the BLC through Zeeman-Doppler Imaging (ZDI) (see Folsom et al., 2018, App. B for ZDI methodology). As perhaps the most major result reported therein, Grunhut et al. (2022) found reasonable fits to the magnetic geometry could only be achieved assuming a constant radial velocity, as opposed to the large-amplitude, sinusoidally variable radial velocity implied by the historical model.

## 2.2 Understanding the Results from ZDI Modelling

The shapes of the magnetic signatures in Stokes V[1] are dependent on the magnetic geometry and the viewing angle of regions where light is emitted in the presence of the magnetic field, which is the operative principle used in ZDI. More specifically, ZDI relies on the simultaneous fitting of many (rotational) phase-resolved Stokes V profiles to infer the underlying magnetic geometry. ZDI is, however, susceptible to overfitting much like any optimization process, particularly when the assumed model doesn't fit the data. The Stokes V profiles will track with the Doppler shifting of their associated Stokes I profiles, which constitutes a critical component of the model when conducting ZDI. If an incorrect assumption is made with respect to the motion of the Stokes I profiles, ZDI is liable to overfit the data by increasing the complexity of the magnetic map. The approach to ZDI taken by Folsom et al. (2018), and consequently Grunhut et al. (2022), generally mitigates this by adopting the maximum entropy technique of Skilling and Bryan (1984).

Magnetic maps produced by Grunhut et al. (2022) with Doppler shifting derived from both the Linder et al. (2008) orbital model and a constant radial velocity are shown in Fig, 2.2. Additionally, the associated fits to the Stokes

---

[1]The Stokes vector is a wavelength-dependent vector describing the absorption and polarization characteristics of light in a spectropolarimetric observaton. Stokes V represents the net circular polarization as a function of wavelength. Stokes I represents the normalized flux as a function of wavelength.

V profiles are shown in Fig. 2.3. The map assuming the Linder et al. (2008) orbital model is clearly substantially more complex than the model assuming a constant radial velocity. Additionally, Grunhut et al. (2022) observed the fits to the Stokes V profiles in the case of the Linder et al. (2008) radial velocities to be poor. On the contrary, the magnetic map produced assuming a constant radial velocity is simple, the fits to the Stokes V profiles were reasonable, and the magnetic geometry is generally consistent with those of other magnetic massive stars. This provided strong evidence *against* significant radial velocity variations for the BLC, and is supported by disentangling of Stokes I profiles (see Sect. 6.1). These results are fundamentally inconsistent with the well-developed historical model of this system and this has motivated a substantial effort to revisit Plaskett's Star in the context of developing a new model for the composition and structure of this enigmatic system.
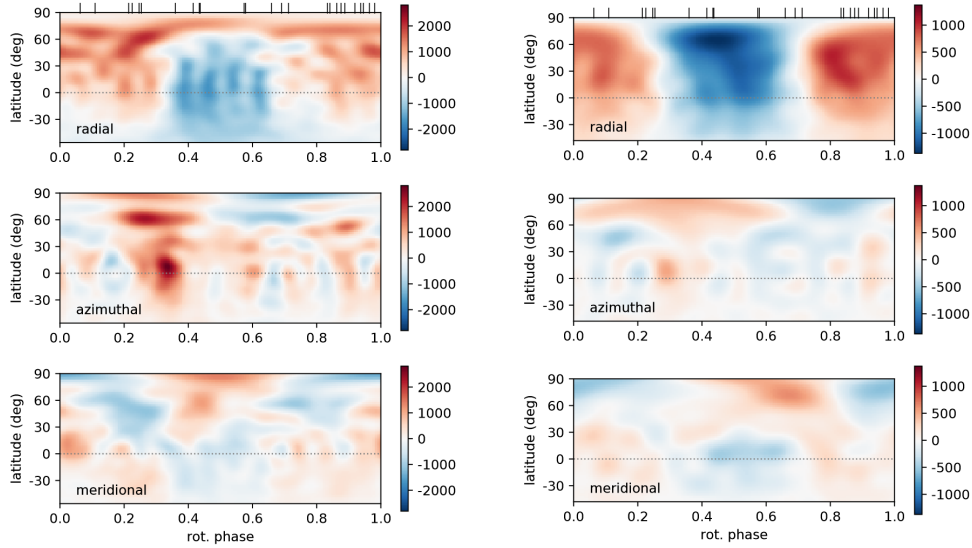


Figure 2.2: The maps of the surface magnetic field geometry reported by Grunhut et al. (2022). These decompose the vector magnetic field into radial (upper frames), azimuthal (center frames), and meridional (lower frames) components. The left three panels are the maps that were determined assuming the Linder et al. (2008) orbital model, whereas the maps in the right three panels were determined assuming a constant radial velocity. This figure was originally published by Grunhut et al. (2022).
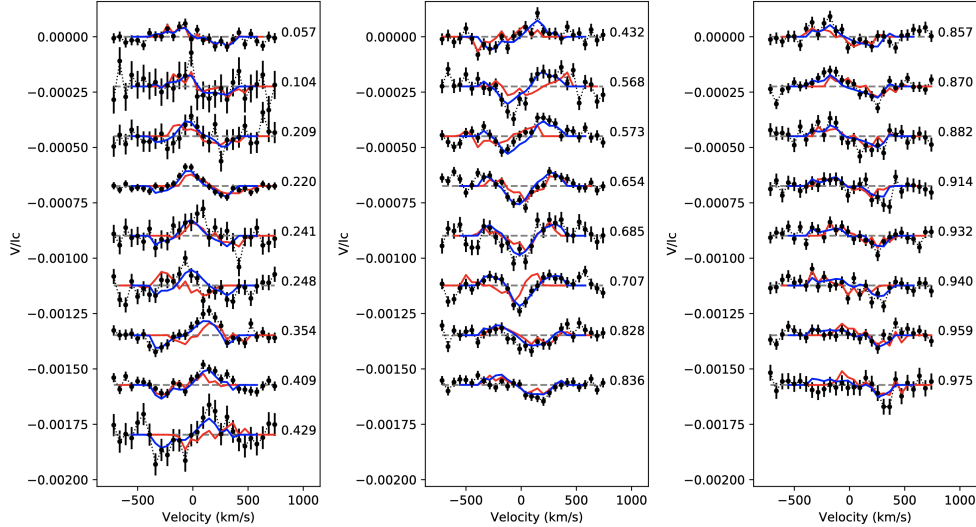
Figure 2.3: Fits to the Stokes V profiles from ESPaDOnS observations of Plaskett's Star from the analysis of Grunhut et al. (2022). The black points indicate the measurements in Stokes V, while the blue line correspond to the fits assuming a constant radial velocity and the red lines correspond to the fits assuming the Linder et al. (2008) orbital model. This figure was originally published by Grunhut et al. (2022).

## 2.3 Revisiting Plaskett's Star from a New Perspective

The results of Grunhut et al. (2022) clearly motivated a revision of the previously well-established structure and composition of this system. This is complicated by the wealth of observational results in literature which were reasonably consistent with the historical model (radial velocity measurements of the BLC notwithstanding). In the case where the results published by Grunhut et al. (2022) are to be believed and the spectral lines of the BLC are taken to be stationary, understanding Plaskett's Star requires three major questions to be addressed:

1. What is responsible for the radial velocity variations of the NLC?
2. Why does the magnetic star demonstrate such rapid rotation?
3. What is responsible for the chemical peculiarity of the system?

The first question implies two scenarios: one where the BLC is responsible for the observed radial velocity variations of the NLC, and one where it

19

is not. In the former case, a large mass ratio between the two components is implied. Based on new radial velocities measured from ESPaDOnS spectra (Kochukhov, private comm.), the implied mass ratio is $M_{\mathrm{BLC}}/M_{\mathrm{NLC}} = 32.3^{+8.3}_{-5.5}$. This is a significant discrepency and is challenged by the similar spectral types and luminosities of the two components. In the latter case, some third object is required that is not apparent in the optical spectra.

The significance of the second question is predicated on the phenomenon of magnetic braking described in Sect. 1.1.3. That is, magnetic O-type stars rotate slowly due to rapid spindown as a consequence of strong coupling between their magnetic fields and outgoing winds. Plaskett's Star is the most rapidly rotating known magnetic O-type star by a significant margin (G. A. Wade, private comm., 2022). Its rapid rotation was previously understood to be a consequence of mass transfer in a RLOF event, however the reason for the rapid rotation is now unclear and a consideration for the structural revision.

The chemical pecularities of this system were also addressed in the historical model by the interpretation of this system as an evolved binary. Particularly, the RLOF event transferred mass from the NLC to the BLC, revealing layers with that had previously undergone chemical processing associated with CNO cycling in the NLC and causing an apparent depletion in N for the BLC. Similar to the rapid rotation of the BLC, models which don't include some sort of binary evolution face challenges with addressing the chemical peculiarities of the two components.

Two hypotheses have emerged to restructure Plaskett's Star in light of the Grunhut et al. (2022) result. These are explored by Stacey et al. (2022, pending publication in Proceedings of the International Astronomical Union Symposium 361) and the relevant discussion has been adapted here to provide context for the work in this thesis.

### 2.3.1 An Unseen Object Companion

The first hypothesis considers the case where the NLC is in a close $P \approx 14.4$ d orbit with a third object, and the BLC is either dynamically unrelated or weakly dynamically bound (e.g. hierarchical trinary). The minimum mass of a companion based on the RV variations of the NLC can be determined through the binary mass function (BMF). For a star with orbital velocity $v_r$ in a single-lined spectroscopic binary system with an inclination of $90°$ and a

period of $P_{orb}$, the BMF is given by

$$\mathrm{BMF}(P_{\mathrm{orb}}, v_r) = \frac{P_{\mathrm{orb}} v_r^3}{2\pi G} \qquad (2.1)$$

where $G$ is the gravitational constant. Assuming $v_r = 210 \pm 13$ km/s (Wade, private comm.) and the Linder et al. (2008) orbital period, the minimum mass of an unseen binary companion to the NLC is $13.8 \pm 2.6$ M$_\odot$ according to Eq. 2.1. This is consistent with a potential BH companion and a star or stellar remnant should be visible in the optical spectrum. Cyg X-1 is a O/BH binary system with an orbital period of approximately 6 days (Brocksopp et al., 1999) and an estimated BH mass of 10 to 23 M$_\odot$ (Ziolkowski, 2014), which is nominally similar to what is expected of an O/BH binary model for Plaskett's Star. However, this system exceeds the X-ray luminosity of Plaskett's Star by approximately 5 orders of magnitude (Orosz et al., 2011). Casares et al. (2014) described a Be/BH binary with relatively low X-ray luminosity ($L_X < 1 \times 10^{32}$ erg/s) owing to inefficient accretion. Therefore, it does appear that examples in literature could support a potential O/BH binary model to explain the RV variability of HD 47129, but nevertheless it may be challenging to reconcile the strong winds expected from the O star with the low X-ray luminosity of the system.

Turner et al. (2008) and Sana et al. (2014) reported a total of three targets detected with infrared interferometry within 1 to 8000 milli-arcseconds of Plaskett's Star (subtending $\approx 1 - 8000$ AU), none of which are consistent in luminosity with the broad-line component. Therefore, this hypothesis restricts the broad-lined component to narrow ranges of orbital phase in a hierarchical configuration. Additionally, this solution does not provide a natural explanation for the high rotation rate of the magnetic star nor the chemical peculiarity of either component.

### 2.3.2   A Stripped Star Companion

A second revised model under consideration for HD 47129 instead enforces the mass ratio as implied by the radial velocities measured from disentangled spectra (O. Kochukhov, private comm.). Assuming the BLC is a "normal" magnetic O star with the Linder et al. (2008) minimum mass of $47 \pm 0.3$ M$_\odot$, a mass of the order of a single solar mass is implied for the NLC. This component still demonstrates an O spectral type in the spectroscopic observations and comparable luminosity to the BLC. A stripped sdO star is a potential

candidate for the NLC in this case, which is a star that has lost its envelope through binary interaction leaving a hot, compact object (Götberg et al., 2018).

This prescription addresses the radial velocity measurements of both components simultaneously and accounts for the rapid rotation of the BLC through angular momentum transfer by the stripped material. Götberg et al. (2018) remarked that the layers exposed at the surface of stripped stars are regions where CN and CNO hydrogen burning have occurred, yielding enhancements in He and N and depletions in H, C, and O. This is particularly consistent with the strong N enhancement and C depletion measured by Linder et al. (2008) and the (qualitative) absence of oxygen lines in the spectra (G. A. Wade, private comm.). Unintuitively, given the low radius of such a stripped star, this solution is also qualitatively consistent with the permissible luminosities of the two components inferred from their spectral line profiles (S. E. de Mink, private comm.). However, this model is inconsistent with the $\log g$ of 3.5 (cgs) reported by Linder et al. (2008), as candidates for the NLC according to the Götberg et al. (2018) would demonstrate $\log g > 4.5$.

A modification of the sdO+O hypothesis has also emerged which addresses the inconsistency with the observed $\log g$, which is based on a system demonstrating some analogous spectroscopic properties. This system is HR 6819, which is a spectroscopic binary containing a Be component, observed to exhibit minimal variability in radial velocity, and a B component, observed to exhibit radial velocity variability consistent with membership in a binary system (Rivinius et al., 2020). This system was proposed to be a heirarchical triple with an inner BH+B binary, however this was refuted by interferometric observations (Frost et al., 2022). Alternatively, this system has been interpreted as a Be+B binary where the B star is a "bloated" stripped star: a star that has transferred most of its envelope to its companion however is still coalescing into a compact subdwarf star (Bodensteiner et al., 2020; El-Badry and Quataert, 2021). In this case the stripped star has lost most of its mass however remains approximately the same size as a main-sequence star of comparable spectral type, and proceeds to collapse to a compact subdwarf star on a timescale of the order $10^5$ years.

## 2.4 Photometric Variability of Plaskett's Star

Plaskett's Star demonstrates significant ($\approx$ 50 mmag), multi-periodic photometric variability (Mahy et al., 2011; Burssens et al., 2020). Mahy et al. (2011) identified variability at 150 frequencies in the CoRoT photometry for HD 47129 (see Sect. 3.4), 43 of which were determined to be statistically significant. The principal photometric variability observed by Mahy et al. (2011) was at a period of 1.215 d and associated harmonics, with the first harmonic of this period demonstrating the highest amplitude in the power spectrum. This is now known to arise due to rotational modulation of the BLC (Grunhut et al., 2022). Particularly, the centrifugal magnetosphere of the BLC hosts two dense regions of corotating, hot plasma which are each seen once per rotation, leading to strong variability at the first harmonic of the rotational period. Mahy et al. (2011) also observed photometric variability at the Linder et al. (2008) orbital period and speculated this to be caused by a hot spot on the surface of one of the stars. A limited frequency analysis of the TESS photometry of Plaskett's Star was also performed by Burssens et al. (2020), revealing 9 frequencies consistent with the results of Mahy et al. (2011).

Mahy et al. (2011) also performed binary modelling of this system using the *Nightfall* program (Wichmann, 1998)[2], under the assumption of the historical model. They found the orbital modulation in the CoRoT photometry was consistent with a combination of ellipsoidal variability and a hot spot on the NLC facing the BLC. They hypothesized the hot spot was related to wind interaction between the two stars.

The frequency analysis of Burssens et al. (2020) imposed a more conservative criterion for statistical significance of extracted frequencies and also used only a highest-amplitude criterion for peak selection, and as a consequence their analysis only identifies nine significant frequencies. Additionally, Burssens et al. (2020) analyzed a large sample of targets and therefore the interpretation and discussion of the frequency spectrum for any given star, Plaskett's Star included, was brief. On the contrary, Mahy et al. (2011) provided a sophisticated analysis and discussion of the frequency spectrum as measured from the CoRoT photometry. However, this work was conducted under the assumption of the historical model for Plaskett's Star and this is reflected in the interpretation of the measured frequencies. Furthermore, while they correctly hypothesized the presence of stochastic variability in the light

---

[2]Also see: `http://www.lsw.uni-heidelberg.de/users/rwichman/Nightfall.html`.

curve, the asteroseismological theory of stochastic low-frequency (SLF) variability was only beginning to develop at the time of publication. In fact, the observation of red noise in CoRoT photometric light curves around this time by Blomme et al. (2011) is often regarded as the first entry of the many papers addressing SLF variability over the past decade. Therefore, while both the TESS and CoRoT photometry analyzed in this work have been previously analyzed, this work expands on the previously-published results by (1) interpreting the frequency spectra in the context of the results published by Grunhut et al. (2022), (2) providing self-consistent analyses of both the CoRoT and TESS photometry, which is particularly useful given the time between the collection of each dataset, and (3) providing an asteroseismological perspective on Plaskett's Star in the context of SLF variability.

# 3  Photometry

## 3.1  A Primer on Photometric Observations

Modern photometric data in spectral regions around the optical band is typically collected by a telescope with a mounted charge-coupled device (CCD) imager. A CCD imager is a high-efficiency solid-state detector consisting of a 2-D array of metal-oxide semiconductor (MOS) capacitor "pixels" which rely on liberation of charge carriers by incident photons to produce detections. While the shutter on the imager is open, incident photons scatter electrons from their bound states and charge is accumulated in the respective pixel. The charge on each pixel is then read to produce an image, which can be normalized to a flux by dividing by the gain and exposure time. Therefore, the raw data read from a CCD is in either integrated electrons or electrons per second. Depending on the scientific objectives, particularly when relative or differential measurements are the principal interest, units of electrons/s are perfectly acceptable.

The apparant brightness of an astronomical object can be determined from a CCD image by summing the flux across all pixels it illuminates. This process can be performed on a series of images (indexed in time) to construct a time series of brightness measurements, commonly referred to as a *light curve*. A common means of converting a large sample of raw images into a light curve is a method called simple aperture photometry (SAP), where a pre-defined pixel selection (called an aperture mask) is applied across all images to make brightness measurements. This greatly reduces the effort required to extract a light curve from a large number of observations, however also requires a stable imaging platform such that the object's translation is minimal compared to the span of the pixels it illuminates. This is particularly useful for high-cadence monitoring campaigns, where the number of CCD images can easily exceed $10^4$.

The brightness variability of astrophysical objects can take various forms and yield insight into a plethora of physical processes. A particularly powerful probe into physical behaviour in stellar systems is through analysis of periodic signals in their light curves. Signals at binary orbital periods can give insight into the structure of binary systems, variability at stellar rotational periods can reveal the structure of stellar atmospheres, and asteroseismological signals can probe the internal configuration of stars. This work principally focuses in the frequency analysis of stellar light curves pertaining to Plaskett's Star, and the analysis methodology is discussed in Chapter 4.

### 3.1.1 Standard Photometric Systems and Magnitude

The field of astronomy is well known in the broader physics community to have some unusual systems of measurement, often rooted in some form of historical utility. A prolific example of this is the tendency to express the brightness of astrophysical objects in terms of *magnitude*. Magnitude is a unitless quantity that describes the brightness of an object on a logarithmic scale with respect to some reference object (assigned a magnitude 0), which has historically been the star Vega. Emission mechanisms are generally variable with wavelength and therefore a meaningful magnitude measurement requires a spectral passband to be specified as well as a reference magnitude and brightness. This has led to the establishment of several standard photometric systems with different treatments of passbands and reference values. All modern formulations of the magnitude scale agree that a unit increase in magnitude corresponds to a decrease in brightness by a factor of the fifth root of 100 ($\approx 2.5$). Therefore the apparent magnitude[1] $m$ of an object with flux $I$ with respect to a reference object denoted by a subscript $r$ is

$$m = -2.5 \log(I/I_r) + m_r. \tag{3.1}$$

The *Johnson* or *Johnson-Morgan* system is an example of a magnitude system which sees widespread use today (Johnson and Morgan, 1953). It defines three common[2] passbands: Ultraviolet, Blue, Yellow (UBV originally in Johnson and Morgan, 1953), which was later expanded in various ways by a variety of authors to access the infrared regime (e.g. the Johnson-Cousins UBVRI system; see Bessell (1990)). A comprehensive review of the challenges and development of standard photometric systems through the latter half of the 20th

---

[1]As opposed to absolute magnitude, which is the apparent magnitude of the object at a standard distance of 10 pc.

[2]The actual boundaries of these passbands have varied between authors and instruments.

century is presented by Bessell (2005). The nuances of standard photometric systems are not entirely relevant to this work, however the critically relevant points from this discussion are:

1. A brightness measurement must be accompanied by a description of the passband treatment and, in the case of magnitude, the reference value,
2. Measurements obtained in different passbands are, in general, non-trivial to reconcile for direct comparison,
3. Photometric instruments will generally have different passbands according to their scientific objectives.

While the passband is important to the shape and amplitude of the light curve, the reference point is not. Therefore, a light curve in any linear, positive, unit $I$ can be converted to magnitude with an arbitrary zero point using

$$m = -2.5 \log(I). \tag{3.2}$$

Subtracting the average value of the light curve in magnitude will yield a light curve in *differential* magnitude, which is identical no matter the reference object chosen (for a given passband). It's important to note, however, that the conversion to magnitude *will* affect the shape of the light curve due to the logarithmic nature of magnitude scales. For the convenience of the reader, flux measurements in this work are expressed in differential millimagnitude (mmag), however all analyses were conducted in linear units. The passbands are those of the instrument which collected the data, unless otherwise specified.

## 3.2   Physics of Modulation at Orbital Periods

Two objects in a mutual orbit follow closed, smooth paths around their combined center of mass. To an external observer, the relative velocity of the objects along the observer's line of sight (the radial velocity) varies quasi-sinusoidally as the objects move around the center of mass of the system. In binary systems, a Doppler shift is independently introduced to the light emitted by each object according to their apparent radial velocities as observed by a distant observer. This is readily apparant in spectroscopic observations, where the absorption line contributions from each component will vary according to orbital phase and cause either variability in the blended line profile, or complete separation of the absorption lines for each star. The instantaneous radial velocity of each component can be measured by separating their contributions to an absorption or emission feature associated with a spectral line with a known rest wavelength (spectral disentangling) and determining the

velocities which would produce the observed Doppler shifts. With several spectroscopic observations at different orbital phases, several properties including the orbital period, mass ratio, and orbital eccentricity can be inferred from direct measurements of radial velocity.

While spectroscopic variability in stellar binary systems is relatively easily understood as the consequence of variable radial velocities in each component, the physics of photometric variability introduced by binary orbits is more complex. Variability in brightness at a period equal to the orbital period for a non-eclipsing stellar system can be attributed to three potential physical sources: Doppler boosting, ellipsoidal variability, and reflection (Faigler and Mazeh, 2011). For Doppler boosting (also referred to as the beaming effect), the Doppler shift of a target enhances or diminishes its brightness based on its motion towards or away from the observer, respectively. This has historically been of little relevance as the effect is only significant in very short period systems and very high precision photometry is required to observe it. The paradigm of high-precision space photometry missions has, however, produced regular detections of this phenomenon (e.g. van Kerkwijk et al., 2010; Carter et al., 2011). Doppler boosting will be maximized at maximum velocity towards the observer and minimized at maximum velocity away from the observer, therefore the brightness variations will be in phase with the orbital velocity variations (see Figs. 3.1 and 3.4). The radial velocities of the two components of a stellar binary will always be of opposite sign, therefore the diminished brightness of one component will act against the enhanced brightness of the other. Consequently, Doppler boosting is most easily observed in binaries where the constituents demonstrate significantly different luminosities.

Ellipsoidal variability arises due to tidal distortion of a star by a companion. As the star orbits its companion, the visible cross section will be variable and therefore the brightness of the star will also modulate (Morris, 1985). This is illustrated in Fig. 3.2. The ellipsoidal distortion is maximized when the objects are at their maximum apparant separation, which corresponds to a maximum *absolute* radial velocity. The brightness maxima therefore occur twice per orbit (the first harmonic frequency) and are out of phase by a quarter wave with respect to the radial velocity variations (see Fig. 3.4).

The final source of orbital photometric variability is called reflection, however it is not truly a reflective effect. This arises when a bright object radiatively heats the facing side of a relatively-cooler companion object, creating a
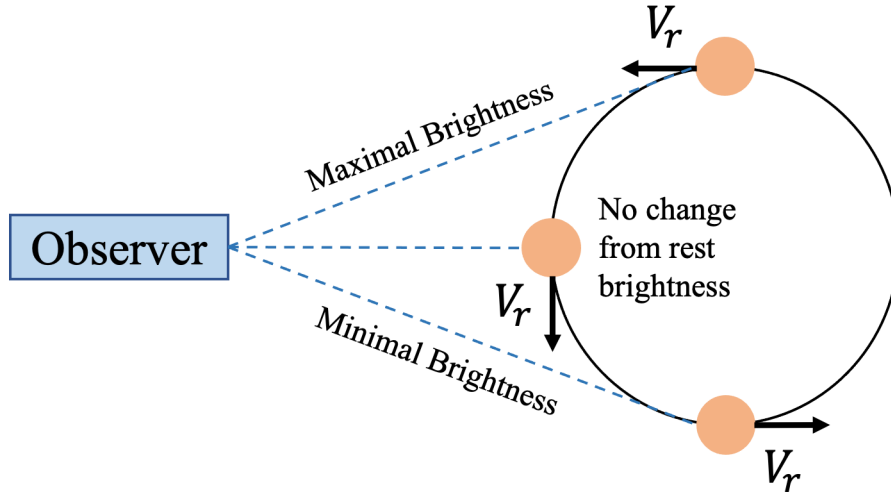
Figure 3.1: An illustration of the expected brightness variations due to Doppler boosting of a star as it proceeds around a circular orbital path. The companion star, which the pictured star is in a mutual orbit with, is omitted for clarity.

difference in temperature between the side facing the brighter object and the side facing away. As the hotter side comes in and out of view once per orbit, the observed brightness varies with the same period as the orbital period (see Fig. 3.3). The brightness enhancements are maximized when the hot side is maximally visible to the observer, which occurs when the two objects are at their minimum apparent separation. Therefore, brightness variability due to reflection will be out of phase with the radial velocity variability by a quarter wave (see Fig. 3.4). More specifically, it will be advanced and retarded by a quarter wave relative to the radial velocity curve of the cooler and hotter star respectively.
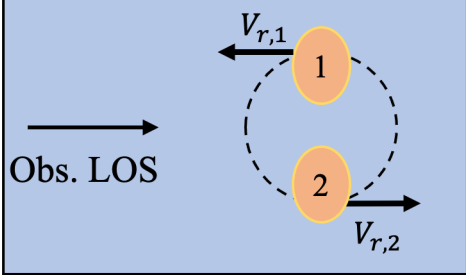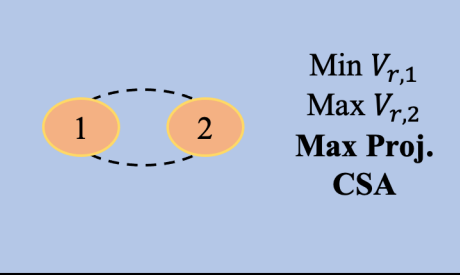
Figure 3.2: An illustration of ellipsoidal distortion leading to ellipsoidal brightness variability in a non-eclipsing binary. The cross-sectional area (CSA), and therefore the apparant brightness, is maximized when the stars are observed to be at their maximum separation. This occurs twice per orbit.
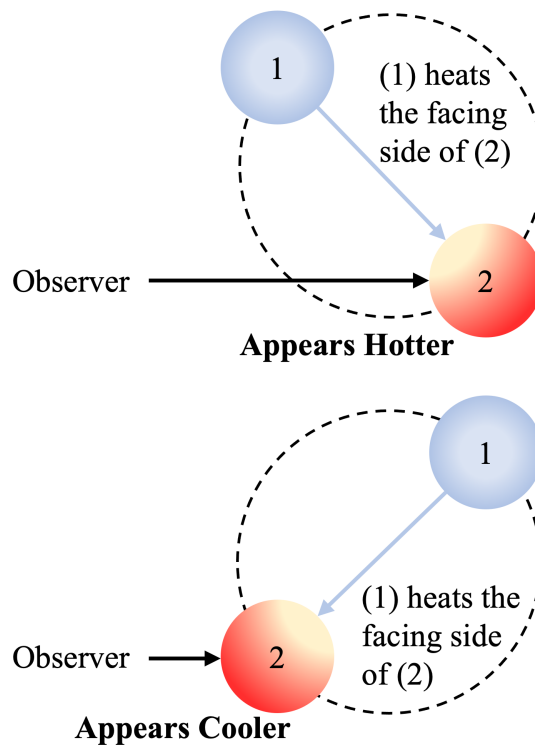
Figure 3.3: An illustration of reflective effects in a binary with a significant luminosity difference between its constituents. Star 1 is considerably hotter and more luminous than its companion star 2, therefore the facing side of star 2 will be heated by radiation from star 1.
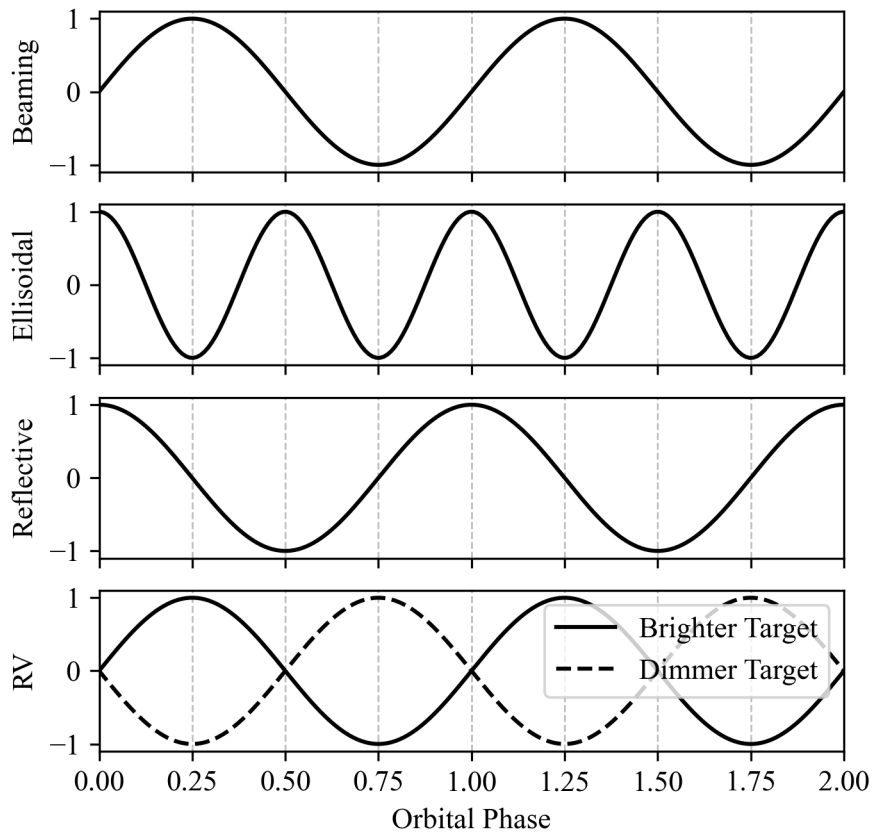
Figure 3.4: The normalized amplitude as a function of phase that is expected for variability arising from Doppler boosting, ellipsoidal variability, or reflection in an ideal system with zero eccentricity and a sufficient temperature differential to cause reflection. The normalized radial velocity curves are given in the bottom panel and the cooler star is indicated by a dashed line.

## 3.3 TESS

The Transiting Exoplanet Survey Satellite (TESS) is a survey satellite launched by NASA in 2018 with the primary objective of detecting transiting exoplanets around bright, nearby stars (Ricker et al., 2015). The primary mission was to perform a two-year, near-all-sky survey and collect photometric light curves at a cadence of two minutes for over 200 000 stars brighter than 13th magnitude. The satellite occupies an inclined elliptical 13.7 d orbit in 2:1 resonance with the lunar orbit and its apogee and perigee are at approximately 59 and 17 Earth radii respectively. The instrumentation consists of four 4096pixel $\times$ 4096pixel CCD cameras with fields of view of $24° \times 24°$ and a (non-linear) spectral response function spanning approximately 600 to 1000 nm. The cameras were arranged in a $1 \times 4$ configuration for a combined field of view of $24° \times 96°$ (see Fig. 3.5a). The observing strategy divided the celestial sphere into 26 partially-overlapping $24° \times 96°$ sectors, 13 per hemisphere (see Fig. 3.5b/c), which were each observed for two spacecraft orbits (up to 27.4 d). TESS completed its primary mission on July 4, 2020 and is now well into its extended mission (Weinberg et al., 2019; Hertz, 2019). Plaskett's Star was observed by TESS as a part of sector 6 from Dec 15, 2018 to Jan 6, 2019 and has not been observed in any additional sectors.
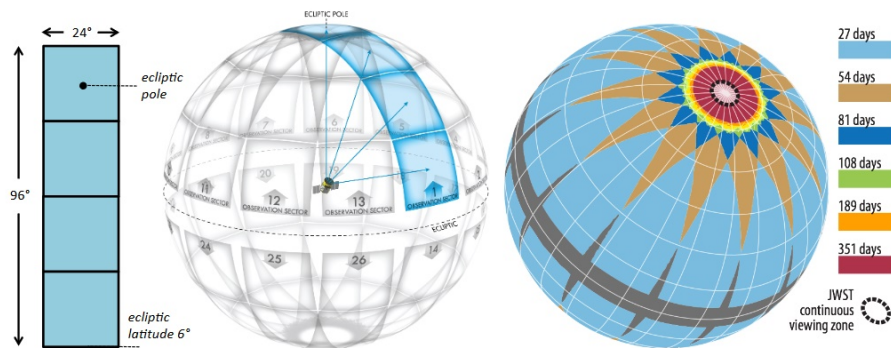


Figure 3.5: Left: A schematic of the arrangement of the four CCD cameras. Center: The celestial sphere divided into TESS observing sectors. Right: Total monitoring durations across the celestial sphere. This figure was originally published by Ricker et al. (2015).

TESS provides several data products to the public through regular data

releases with no proprietary periods. The primary data products are available as full-frame images (FFIs), target pixel files (TPFs) and light curves. A FFI is a stack of images at the full resolution of a single camera and a cadence of 30 minutes. TPFs are extracted from the FFIs aboard the satellite before downlink and are stacks of small images (typically 11pixels × 11pixels) around pre-determined targets at a cadence of 2 minutes. The FFIs and TPFs are calibrated according to instrument calibration models prior to dissemination. Finally, an automated data reduction pipeline extracts light curves from the calibrated TPFs according to an automatically-determined aperture mask to create a SAP light curve and then performs a detrending to create a pre-search data conditioning (PDC)[3] SAP light curve (Twicken et al., 2020).

TESS is principally an exoplanet detection mission, as clearly outlined by Ricker et al. (2015). Nevertheless, the high-precision high-cadence photometry collected by the satellite is also suitable for the study of stellar physics and has been used extensively to study stellar binarity (Kołaczek-Szymański et al., 2021; Prša et al., 2022), rotation (Cunha et al., 2019), pulsation (Antoci et al., 2019; Bowman et al., 2019b, 2020; Burssens et al., 2020; Cunha et al., 2019), and magnetism (David-Uraz et al., 2019). That being said, it is important to emphasize the fundamental differences in the character of the variability associated with exoplanetary transits and most stellar phenomena. The automated data reduction pipeline can diminish or even extinguish longer-period signals that are recovered when a manual detrending is conducted (e.g. O star rotational modulation, $P \approx 7$ d, see Barron and Wade, 2021). The relatively large pixels of the CCD cameras and the automated aperture mask selection procedures employed for light curves extracted by the automated pipeline can also lead to contamination in stars with bright neighbours (Barron et al., 2021). That is, pixels in the aperture mask for a target of interest can be partially illuminated by light from a nearby bright star and introduce spurious signals in the extracted light curve. For these reasons, it's preferable to perform manual extraction and detrending procedures instead of using PDCSAP light curves when focusing on stellar variability.

### 3.3.1 Extracting TESS Light Curves

To extract a light curve for HD 47129, the TPF and co-trending basis vectors (CBVs) were retrieved from the public archive using the Python *Lightkurve* package (Lightkurve Collaboration et al., 2018)[4]. TPF images were omitted

---

[3]The "pre-search" terminology refers to the search for transiting exoplanets.

[4]*Lightkurve* documentation is available at `https://docs.lightkurve.org/index.html`.
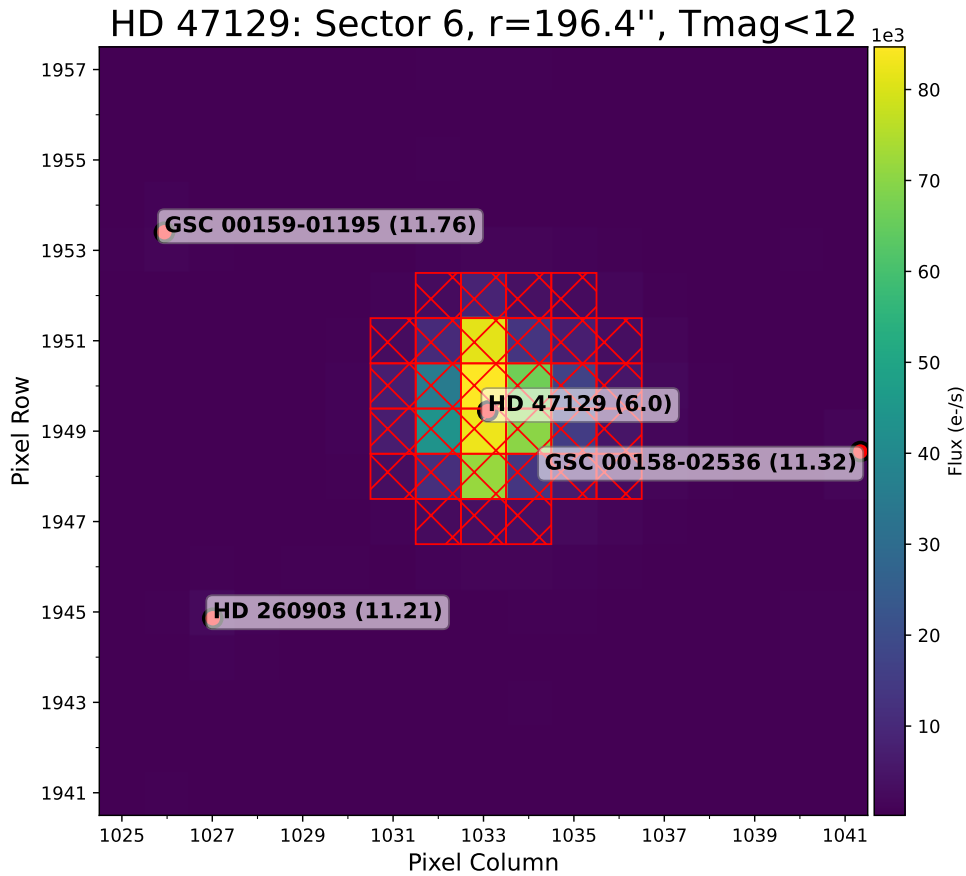
Figure 3.6: An $18 \times 18$ pixel region around Plaskett's Star. Plaskett's Star and its nearby neighbours with TESS magnitudes brighter than 12 are annotated, with their respective TESS magnitudes in brackets following their identifier. The automatically-generated pipeline mask is indicated by the red cross-hatched pixels. The only stars nearby to HD 47129 are several orders of magnitude fainter, therefore significant contamination is not expected in the TESS data for HD 47129. Figure provided courtesy of J. A. Barron.

wherever data quality flags indicated attitude tweak events, satellite "safe mode" events, coarse pointing, earth pointing, reaction wheel desaturation events, manual exclusion, cosmic rays, and earth/moon straylight. An aperture mask, illustrated in Fig. 3.7, was defined as all pixels with integrated fluxes that exceeded the average integrated flux of the TPF by a factor of 9.

A SAP light curve was extracted using this aperture mask. The SAP data was then detrended to produce a manually extracted equivalent to a PDCSAP light curve, which is referred to as "detrended" in this work. Both these data were analyzed in this work to understand how the detrending affected the results of the frequency analysis. This work did not make use of the FFI data, which could be used to extract a 30-minute cadence light curve for Plaskett's Star.

The detrending process for TESS data is highly similar to that of the mission's predecessor, the Kepler space telescope (Smith et al., 2020). CBVs are sets of quasi-light curves which represent trends observed across all targets in the respective TESS sector observed by the same detector and are provided as auxiliary data products for each FFI/TPF/light curve (Smith et al., 2020; Twicken et al., 2020). Three sets of CBVs are available for TESS data and the choice of which to employ is dependent on individual use cases. Single-scale and multi-scale CBVs are typically used with mutual exclusivity and differ in treatment of the systematic signals by apparent frequency. The single-scale CBVs are provided as a single set which represent all apparent systematic trends present and are recommended for preserving long-period signals. Multi-scale CBVs are provided in multiple sets (typically three - low, medium, and high frequency) which each independently treat address systematic trends within a specific region of frequency space and are recommended when searching for exoplanetary transits. Spike CBVs are used in tandem with either the single-scale or multi-scale CBVs and contain short, impulsive event corrections. For an extended discussion on detrending with CBV focusing particularly on asteroseismology, see Lund et al. (2021).

For HD 47129, eight single-scale CBVs were used in the detrending. Spike CBVs were not included, as they only served to introduce additional noise. The detrending was performed by linear regression of the light curve against the CBVs, which yielded a trend model underlying the light curve. This model was almost certainly overfit, however the primary consequence of this was the introduction of some degree of noise in a high-frequency band outside the region of scientific interest. The detrending of TESS light curves is a complex and relatively technical subject and an extended discussion pertaining to detrending for this work can be found in App. A. The final analysis-ready SAP and detrended light curves contained 14491 data points and spanned approximately 21.63 days.

Several aperture masks were tested to explore the influence of mask choice

on the light curve and frequency analysis results. For each test aperture, a light curve was extracted and detrended with 0, 4, 8, 12, and 16 single-scale CBVs. A simple 20-frequency pre-whitening was performed for each mask. The results varied negligibly and therefore details of the mask choice within the TPF was concluded to have minimal effect on the results. The masks considered for this testing are provided in App. C. The final aperture was selected such that the included pixels exceeded the average flux level of all pixels by a factor of 9 (see Fig. 3.7).
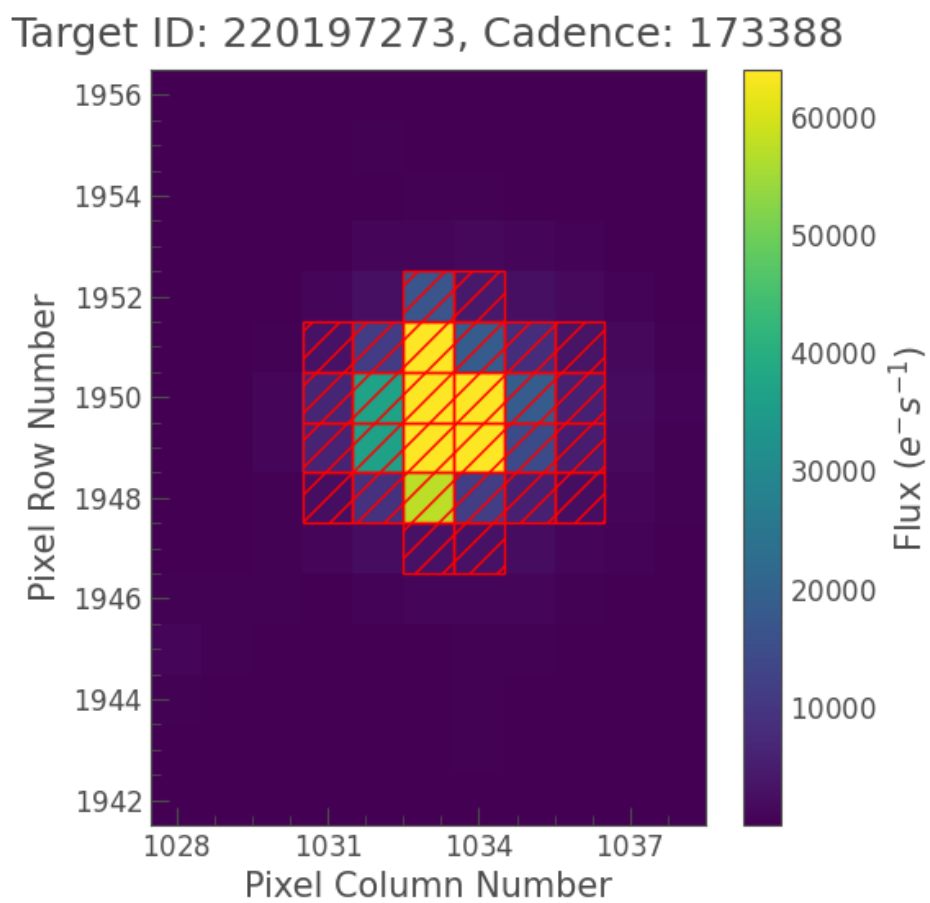
Figure 3.7: One aperture used to extract a light curve from the TESS TPFs of HD 47129, indicated by the red hatched pixels. This aperture was used to extract the canonical light curve analyzed in this work.
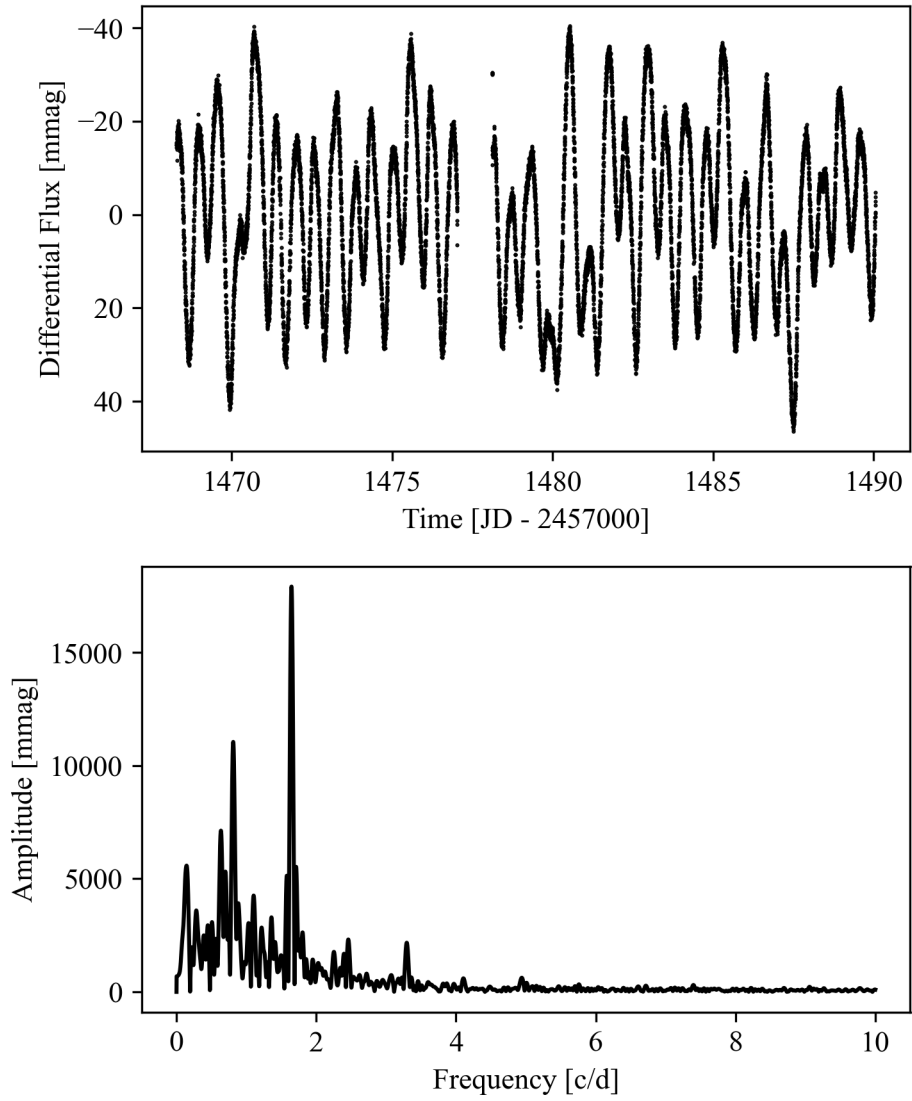
Figure 3.8: The TESS light curve (top) and associated periodogram (bottom) for HD 47129.

## 3.4 CoRoT

The Convection, Rotation, and Planetary Transits (CoRoT) satellite was an optical space telescope developed and operated by the French space agency Centre National D'études Spatiales (CNES) with contributions from the ESA, Austria, Belgium, Germany, Spain, and Brazil (Auvergne et al., 2009). It was launched on Dec 27, 2006 and was intended to collect data to conduct astero-seismological studies of pulsating stars as well as to detect exoplanetary transits. The satellite operated for approximately 7.5 years and was decommissioned on June 17, 2014[5]. CoRoT's observing strategy involved both long runs, lasting 150 days, and short runs, lasting only 20-30 days. The satellite occupied a polar orbit with the ecliptic pole oriented towards the galactic center. Observations toward and away from the galactic center were collected from April to October and November to March respectively, which ensured the sun remained beside or behind the satellite relative to its observing direction at all times (Baglin et al., 2016). Each seasonal cycle contained one long and one short run. The long runs conducted asteroseismological observations and exoplanetary transit observations simultaneously while the short runs were dedicated to exploratory asteroseismological programs (Boisnard and Auvergne, 2006). The instrumentation consisted of an afocal refractor telescope with a field of view of $2.7° \times 3.05°$ mated to four 2048pixel $\times$ 2048pixel CCDs. The satellite hosted an asteroseismology channel and an exoplanet channel, each allocated two of the four CCDs, enabling simultaneous observations for both scientific objectives. The full optical system demonstrated a bandpass of approximately 300 nm to 1100 nm with a nonlinear response function demonstrating peak efficiency at approximately 600 nm (Auvergne et al., 2009).

HD 47129 was observed as a part of the second CoRoT short run SRa02 from Oct 8, 2008 to Nov 12, 2008, collecting a total of 92696 photometric data points at a cadence of 30 seconds. These data were first analyzed by Mahy et al. (2011), who reduced/detrended the data and performed a Fourier-based pre-whitening analysis to find a total of 43 significant periodic components. They reported the strong variability at 0.82 c/d and harmonics, which is now known to be associated with the rotation of the BLC. Variability at 0.07 c/d and its harmonics was also detected, which is associated with the historically established orbital period. The purpose of including this data in the work presented in this thesis was twofold: (1) it provided a literature benchmark to compare the analysis methodology against, and (2) it allows a self-consistent

---

[5]See `https://presse.cnes.fr/en/cp-8761`.

comparison between the TESS data and the CoRoT data with a 10-year baseline.

The CoRoT data are principally provided in the form of light curves which, within the relevant catalogues, are suitable for use in asteroseismology (e.g. a manual extraction is not required, unlike the TESS data). A light curve was retrieved from the public archive[6] which was corrected for aliasing, offsets, backgrounds, CCD temperature jumps, and long-term CCD degredation prior to dissemination. Points were removed according to data quality flags indicating outliers (e.g. cosmic rays), invalid, South-Atlantic Anomaly crossings, mask-change discontinuities, or spacecraft motion. Ultimately, 9416 points were removed and the final data contained 83052 points spanning 34.41 days (see Fig. 3.9).

---

[6]http://idoc-corot.ias.u-psud.fr/sitools/client-user/COROT_N2_PUBLIC_DATA/project-index.html
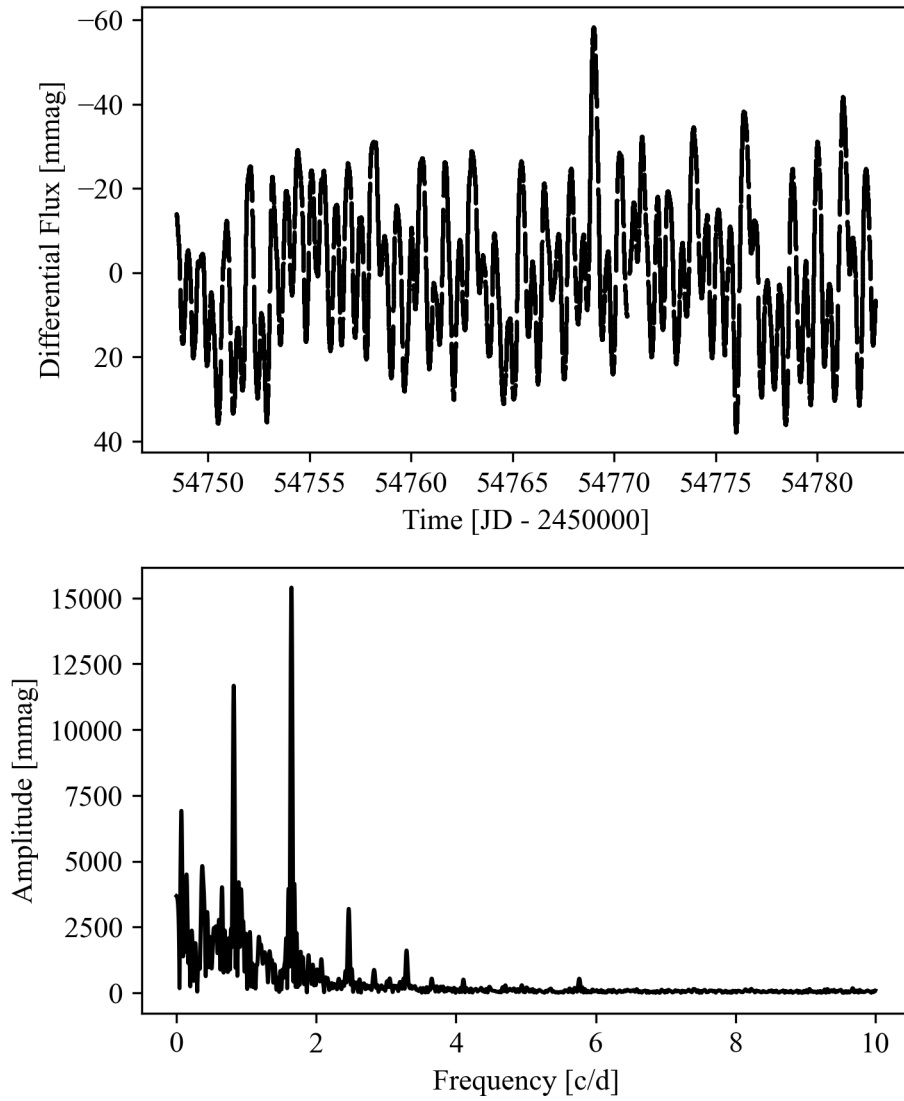
Figure 3.9: The CoRoT light curve (top) and associated periodogram (bottom) for HD 47129.

## 3.5 Hipparcos

High Precision PARallax COllecting Satellite (Hipparcos) was an astrometry satellite launched by the European Space Agency on Aug 8, 1989 (ESA, 1997a). The primary objective of this mission was to measure precise astrometric measurements (positions, proper motions, and parallaxes) for approximately 120 000 stars brighter than magnitude 12.4. It also included an auxiliary instrument which observed approximately 1.06 million stars, constituting the Tycho catalogue, with lower precision (ESA, 1997b, also see `https://www.cosmos.esa.int/web/hipparcos`). The satellite was intended to occupy a geostationary orbit however a booster failure stranded the satellite in a geostationary transfer orbit. A revised mission was developed and Hipparcos was able to collect observations for approximately 3.5 years before it was decomissioned in August of 1993.

Plaskett's Star was observed by Hipparcos over 1096 days from March 11, 1990 until March 11, 1993, during which time 72 data points were collected (Turon et al., 1993). These data are illustrated in Fig. 3.10 and demonstrate relatively large uncertainties in comparison to the expected semi-amplitudes of individual frequencies, ranging from 4 to 8 millimag. The low total number of data points, high uncertainties on each point, and numerous large gaps in the time series render these data unusable for a frequency analysis of Plaskett's Star with a reasonable degree of confidence and scientific value. Therefore it was omitted from further examination.
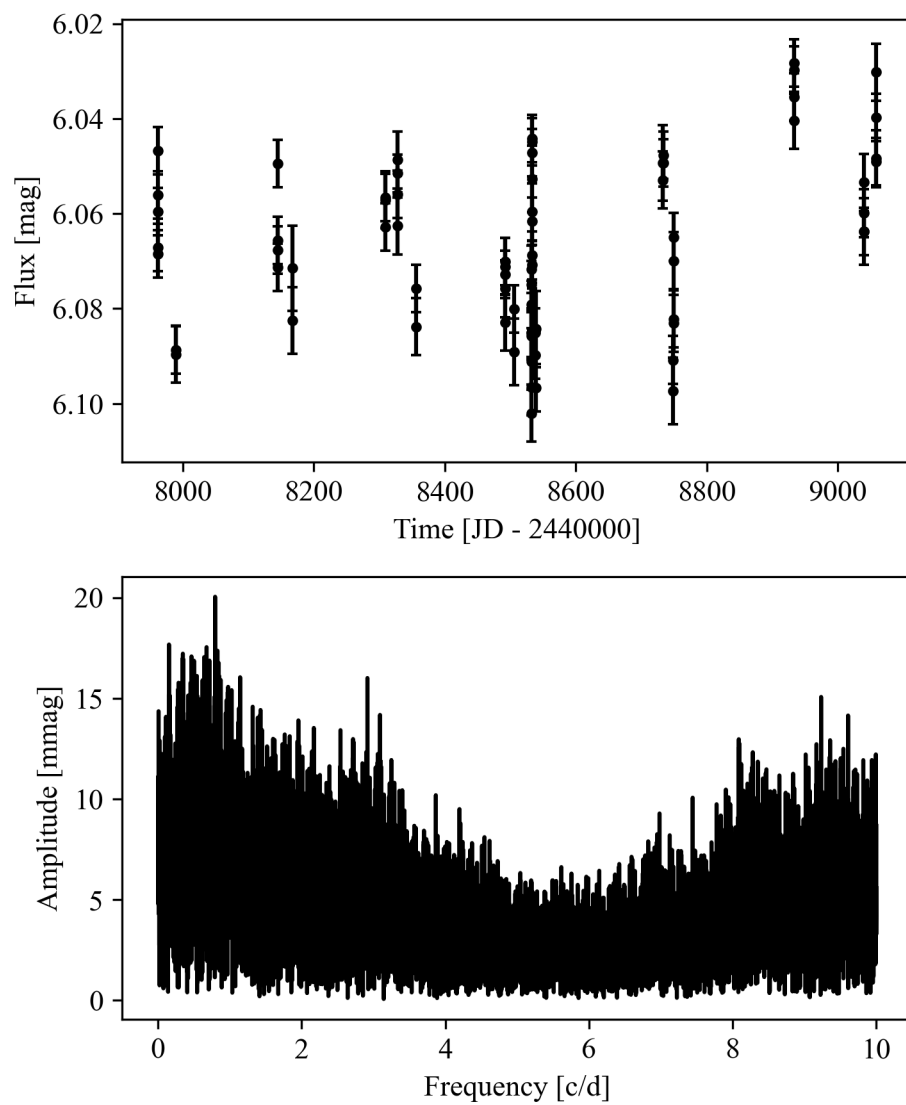
Figure 3.10: The Hipparcos light curve (top) and associated periodogram (bottom) for HD 47129.

## 3.6 ASAS

The All-Sky Automated Survey (ASAS) is a ground-based multi-site photo-metric observation project which has operated since 1997 (Pojmanski, 1997, also see `http://www.astrouw.edu.pl/asas/`). The project has evolved in scope and capability over its lifetime, and presently the stated mission objective is to conduct photometric monitoring in V and I bands for 10 million stars brighter than 14th magnitude distributed across the entire celestial sphere. The ASAS observed HD 47129 from Aug 15, 2002 to Nov 30, 2009 and collected 503 observations spanning 2664.8 days (Pojmanski (1997)). The ASAS light curve is shown in Fig. 3.11 and is clearly contaminated by strong systematics arising due to the collection of observations nightly, as required by a ground-based observing campaign. Furthermore, the uncertainties in this dataset are of the order 10 millimag. The former issue may be alleviated by a careful data reduction, however the latter issue restricts the observable signals in these data to those of significant amplitude. For this reason, these data were omitted from this analysis. Nevertheless, there may be scientific value to a future frequency analysis of these data, particularly focusing on the orbital frequency of the system.
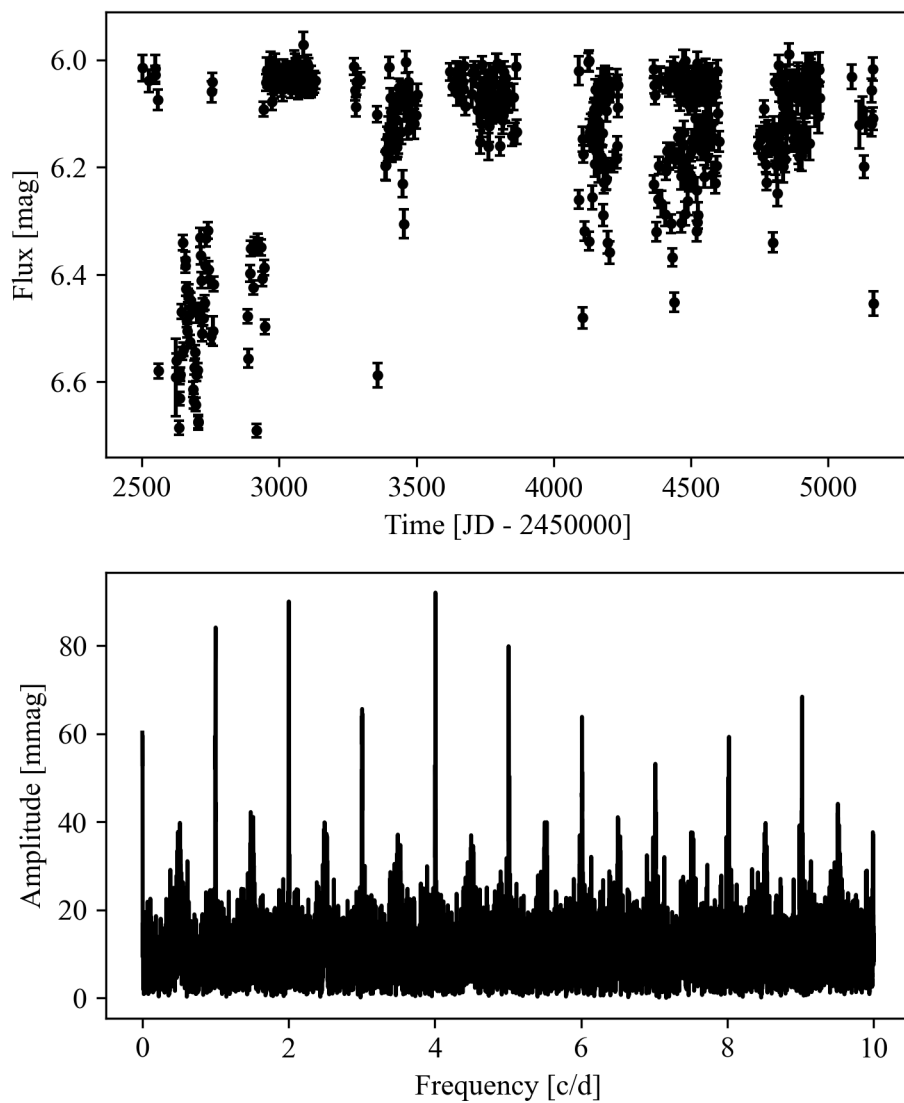
Figure 3.11: The ASAS light curve (top) and associated periodogram (bottom) for HD 47129.

# 4 Methods of Analysis

## 4.1 Time Series Analysis of Stellar Light Curves

Astronomical time series data present unique analytical challenges seldom addressed outside the field of astronomy (Aerts et al., 2010, chapter 5). Ground-based observers have to contend with variable weather, target visibility, the rotation of the earth, and the position of the sun and moon. Consequently, ground-based astronomical time series observations are often discontinuous with uneven sampling and large gaps, even for multi-site campaigns designed specifically to mitigate these challenges. The difficulty in analyzing these data is often further exacerbated by the quasi-peridicity of these interruptions in data collection. For example, it is common for observations to be collected nightly ($f = 1$ c/d) or scheduled according to favourable lunar phases ($P \approx 28$ d).

Space-based observations are inarguably less affected by environmental interference compared to ground-based observations. Space telescopes are not constrained by weather or the day/night cycle however they must contend with orbital motion of the satellite, stray light from the Earth, and scattered sunlight and moonlight. Additionally, basic spacecraft maintenance such as attitude adjustments and stationkeeping interrupt continuous data collection. Space-based observations are often in high demand due to the high ceiling on data quality, however they are also in relatively low supply due to the significant cost of launching and operating space telescopes. Consequently, space-based observations are often primarily constrained by practical limitations rather than environmental limitations. Satellite photometry is often either limited in monitoring duration (e.g. TESS), minimum target brightness (e.g. BRIght Target Explorer (BRITE); Weiss et al., 2014), or sampling (e.g. Hipparcos) such that missions can be kept financially viable while supporting stated mission objectives. While space-based photometry generally demonstrates higher precision and better sampling than ground-based photometry,

they still share many fundamental analytical challenges.

Astronomers have been performing analyses of astronomical time series for many decades and a variety of frequency analysis algorithms can be found in astronomical literature. These are generally based on either the statistical principles of least-squares analysis (Lomb, 1976; Ferraz-Mello, 1981; Scargle, 1982; Reimann, 1994) or Bayesian probability theory (Gregory and Loredo, 1992) and the procedural principles of discrete Fourier analyses (Deeming, 1975; Lomb, 1976; Scargle, 1982; Palmer, 2009) or the minimization of some dispersion metric for data phased according to candidate periods (Stellingwerf, 1978; Dworetsky, 1983; Schwarzenberg-Czerny, 1989; Graham et al., 2013). Comparisons of some period-searching algorithms were presented by Heck et al. (1985), Schwarzenberg-Czerny (1999), and most recently Graham et al. (2013). Schwarzenberg-Czerny (1999) found many of the phase-binning methods to be statistically equivalent, and notably concluded that methods with smooth model functions are generally more sensitive than methods with step functions. The results of Graham et al. (2013) clearly show that there exists no unilaterally superior method and all methods are similarly sensitive to data quality.

## 4.2 The Lomb-Scargle Periodogram

Possibly the most prolific astronomical frequency analysis algorithm was established by the seminal works of Lomb (1976) and Scargle (1982) and is commonly referred to as the Lomb-Scargle (LS) periodogram. The equation given by Scargle (1982) for the LS periodogram $P_{LS}$ as a function of frequency $\omega$[1] (in cycles per day, c/d) associated with a discrete differential time series $X(t)$ was

$$P_{LS}(\omega) = \frac{1}{2} \left[ \frac{\left[\sum_i X_i \cos(\omega(t_i - \tau))\right]^2}{\sum_i \cos^2(\omega(t_i - \tau))} + \frac{\left[\sum_i X_i \sin(\omega(t_i - \tau))\right]^2}{\sum_i \sin^2(\omega(t_i - \tau))} \right], \quad (4.1)$$

where $\tau$ is a time reference point defined by

$$\tan(2\omega\tau) = \frac{\sum_i \sin(2\omega t_i)}{\sum_i \cos(2\omega t_i)} \quad (4.2)$$

---

[1] The notation of $\omega$ for frequency is used here for consistency with the referenced literature, however $f$ is used to represent frequency in all following sections.

and the units of $P_{LS}$ are the same as those for the time series $X(t)$.

The LS periodogram operates on equivalent statistical principles to optimization with respect to parameters $A$ and $B$ in the model function

$$F(t) = A\cos(\omega t) + B\sin(\omega t) \tag{4.3}$$

according to the minimization of the sum-of-squares

$$\sum_i (X_i - F(t_i))^2, \tag{4.4}$$

in the form of an analytical expression. Shortcomings of the original LS periodogram of Lomb (1976) and Scargle (1982) were independently addressed (Gilliland and Baliunas, 1987; Irwin et al., 1989; Cumming et al., 1999) culminating in the (fully) generalized Lomb-Scargle (GLS) periodogram introduced by Zechmeister and Kürster (2009). They first defined normalised weights

$$w_i = \frac{1}{\sigma_i^2 \sum_i \frac{1}{\sigma_i^2}} \tag{4.5}$$

and the sum short forms

$$Y = \sum_i w_i X_i, \tag{4.6}$$

$$C = \sum_i w_i \cos(\omega t_i), \tag{4.7}$$

$$S = \sum_i w_i \sin(\omega t_i), \tag{4.8}$$

$$Y_\tau = Y(t - \tau), \tag{4.9}$$

$$C_\tau = C(t - \tau), \tag{4.10}$$

$$S_\tau = (t - \tau). \tag{4.11}$$

where the time reference point $\tau$ was given by

$$\tan(2\omega\tau) = \frac{2CS}{CC - SS}. \tag{4.12}$$

The (normalized) GLS periodogram $P_{GLS}(\omega)$ for a discrete time series $X(t)$ with measurement errors $\sigma(t)$ was then given by

$$P_{GLS}(\omega) = \frac{1}{YY} \left[ \frac{YC_\tau^2}{CC_\tau} + \frac{YS_\tau^2}{SS_\tau} \right]. \tag{4.13}$$

49

The GLS periodogram makes two key adjustments to the original LS algorithm simultaneously. The first of these is the change to the equivalent of a $\chi^2$ minimization, which properly weights data points according to measurement error and was first addressed by Gilliland and Baliunas (1987) and Irwin et al. (1989). The second adjustment accounts for the potential of the best-fit sinusoid at a given frequency to have a non-zero mean which was first addressed by Cumming et al. (1999). An extensive discussion of LS periodograms, including the GLS improvement, was provided by VanderPlas (2018).

Given the conclusions of Graham et al. (2013), the LS$^2$ periodogram was chosen as the basis for the analyses presented in this work due to its broad adoption and successful application in similar literature and the readily-available Python implementation from the *AstroPy* package.

## 4.3 PyPw - A Python program for Pre-whitening

Frequency analysis algorithms like the LS and GLS periodograms provide a means of characterizing the frequency spectrum of a light curve on a discrete frequency grid. However, this isn't an exceptionally reliable method for measuring the explicit parameters (e.g. frequency, amplitude, phase) of periodic components present in the light curve. Instead, the LS periodogram can be used to guide the direct fitting of sinusoids to the light curve. This is the basis for a LS-based pre-whitening analysis.

A pre-whitening analysis assumes that a light curve can be described as

$$F_{\mathrm{LC}}(t) = F_{\mathrm{CVM}}(t) + N(t), \tag{4.14}$$

where $F_{\mathrm{CVM}}$ is the "complete variability model" and $N(t)$ is the noise and non-periodic variability present in the light curve. The complete variability model is the sum of all periodic signals present in the data. To understand the complete variability model, it's important to first define a single-frequency variability model. This is given in terms of a frequency $f$, an amplitude $A$, and a phase $\phi$ as

$$F_{\mathrm{sf}}(t) = A \sin(2\pi(ft + \phi)). \tag{4.15}$$

---

[2]While a GLS algorithm is used for this analysis, it is done so assuming equal measurement weights for reasons discussed in Sect. 4.3.1. Therefore, the periodograms computed in this work are somewhat more akin to the original LS periodogram or the "floating-mean periodogram" of Cumming et al. (1999) (for which an analytical form was not provided) and are referred to as LS periodograms.

The complete variability model can then be understood as a sum of single-frequency variability models according to Eq. 4.15. For a set of $n$ single-frequency variability models denoted by the index $i$, this is given by

$$F_{\mathrm{CVM}}(t) = C + \sum_1^n A_i \sin(2\pi(f_i t + \phi_i)). \qquad (4.16)$$

The constant term $C$ is included in Eq. 4.16 represents the zero-point offset of the model. With the single-frequency and complete variability models defined, the basic steps of pre-whitening process are

1. compute a periodogram and identify a candidate frequency of interest,
2. determine an optimized single-frequency variability model at the candidate frequency,
3. include the single-frequency variability model in the complete variability model, and
4. generate a residual light curve to use in the next iteration.

The pre-whitening process is ideally conducted until the residual frequency spectrum consists only of noise. In reality, the noise of residual light curves contain a mix of instrumental and environmental noise often with real signal of comparable amplitude to the noise. It's therefore more appropriate to say the residual light curve is assumed to define the noise of the light curve in the context of the frequency analysis. Determining when to halt the iterative procedure therefore is an important and reasonably challenging consideration, and this is further discussed in Sect. 4.3.4.

To analyze the CoRoT and TESS light curves for HD 47129, a new pre-whitening program was developed. Before describing this program, it is pertinent to discuss why it was developed at all, particularly when there exist pre-whitening programs that are freely available to the public, robust, well-tested, and reasonably easy to use (e.g. Period04; Lenz and Breger, 2005). The primary reasoning behind this is that Plaskett's Star demonstrates complex photometric variability compared to most stars; its light curves are dominated by strong ($\sim 20$ mmag) variability at the BLC rotational period and harmonics, while also clearly demonstrating weaker ($\sim 5$ mmag) variability at multiple frequencies including the orbital period. The strong variability, while scientifically significant, is easily detected and already reasonably well-characterized. The current scientific interest, however, is in the weaker variability which consists of several seemingly unrelated frequencies and is of unknown physical origin. The development of a new pre-whitening implementation enabled the testing of several adjustments and modifications in the interest of addressing

the specific challenges with the light curves of HD 47129.

The pre-whitening program developed for this thesis is called Python program for Pre-Whitening (PyPW)[3]. It is a command-line tool implemented in Python 3 (version 3.7+) and makes use of the NumPy[4] package (Harris et al., 2020) for general computation, SciPy[5] and LMFit[6] packages (Virtanen et al., 2020; Newville et al., 2014) for optimization, Matplotlib[7] package (Hunter, 2007) for data visualization, and the AstroPy[8] package (Astropy Collaboration et al., 2022) for computation of LS periodograms.

### 4.3.1   Pre-whitening Procedure

Prior to performing any analyses, the PyPW program converts the data into a differential light curve. The light curves analyzed for both TESS and CoRoT were kept in units of electrons/s as it is a linear scale, compared to the logarithmic magnitude scale (which only approximates a linear scale for small differential magnitudes). All results were converted to a differential magnitude after the analysis for easier presentation and interpretation.

**Stage 1 - Periodogram Computation and Peak Selection**

The first stage of each iteration was to compute a periodogram for the residual light curve (or original light curve, for the first iteration). A frequency grid was first defined with 50 points per frequency resolution element spanning from the minimum frequency resolution (see Sect. 4.3.2 for a discussion of frequency resolution) to an upper bound at 10 c/d.

Before proceeding, it's important to take a moment to remark on the Nyquist frequencies of the data concerned in this work. The Nyquist frequency is the limiting frequency above which signals will be necessarily undersampled, and for an evenly-sampled timeseries with no gaps it's given as half the sampling frequency. This can be understood as requiring at least two data points per cycle for a given signal to avoid undersampling, and signals at frequencies higher than the Nyquist frequency will suffer from aliasing. The

---

[3]The source code for PyPW is available at `https://github.com/erikstacey/pypw`.
[4]`https://numpy.org/doc/stable/`
[5]`https://docs.scipy.org/doc/scipy/`
[6]`https://lmfit.github.io/lmfit-py/`
[7]`https://matplotlib.org/stable/index.html`
[8]`https://docs.astropy.org/en/stable/index.html`

Nyquist frequency for the TESS photometry at a sampling rate of 2 minutes is approximately 360 c/d, and the CoRoT photometry is approximately 1440 c/d. In periodograms computed up to frequencies of 2000 c/d, no significant variability is observed above frequencies of 10 c/d based on a manual inspection with the exception of a group of known systematics in the CoRoT photometry (CoRoT systematics in the HD 47129 photometry; Mahy et al., 2011). In light of this, aliasing due to undersampling was not expected to be an issue in this analysis and periodograms were computed spanning 0-10 c/d.

The *AstroPy* LombScargle function[9] was used to compute an unnormalized power spectral density (PSD) peridogram and it was converted from a power spectrum to an amplitude spectrum. In order to ensure the amplitude spectrum had meaningful units, the periodogram was computed without taking into account errors in flux. The flux errors were similar across the entire light curve for both sets of satellite photometry and the parameters measured from the periodogram are further refined in stages 2 and 3 according to a $\chi^2$ minimization, therefore flux errors were omitted while computing the LS periodogram. The benefit of this was that the periodogram amplitudes at each frequency provided reasonably good input values for the single frequency optimization in the next stage. The primary consequence of this is thought to lie in spurious data points that are potentially overweighted, which is expected to introduce additional power very near 0 c/d and below the lower bound of the computed periodograms.

The primary objective of this stage is to identify a frequency and its corresponding amplitude around which to build a single-frequency variability model. It's common for pre-whitening analyses to select the highest amplitude on the frequency spectrum and use its corresponding frequency (the highest-amplitude peak selection criterion). This program uses an adjusted peak selection algorithm based on this approach which is further discussed in Sect. 4.3.5. An example of a computed periodogram with a peak selected is illustrated in Fig. 4.1.

**Stage 2 - Single-Frequency Optimization**

The second stage of each iteration was to determine a single-frequency model corresponding to the frequency/amplitude pair determined in stage 1. This

---

[9]Documentation on the *AstroPy* LombScargle function can be found at `https://docs.astropy.org/en/stable/timeseries/lombscargle.html`.
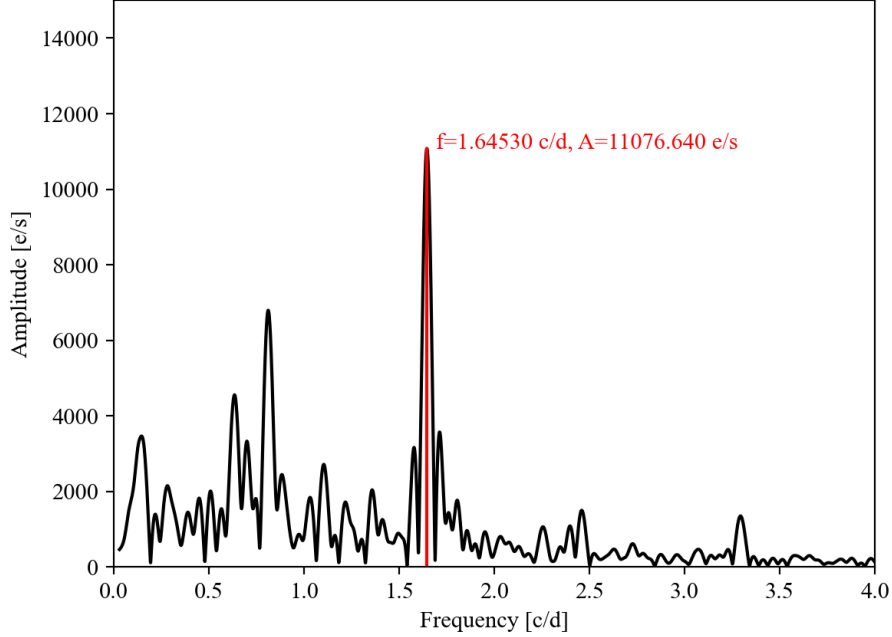
Figure 4.1: The periodogram from the first iteration of the analysis of the detrended TESS data. The red vertical line indicates the frequency selected during stage 1 of this iteration.

stage performs a minimization of a single-frequency variability model described by Eq. 4.15 on the residual light curve[10]. The frequency and amplitude from the periodogram are used as initial parameter guesses alongside a provisional phase of 0.5. An example of initial and optimized models from this stage is depicted in 4.2. This stage yields an optimized single-frequency variability model at each iteration, which is added to the complete variability model.

The choice of provisional phase at 0.5 is arbitrary. However, if the resultant optimized phase is close to the provisional phase (within 0.1), it is possible the optimization algorithm has identified a local $\chi^2$ minimum as a result of the

---

[10]The first iteration will have this step performed on the original (non-residual) light curve, as the resultant model will then be subtracted from the original light curve to yield the first residual light curve.
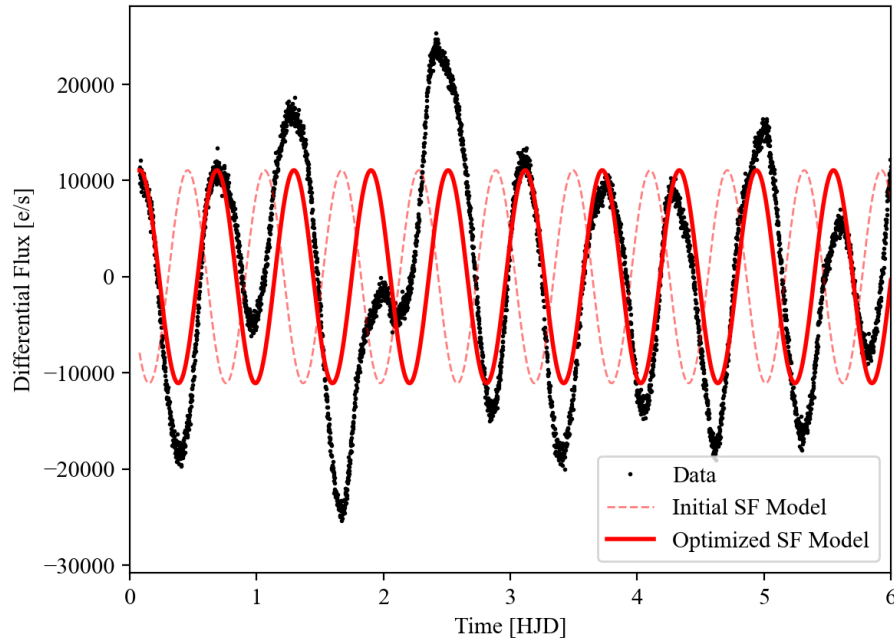
Figure 4.2: An illustration of the optimization of the single-frequency model. It is clear from the initial model that the frequency and amplitude were reasonably well-estimated directly from the periodogram. This illustrates the purpose of this step, which is to *determine* the phase and *refine* the frequency and amplitude of the periodic component identified in this iteration.

assigned provisional phase. In this case, the provisional phase is adjusted to 0.67 and the single-frequency optimization is retried. This is repeated, adding 0.17 to the provisional phase each time, until the optimized phase differs from the provisional phase by at least 0.1. Of course, this doesn't *exclude* phases in the interval [0.4, 0.6] from the optimization and just requires that optimized phases in that interval are confirmed by an optimization or optimizations with differing provisional phases.

## Stage 3 - Multi-Frequency Optimization

The third stage of each iteration refines the complete variability model following the addition of the single-frequency component identified in stage 2. To

do so, a $\chi^2$ minimization of Eq. 4.16 was performed against the original light curve with initial parameters as identified in previous iterations or, in the case of the newest single-frequency model, as identified in stage 2. The intention of this step is to refine the parameters of previously identified components given the addition of a new single-frequency component. As such, the frequencies and amplitudes are constrained to remain within ±20% of their initial values and the phase is limited to the interval [-100, 100][11]. This stage produces an optimized complete variability model and an example is depicted in Fig. 4.3.
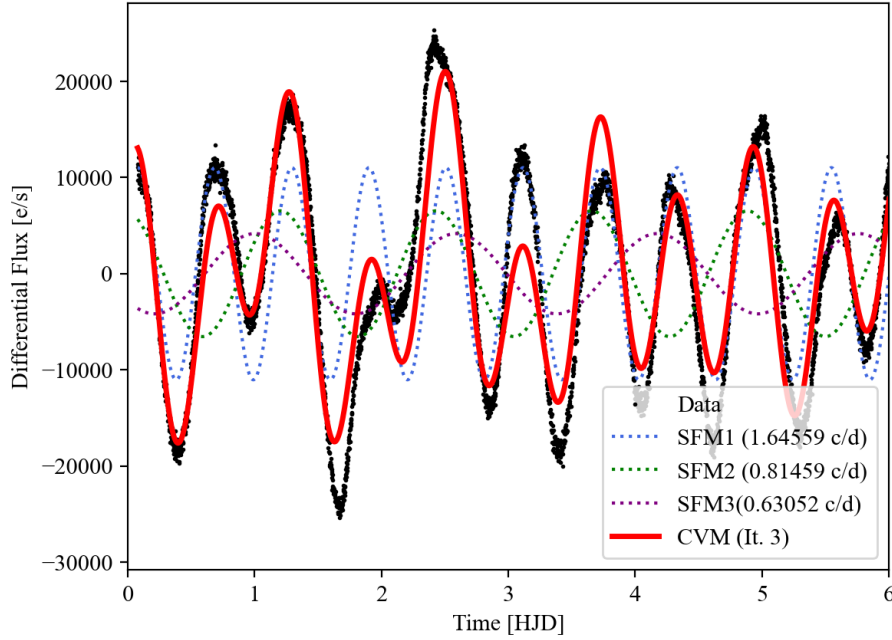


Figure 4.3: The optimized complete variability model (CVM) from stage 3 of the third iteration of the analysis of the detrended TESS data. The dotted lines indicate the single-frequency model (SFM) constituents of the complete variability model. The frequencies of the single-frequency models are shown in the legend.

---

[11]The program converts phases to equivalent values in the interval (0, 1) after the optimization.

**Stage 4 - Generation of a Residual Light Curve**

The final stage is to generate a residual light curve for the next iteration. The complete variability model is subtracted from the residual light curve to generate the new residual light curve (see Fig. 4.4). This light curve is passed to the next iteration and used to determine the next single-frequency variability model.
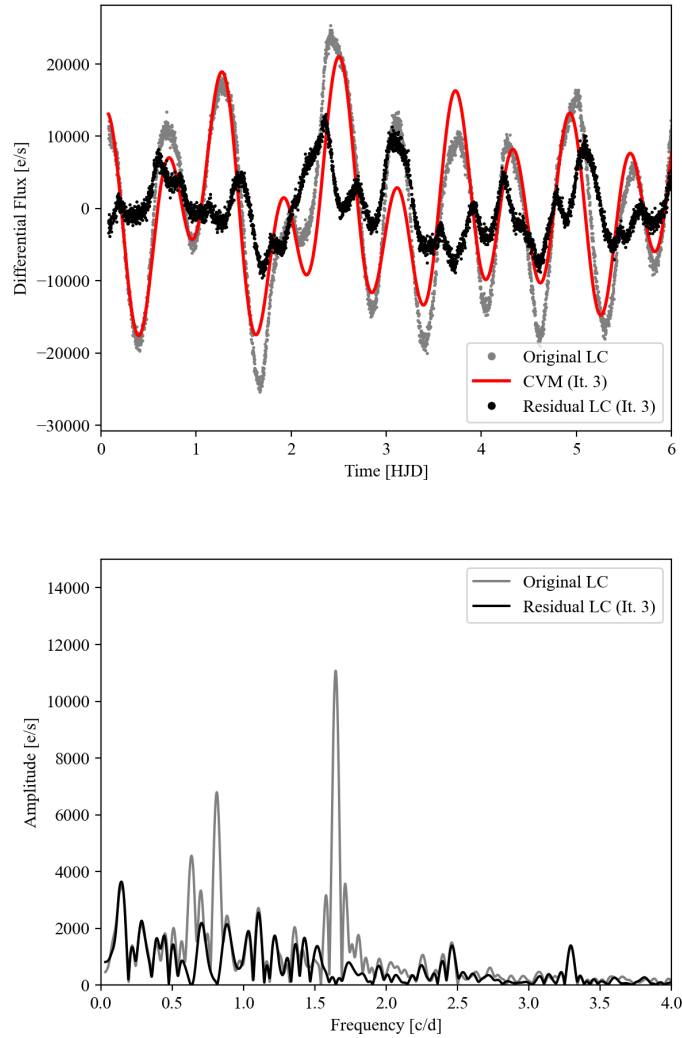
Figure 4.4: (Top) An example of the generation of a residual light curve in the analysis of the detrended TESS data. The complete variability model (CVM) described in Fig. 4.3 is subtracted from the original light curve to yield the residual light curve. (Bottom) The LS periodograms of the original and residual light curve. The periodogram of the residual light curve is missing the three highest-amplitude peaks of the original light curve, which were identified and removed by the first three iterations of pre-whitening.

### 4.3.2 Remarks on Frequency Resolution

A natural question that arises when conducting period searches in multiperiodic light curves is that of resolution: How close in frequency can two periodic components be while still being distinguishable? This can be understood by first considering the addition of two sinusoids at equal frequency to form a single sinusoid at the same frequency:

$$A\sin(fx + \phi) = A_1\sin(fx + \phi_1) + A_2\sin(fx + \phi_2). \qquad (4.17)$$

In the simple case where the two sinusoids are in phase, Eq. 4.17 will reduce to

$$A\sin(fx + \phi) = (A_1 + A_2)\sin(fx + \phi) \qquad (4.18)$$

which implies

$$A = A_1 + A_2. \qquad (4.19)$$

Were one to measure the combined sinusoid, it would be impossible to decompose it into its original constituents as $A_1$ and $A_2$ can take on infinitely many values so long as Eq. 4.19 holds true. It is trivial to extend this argument to summed sinusoids at different phases; the resultant sinusoid will have a single phase parameter, and therefore it can be decomposed into infinitely many amplitude pairs satisfying Eq. 4.19 at the same phase. This phenomenon is approximated in short time intervals for summed frequencies which are *close* in frequency, however over long time intervals the relative phasing between the two will drift and the constituent frequencies will become apparant. Therefore, the maximum frequency resolution of a time series is primarily determined by its length. The Rayleigh resolution criterion of $1/\Delta T$, where $\Delta T$ is the time baseline of the time series, has been commonly employed as a measure of the minimum separation in frequency necessary to resolve two adjacent frequencies. Loumos and Deeming (1978) argued this to be insufficient based on empirical testing and recommended a frequency resolution of $1.5/\Delta T$ instead, which is adopted for this work.

The frequency resolution element has technical implications as well. An issue observed in earlier iterations of the program was related to adjacent frequencies within a resolution element of one another. Particularly, when the multi-frequency optimization was performed, single-frequency models would demonstrate abnormally high and clearly unphysical amplitudes while the complete variability model fit the data reasonably well. Furthermore, if boundaries were enforced on the amplitudes, the optimization would regularly produce amplitudes at or very near the enforced boundaries. This illustrated

59

the need to prevent the *selection* of multiple frequencies within a resolution element of one another. This was ultimately solved by the improved peak selection algorithm described in Sect. 4.3.1, which tended not to make selections leading to this issue, however peak identification was nevertheless explicitly adjusted such that frequencies within $1.5/\Delta T$ of already-identified frequencies were excluded from potential selection.

### 4.3.3 Determining Uncertainty on Frequencies, Amplitudes, and Phases

In Sect. 4.1 it was established that stellar light curves diverge from common statistical assumptions in general time series analysis. For this reason, traditional time series analysis techniques are unreliable for period searching in stellar light curves. It is therefore unsurprising that the determination of uncertainties on extracted parameters similarly requires additional consideration. While the residual light curve from the pre-whitening analysis is assumed to be noise, it typically demonstrates a strong stochastic component and therefore has strong point-to-point correlations. Schwarzenberg-Czerny (1991) showed that the assumption of white noise residuals will lead to the underestimation of uncertainties where such correlation is present. Simultaneously, they argue that estimates based on the Rayleigh resolution criterion (or similar statistical principles) are insensitive to the quality of the data and provide only an upper limit on frequency uncertainties.

Montgomery and O'Donoghue (1999) provided the following set of equations for the estimation of one-sigma uncertainties on frequencies ($\sigma_f$), amplitudes ($\sigma_A$), and phases ($\sigma_\phi$) for sinusoidal models determined through least-squares fitting:

$$\sigma_f = \sqrt{\frac{6}{N}} \left( \frac{\sigma_m}{\pi \Delta T A} \right) \tag{4.20}$$

$$\sigma_A = \sqrt{\frac{2}{N}} \sigma_m \tag{4.21}$$

$$\sigma_\phi = \sqrt{\frac{6}{N}} \left( \frac{\sigma_m}{A} \right). \tag{4.22}$$

Eqs. 4.20-4.22 are dependent on the number of observations $N$, the standard deviation of the residual light curve $\sigma_m$, the time baseline of the time series $\Delta T$, and the amplitude $A$. These are derived under the assumption of white noise and therefore Montgomery and O'Donoghue (1999) concluded these

formulae understimate the true statistical uncertainties (consistent with the conclusions of Schwarzenberg-Czerny, 1991). Schwarzenberg-Czerny (1991) (also see Schwarzenberg-Czerny, 2003) established that consecutive correlated points are statistically equivalent to a single data point. If the average number of consecutive correlated points in a noise model is $\rho$, the effective number of data points in a noise model is thereby reduced by a factor of $\rho$. Therefore, the issue with correlation of the Montgomery and O'Donoghue (1999) equations (Eqs. 4.20-4.22) is eliminated by the adoption of a reduced effective $N$ given by

$$N_{eff} = N/\rho. \tag{4.23}$$

The Montgomery and O'Donoghue (1999) equations with the Schwarzenberg-Czerny (1991)/Schwarzenberg-Czerny (2003) correction was used for the analysis of a large sample of B-type pulsating stars observed by CoRoT (Degroote et al., 2009b,a) and was adopted for this analysis as well.

### 4.3.4 Assessing the Significance of Measured Frequencies

In a LS pre-whitening analysis, real periodic components are identified through strong peaks in the periodogram of a time series. However, noise in a finite-length time series also introduces peaks into the associated periodogram. This is depicted in the periodogram of white noise illustrated in Fig.4.5, which could be analyzed to extract several frequencies. Higher amplitude peaks are, however, less likely to arise from statistical fluctuations for a given noise level. Distinguishing real signal from peaks (likely) introduced by statistical fluctuations therefore becomes a comparison of signal (the amplitude of the signal) to noise (the amplitude of peaks associated with the residual light curve, assumed to be noise). As discussed in Sect. 4.3.3, the residual light curve doesn't necessarily correspond to white noise and therefore the average power in noise is generally a function of frequency. It is therefore ideal to evaluate the expected noise amplitude at or around any potential signals when performing an assessment of the signal to noise ratio (SNR).

Establishing the noise level as a function of frequency can be approached in a variety of ways. If the distribution is known or assumed (e.g. white noise), it is trivial to perform a fit and establish the noise function. However, the general case where the noise doesn't follow a well-known distribution is more challenging. For example, a common solution is to consider the average amplitude on the periodogram in a region around each potential frequency (Burssens et al., 2020; Lenz and Breger, 2005). The choice is generally subjective and dependent on the characteristics of the light curve, which is also
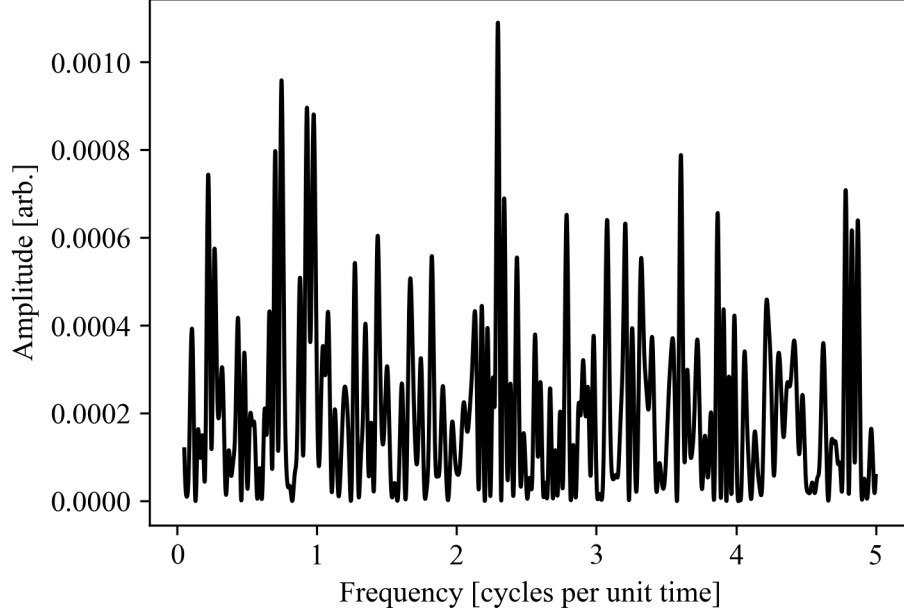
Figure 4.5:   A LS periodogram of 10 000 randomly sampled gaussian-distributed points evenly sampled across 30 days.

subjectively dependent on the analyzer's distinction of noise and signal.

In order to ensure the significance of detected frequencies were well-characterized, two methods of significance estimation were used. The first of these was a fit to the final residual periodogram according to the SLF model of Bowman et al. (2019b) (also see Bowman et al., 2019a, 2020). This model is given by

$$\alpha(f) = \frac{\alpha_0}{1 + \left(\frac{f}{f_{\mathrm{char}}}\right)^{\gamma}} + C_w, \tag{4.24}$$

where $\alpha_0$ is the amplitude at zero frequency, $f_{\mathrm{char}}$ is the characteristic frequency, and $\gamma$ is the logarithmic amplitude gradient. The first term represents red (Brownian) noise while the second term $C_w$ represents a constant white noise. The second method determines the local minima on either side of a frequency peak, then takes the average periodogram amplitude in $\Delta f = 0.5$ c/d regions on either side of the peak to determine a local noise level for that frequency. Note that while the SLF variability is treated as noise in this

analysis, it is actually a phenomenon thought to arise from stellar pulsations driven by gravitational (and buoyant) restoring forces. Therefore, the SLF variability represents real, physical variations in brightness of the star. Due to the stochastic nature of these variations, they conflate the detection of well-defined signals and it is appropriate to treat the SLF spectrum as a noise spectrum.

When concerned with Gaussian statistics, a SNR exceeding three ($3\sigma$) is usually sufficient to confidently report a statistically significant detection, corresponding to a 99.7 % confidence the observed phenomenon did not arise due to chance statistical fluctuations. However, stellar light curves typically demonstrate departures from Gaussian statistics (in ways that are challenging to account for analytically) and therefore a more conservative and empirical SNR criterion of $\geq 4$ is typically used. This was established by Breger et al. (1993) and has since been adopted by the broader scientific community for performing frequency analyses of stellar light curves (Degroote et al., 2009a). As this analysis considered two methods of estimating SNR, frequencies were provisionally accepted if *either* measurement exceeded the Breger et al. (1993) $4\sigma$ criterion. It is important to stress, however, that frequencies which only satisfy this criterion by one of the two SNR measurement methods must be carefully considered and ideally supported by additional contextual evidence (e.g. apparent membership in a harmonic structure).

### 4.3.5 Peak Selection

Stage 1 of each pre-whitening iteration involves the selection of a candidate frequency from the LS periodogram. This candidate frequency, and its corresponding amplitude, are passed to Stage 2 as initial values for the single-frequency model optimization. This frequency selection plays an important role in the development of a complete variability model, as the single-frequency and multi-frequency minimization steps act to *refine* the frequencies identified in this stage. A simple approach to pre-whitening is to simply select the frequency corresponding to the highest amplitude on the periodogram at each stage (a highest-amplitude peak selection criterion). For an ideal timeseries demonstrating purely white noise, this is an effective solution as it's equivalent to selecting frequencies according to maximum SNR. Even for light curves departing from the ideal white-noise case, a highest-amplitude approach will identify most or all of the variability of interest in most cases.

Plaskett's Star demonstrates strongly frequency-dependent noise due to

the SLF variability discussed in Sect. 4.3.4. The amplitude of quasi-periodicity introduced by the SLF noise can be much higher than the amplitude of peaks in regions of the spectrum where there is much less noise. An example from this analysis is illustrated in Fig. 4.6, and using only a highest-amplitude peak selection criterion would either miss these peaks or identify many quasi-periodic signals from the SLF noise. Plaskett's Star therefore demands a more sophisticated peak selection algorithm to perform a rigorous frequency analysis.
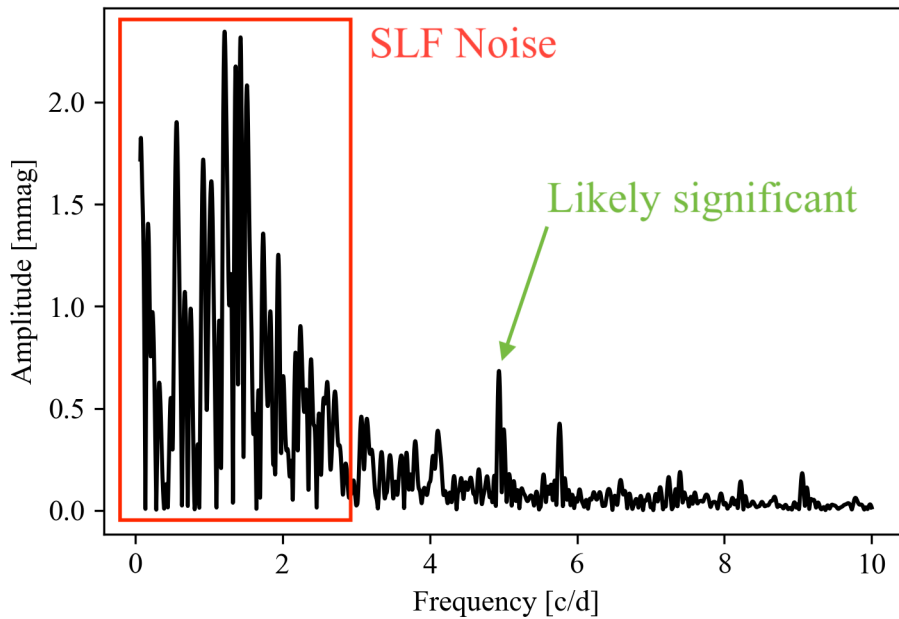


Figure 4.6: An example periodogram from the 12th pre-whitening iteration of the detrended TESS data. A red box indicates a region that is certainly dominated by SLF variability. The green arrow indicates a peak of lesser amplitude than the SLF variability which appears qualitatively significant (and was ultimately detected significantly).

PyPW takes a hybrid approach to peak selection. The first several frequencies are identified and extracted according to highest-amplitude. This removes the power they introduced to the LS periodogram and permits a reasonable estimation of a pseudo-noise level. Once the strongest frequencies are

removed, frequencies are still selected according to highest-amplitude however with the additional condition that they must exceed a provisional noise model by at least $3\sigma$. This is henceforth referred to as the peak selection significance criterion. The provisional noise model is given by a fit assuming a SLF model at each iteration and performed prior to peak selection. If no frequencies are found which satisfy this condition, the analysis is concluded. For both the TESS and CoRoT data, it was found to be optimal to impose this additional condition after 10 frequencies were identified.

## 4.4   Testing and Validation

PyPW was primarily validated against Period04, an open-source, multi-platform, GUI-based, well-documented frequency analysis tool for astronomical time series analysis (Lenz and Breger, 2005). Period04 has been extensively used in many publications and is considered very reliable and robust. It is functionally similar to PyPW, making it a highly suitable benchmark to test against. Contrary to PyPW, however, it is a semi-manual tool requiring some degree of instruction for each stage of each iteration. Therefore, comparison with this tool cannot be used to verify steps that are ultimately left up to the end user by Period04, such as frequency selection methodology. Therefore, a basic pre-whitening was performed with both Period04 and PyPW to identify the first 10 frequencies in the detrended TESS light curve with highest-amplitude peak selection (see Table 4.1). Worst-case fractional differences between the two were of the order $10^{-4}$ for frequencies, $10^{-2}$ for amplitudes, and $10^{-4}$ for phases. These are all generally neglegible given the measurement uncertainties. Notably, the uncertainties assessed by PyPW and Period04 differ significantly despite the similarity of the nominal values. Period04 uses the original equations from Montgomery and O'Donoghue (1999) to compute formal uncertainties whereas PyPW uses the Montgomery and O'Donoghue (1999) equations with the Schwarzenberg-Czerny (1991)/Schwarzenberg-Czerny (2003) adjustment, easily accounting for the difference in formal uncertainties.

The frequencies measured in this analysis are also consistent with the results of Burssens et al. (2020) for the TESS data and the results of Mahy et al. (2011) for the CoRoT data. It's important to note, however, that this analysis identifies more frequencies in the TESS data than the analysis of Burssens et al. (2020) and (many) fewer frequencies than analysis of Mahy et al. (2011) due to differences in choice of termination criteria. However, all frequencies appearing in the Burssens et al. (2020) analysis appear in the sample pre-

| I | Frequency [c/d] | Amplitude [mmag] | Phase | Frequency [c/d] | Amplitude [mmag] | Phase |
|---|---|---|---|---|---|---|
| 1 | 1.64542(33) | 17.56(22) | 0.634(13) | 1.64542(94) | 17.575(65) | 0.63432(59) |
| 2 | 0.80884(51) | 11.34(22) | 0.847(20) | 0.80880(14) | 11.358(65) | 0.84726(91) |
| 3 | 0.63524(97) | 6.05(23) | 0.023(38) | 0.63523(27) | 6.065(65) | 0.0230(17) |
| 4 | 0.1387(10) | 5.77(23) | 0.652(40) | 0.13867(29) | 5.773(65) | 0.6525(18) |
| 5 | 1.1041(12) | 4.65(23) | 0.190(49) | 1.10404(36) | 4.651(65) | 0.1909(22) |
| 6 | 0.7129(11) | 5.00(23) | 0.958(46) | 0.71298(33) | 5.017(65) | 0.9576(21) |
| 7 | 0.2858(15) | 3.88(23) | 0.845(59) | 0.28581(43) | 3.878(65) | 0.8450(27) |
| 8 | 0.3907(16) | 3.59(23) | 0.861(64) | 0.39060(46) | 3.580(65) | 0.8610(29) |
| 9 | 0.4416(19) | 3.10(23) | 0.494(74) | 0.86993(55) | 3.034(65) | 0.0471(34) |
| 10 | 0.8700(19) | 3.03(23) | 0.045(76) | 0.44145(54) | 3.087(65) | 0.4959(34) |

Table 4.1: The results of a basic frequency analysis using PyPW (left) and Period04 (right). The I column indicates which iteration the corresponding frequencies were detected.

sented in this work, and all frequencies measured in this work appear in the results of Mahy et al. (2011).

# 5 Frequency Analysis of TESS and CoRoT Data

Frequency analyses were performed using the PyPW program for the detrended TESS data, the SAP TESS data, and the CoRoT data. The numerical results are presented in Tables 5.1, 5.2, and 5.3 for the detrended TESS data, TESS SAP data, and CoRoT data respectively. It was found that adjusting various parameters of the PyPW program could substantially affect both the quantity, precision, and in some cases even the nominal values of the results. Both increasing the number of peaks selected according to strictly the highest-amplitude criterion (with no peak selection significance criterion) and decreasing the minimum required significance criterion caused the program to identify frequencies in the 0-2 c/d range thought to be related to SLF variability. Furthermore, the formal uncertainties are dependent on the standard deviation of the residual light curve which itself is dependent on how many frequencies were extracted. Extracting too many frequencies can also lead to the overestimation of significances as power is removed from the residual periodogram. For these reasons, special focus was placed on appropriately tuning the program for the light curves of Plaskett's Star. It was determined that selecting 10 frequencies prior to enforcing a peak selection significance criterion, set to require a minimum significance of 3, maximally identified variability with real narrow-band periodic signal while avoiding peaks likely associated with SLF variability.

Considering all three light curves, the majority of the variability is represented by the first 7 to 8 frequencies. Of these, two are particularly dominant and generally define the shape of the light curves. This is particularly well-illustrated by the evolution of the light curve across 8 pre-whitening iterations as illustrated in Fig. 5.1. There appears to be a significant red noise component in the frequency spectra spanning approximately 0-2 c/d. A qualitative

assessment of the residual light curves suggests coherent variability is still present therein (see Figs. 5.2, 5.3), however this is only apparent due to the stochastic nature of the red noise. The residual light curves had standard deviations of approximately 5 mmag for the detrended TESS data, approximately 5.8 mmag for the SAP TESS data, and approximately 6.9 mmag for the CoRoT data. From the fits to the residual periodograms (e.g. Fig. 5.2, bottom panel), it is apparent that variability which is plausibly real has been identified and frequencies likely associated with SLF variability have been generally preserved. This is an important part of ensuring appropriate estimation of the formal uncertainties and significances.

The final complete variability models appear to fit the data reasonably well, as shown in Figs. 5.5, 5.6, and 5.7. Closer fits can be achieved through extracting additional frequencies, however this is argued to be equivalent to overfitting the data. Deriving an argument from the Fourier theorem, any data can be closely fit using sufficiently many summed sinusoids, however their individual parameters will be meaningless if the data is inherently non-periodic.
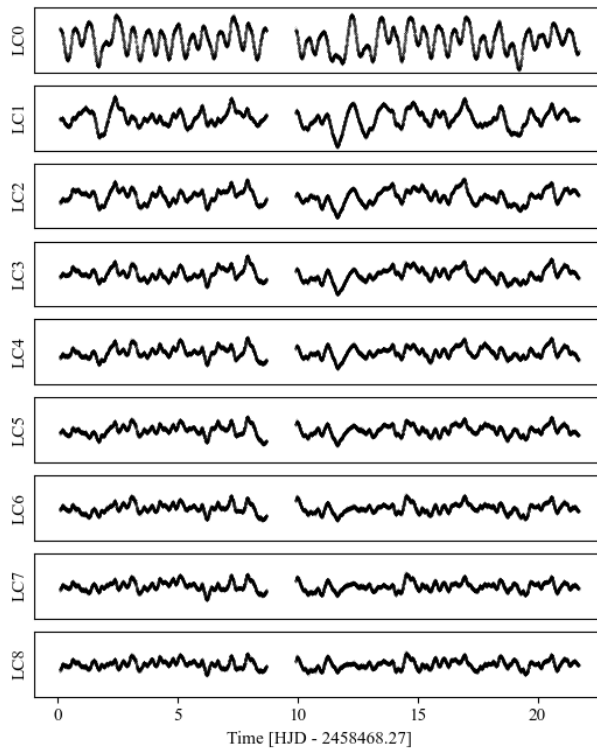
Figure 5.1: The residual light curves from the first eight pre-whitening iterations of the detrended TESS data. Each panel spans ±50 mmag and is annotated on the y-axis with a number. LC0 corresponds to the initial light curve, and the numbers 1 through 9 indicate the corresponding light curve was the residual from that iteration (e.g. LC1 is the residual light curve from the first iteration).

69
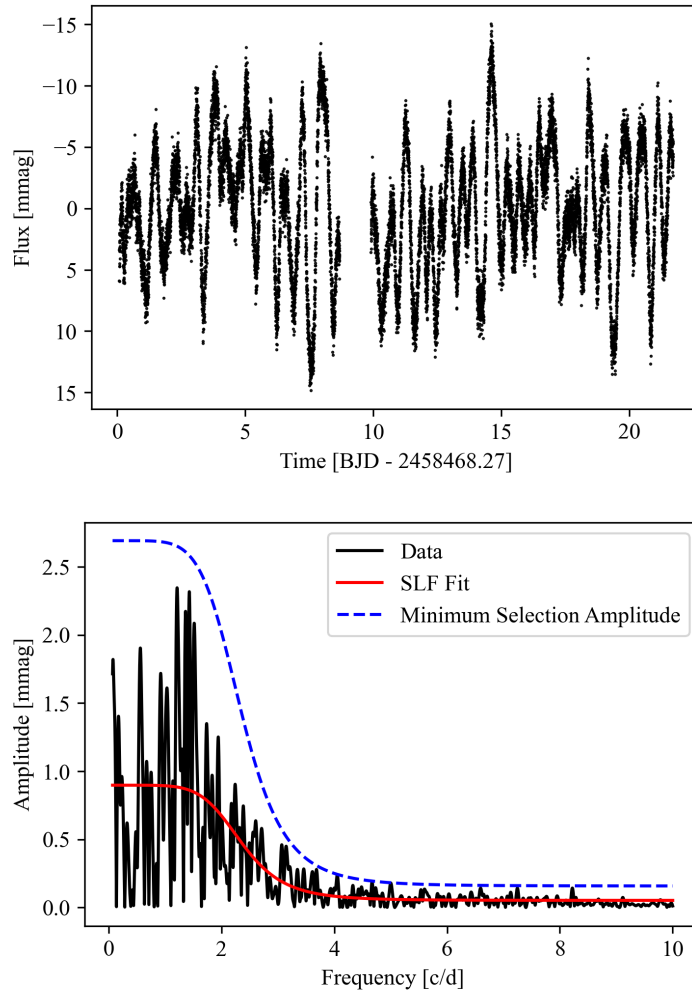
Figure 5.2: (Top) The residual detrended TESS light curve from the frequency analysis. (Bottom) The periodogram of the residual detrended TESS light curve from the frequency analysis. The red line indicates the SLF noise fit, while the blue dashed line indicates the minimum threshold for the acceptance of a potential peak. As this is the final residual periodogram, no peaks exceed the minimum threshold for acceptance and this confirms the analysis was appropriately terminated.
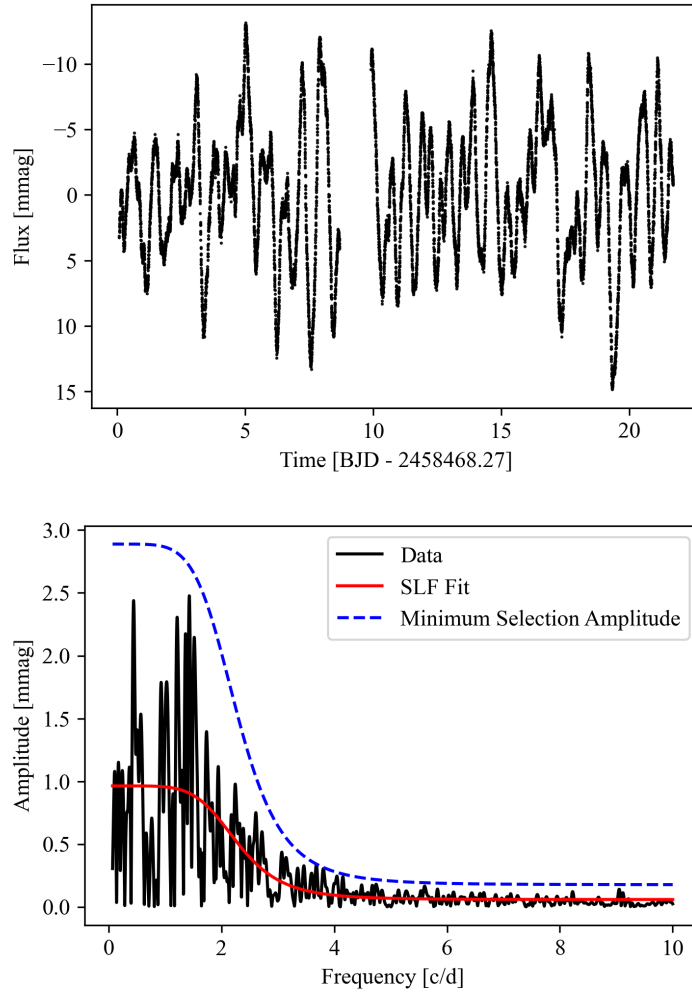
Figure 5.3: Same as Fig. 5.2 for the SAP TESS data.
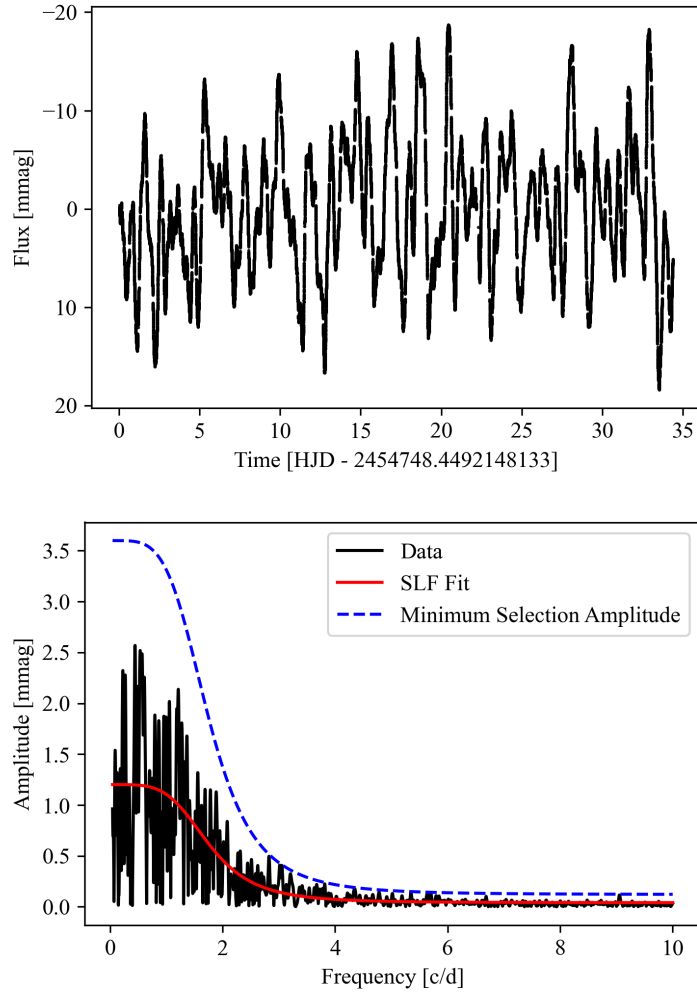
Figure 5.4: Same as Fig. 5.2 for the CoRoT data.
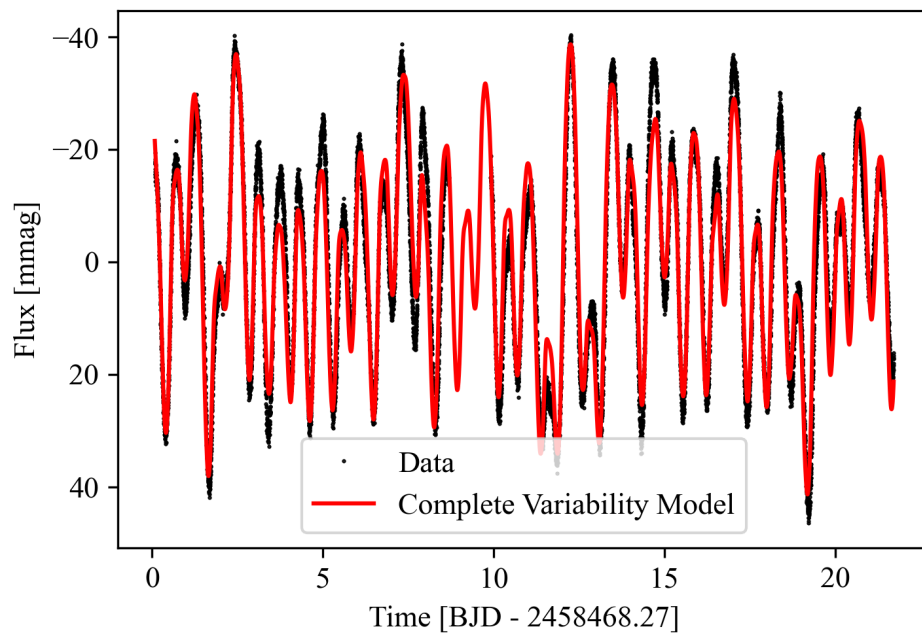
Figure 5.5: The final complete variability model fit to the detrended TESS light curve.
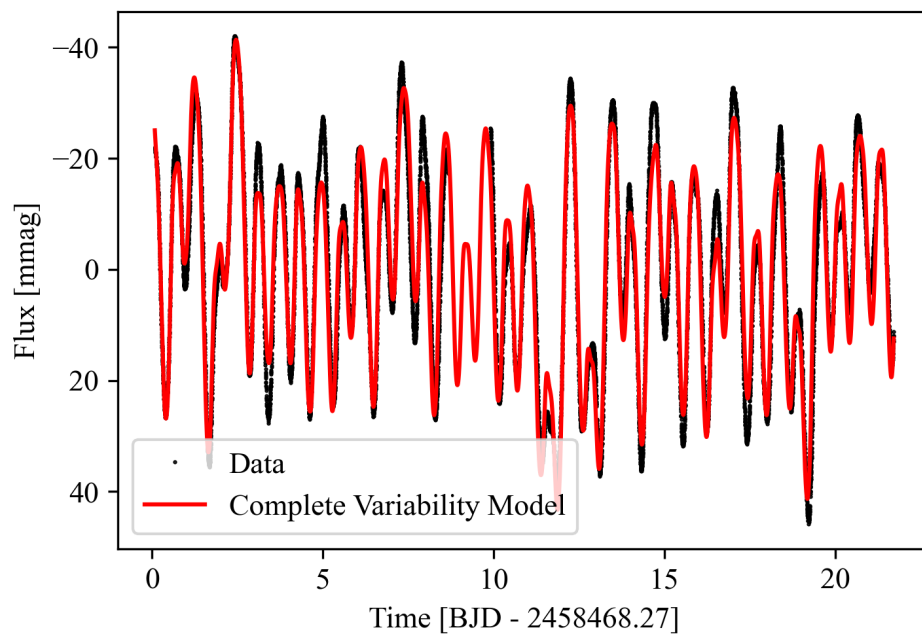
Figure 5.6: The final complete variability model fit to the TESS SAP light curve.
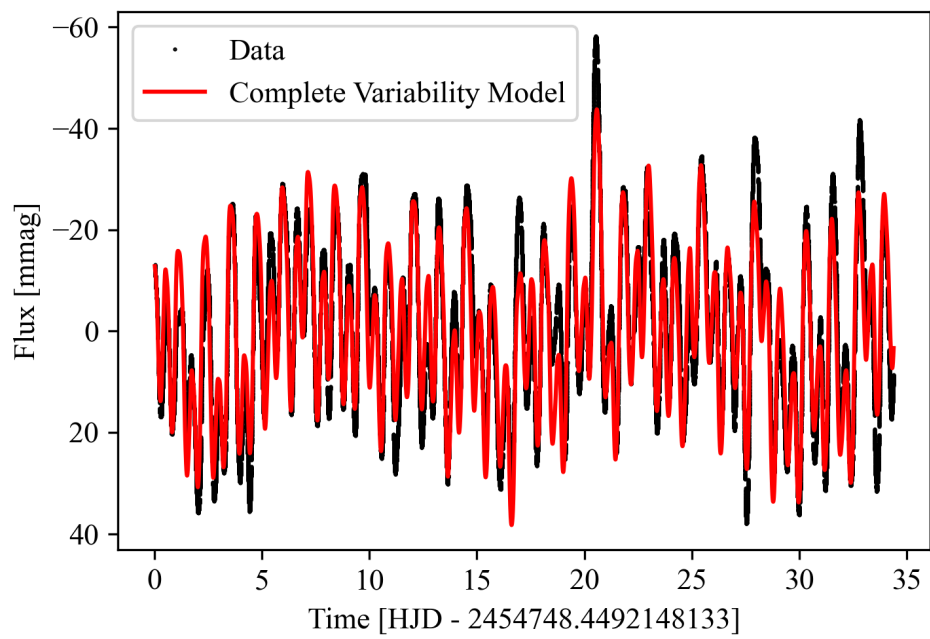
Figure 5.7: The final complete variability model fit to the CoRoT light curve.

## 5.1 Numerical Results

Twenty frequencies were extracted from the detrended TESS data, fourteen of which were identified to be significant and are detailed in Table 5.1. Of the fourteen significantly detected frequencies, two are clearly dominant and responsible for the majority of the observed variability. These correspond to periods of $1.23606 \pm 0.00069$ d and $0.60774 \pm 0.00011$ d. The latter appears to be a harmonic of the former, and several additional harmonic frequencies are detected with intermediate to high significance. This structure is likely associated with the rotation of the BLC based on the period inferred by Grunhut et al. (2022). Two frequencies appeared as though they may be associated with orbital motion of the system. The fundamental frequency is not detected, however, and these all lie within the noisy 0.1-0.4 c/d region (where they may be easily conflated with noise peaks within the frequency resolution). Therefore, it was not possible to establish a reliable association with orbital modulation based on this data alone. Four additional significant frequencies were detected for which the physical origin was not immidiately apparent.

| Index | Frequency [c/d] | Amplitude [mmag] | Phase | Sig. (SLF) | Sig. (Avg.) | Remarks |
|---|---|---|---|---|---|---|
| 2 | 0.80902(45) | 11.34(20) | 0.839(17) | 12.7 | 13.9 | $f_{\rm rot,BLC}$ |
| 1 | 1.64543(29) | 17.56(19) | 0.623(11) | 21.69 | 19.29 | $2f_{\rm rot,BLC}$ |
| 12 | 2.4631(24) | 2.14(20) | 0.093(94) | 5.11 | 5.45 | $3f_{\rm rot,BLC}$ |
| 11 | 3.2940(23) | 2.17(20) | 0.918(93) | 14.72 | 12.3 | $4f_{\rm rot,BLC}$ |
| 15 | 4.098(13) | 0.37(20) | 0.43(54) | 4.71 | 3.69 | $5f_{\rm rot,BLC}$ |
| 13 | 4.9393(73) | 0.70(20) | 0.88(28) | 11.43 | 9.62 | $6f_{\rm rot,BLC}$ |
| 14 | 5.763(12) | 0.42(20) | 0.26(48) | 7.51 | 7.09 | $7f_{\rm rot,BLC}$ |
| 20 | 9.056(27) | 0.19(20) | 0.442(89) | 3.51 | 6.89 | $11f_{\rm rot,BLC}$ |
| 4 | 0.13872(88) | 5.81(20) | 0.652(34) | 6.49 | 7.8 | $2f_{\rm orb}$? |
| 7 | 0.2855(13) | 3.82(20) | 0.846(53) | 4.26 | 5.19 | $4f_{\rm orb}$? |
| 3 | 0.63516(84) | 6.14(20) | 0.020(32) | 6.85 | 8.6 | |
| 6 | 0.7132(10) | 4.95(20) | 0.953(40) | 5.52 | 6.79 | |
| 5 | 1.1042(11) | 4.64(20) | 0.181(43) | 5.22 | 4.54 | |
| 8 | 0.3910(14) | 3.49(20) | 0.854(58) | 3.89 | 5.21 | |

Table 5.1: The significant frequencies of photometric variability identified in the detrended TESS data. The significance (Sig.) is shown assuming both a SLF noise model and a box average noise model. Three frequencies are only identified as significant in one of the two significance tests shown.

| Index | Frequency [c/d] | Amplitude [mmag] | Phase | Sig. (SLF) | Sig. (Avg.) | Remarks |
|---|---|---|---|---|---|---|
| 2 | 0.81054(94) | 11.40(41) | 0.814(36) | 11.92 | 11.98 | $f_{\mathrm{rot,BLC}}$ |
| 1 | 1.64551(61) | 17.45(41) | 0.621(24) | 20.86 | 19.45 | $2f_{\mathrm{rot,BLC}}$ |
| 11 | 2.4626(47) | 2.26(42) | 0.10(18) | 5.47 | 5.75 | $3f_{\mathrm{rot,BLC}}$ |
| 12 | 3.2942(48) | 2.22(42) | 0.92(19) | 14.11 | 12.3 | $4f_{\mathrm{rot,BLC}}$ |
| 15 | 4.108(29) | 0.36(42) | 0.32(17) | 4.04 | 2.77 | $5f_{\mathrm{rot,BLC}}$ |
| 13 | 4.940(16) | 0.64(42) | 0.86(66) | 9.12 | 8.02 | $6f_{\mathrm{rot,BLC}}$ |
| 14 | 5.764(24) | 0.44(42) | 0.25(95) | 6.99 | 6.2 | $7f_{\mathrm{rot,BLC}}$ |
| 17 | 7.398(54) | 0.20(42) | 0.45(12) | 3.31 | 4.27 | $8f_{\mathrm{rot,BLC}}$ |
| 5 | 0.0505(21) | 5.06(42) | 0.572(83) | 5.26 | 5.19 | $f_{\mathrm{orb}}$? |
| 4 | 0.1407(16) | 6.41(42) | 0.617(65) | 6.66 | 6.67 | $2f_{\mathrm{orb}}$? |
| 3 | 0.6329(17) | 6.05(42) | 0.066(69) | 6.29 | 7.09 | |
| 6 | 1.1048(24) | 4.43(42) | 0.174(95) | 4.68 | 4.47 | |
| 7 | 0.7128(24) | 4.35(42) | 0.951(97) | 4.52 | 4.92 | |
| 8 | 0.2861(27) | 3.92(42) | 0.80(10) | 4.08 | 4.61 | $4f_{\mathrm{orb}}$? |
| 9 | 0.3982(31) | 3.40(42) | 0.77(12) | 3.53 | 4.44 | |

Table 5.2: The significant frequencies of photometric variability identified in the SAP TESS data. The significance (Sig.) is shown assuming both a SLF noise model and a box average noise model. Two frequencies are only identified as significant in one of the two significance tests shown.

Seventeen frequencies were extracted from the SAP TESS data, fifteen of which were identified to be significant and are detailed in Table 5.1. The frequency content is broadly similar to that of the detrended data. The exception to this is the detection of a frequency at 0.0505(21) c/d. This frequency may be associated with the orbital modulation of the system, recalling that detrending of TESS data can affect the detection of signals . However, such an association is difficult to uphold as this frequency deviates from the orbital frequency by approximately $9\sigma$.

Twenty-two frequencies were extracted from the CoRoT data, fifteen of which were identified to be significant and are detailed in Table 5.1. The harmonic structure about the BLC rotational frequency was observed to contain eight significant harmonics up to a maximum frequency of $10f_{\mathrm{rot,BLC}}$. A frequency at $9f_{\mathrm{rot,BLC}}$ was also detected and identified as insignificant. Variability at the orbital frequency of the system was clearly detected, contrary to both TESS analyses. A frequency near the fourth harmonic of the orbital

frequency is detected as well as an insignificant frequency near the first harmonic (see App. E). One frequency of unknown physical origin was detected at $f \approx 0.3653$ c/d, which does not clearly correspond with any frequencies detected in either of the TESS light curves.

| Index | Frequency [c/d] | Amplitude [mmag] | Phase | Sig. (SLF) | Sig. (Avg.) | Remarks |
|---|---|---|---|---|---|---|
| 2 | 0.81992(70) | 11.26(49) | 0.925(43) | 9.77 | 9.46 | $f_{\rm rot,BLC}$ |
| 1 | 1.64586(51) | 15.33(48) | 0.124(32) | 22.15 | 20.71 | $2f_{\rm rot,BLC}$ |
| 9 | 2.4663(25) | 3.11(49) | 0.72(15) | 12.14 | 12.04 | $3f_{\rm rot,BLC}$ |
| 11 | 3.2920(56) | 1.42(49) | 0.95(34) | 12.64 | 8.7 | $4f_{\rm rot,BLC}$ |
| 13 | 4.106(19) | 0.42(49) | 0.07(19) | 6.01 | 4.75 | $5f_{\rm rot,BLC}$ |
| 15 | 4.939(25) | 0.31(49) | 0.48(60) | 5.79 | 5.33 | $6f_{\rm rot,BLC}$ |
| 12 | 5.763(14) | 0.55(49) | 0.95(90) | 11.58 | 9.8 | $7f_{\rm rot,BLC}$ |
| 20 | 6.589(51) | 0.16(49) | 0.36(18) | 3.54 | 4.2 | $8f_{\rm rot,BLC}$ |
| 21 | 8.226(63) | 0.12(49) | 0.04(98) | 2.98 | 4.25 | $10f_{\rm rot,BLC}$ |
| 3 | 0.0699(12) | 6.54(49) | 0.356(75) | 5.46 | 5.48 | $f_{\rm orb}$ |
| 6 | 0.1467(21) | 3.64(49) | 0.32(13) | 3.04 | 2.88 | $2f_{\rm orb}$ |
| 7 | 0.3653(16) | 4.82(49) | 0.69(10) | 4.02 | 4.09 | |
| 14 | 3.309(14) | 0.54(49) | 0.18(92) | 4.84 | 3.32 | Assoc. $f_{11}$ |

Table 5.3: The significant frequencies of photometric variability identified in the CoRoT data. The significance (Sig.) is shown assuming both a SLF noise model and a box average model. Three frequencies are only identified as significant in one of the two significance tests shown, and an insignificant frequency measured near 0.14 c/d is also included as it is suspected to be associated with the orbital frequency.

## 5.2 Characterization of the SLF Noise

A least-squares fit of Eq. 4.24 was performed on the final residual light curve of each pre-whitening analysis to estimate a noise level such that the SNR of each frequency could be measured. Fits of Eq. 4.24 were performed on each residual periodogram to measure $\nu_{\rm char}$, $\alpha_0$, $\gamma$, and $C_w$, and the best-fit models are shown in Figs. 5.2, 5.3, and 5.4. The optimized parameters for each of these fits are presented in Table 5.4 with the standard least-squares fit errors. Notably, there appears to be a difference in shape between the SLF variability model of the CoRoT and the two TESS datasets. This isn't particularly sur-

prising as the instrument and data reduction processes will contribute noise and systematics to the spectrum. This introduces power to the spectrum and obscures the detection of real frequencies. The residual LS periodograms with the SLF noise fits for the detrended TESS data, the SAP TESS data, and the CoRoT are shown in Fig. 5.2, Fig. 5.3, and Fig. 5.4 respectively.

| Dataset | $\nu_{\mathrm{char}}$ [c/d] | $\alpha_0$ [mmag] | $\gamma$ | $C_w$ [mmag] |
|---|---|---|---|---|
| TESS Detrended | 2.42414(15) | 0.883(14) | 5.476(13) | 0.02(11) |
| TESS SAP | 2.38193(16) | 0.955(16) | 4.6781(78) | 0.01(23) |
| CoRoT | 1.77(17) | 1.207(46) | 3.65932(59) | 0.01(51) |

Table 5.4: The best fit parameters for the fit of the Bowman et al. (2019b) SLF noise model to the residual light curve from the detrended TESS, SAP TESS, and CoRoT analyses.

Bowman et al. (2020) measured SLF models from TESS data of O and B-type stars spanning from dwarves to supergiants. For their sample of O-type giant stars, they measured mean values for $\alpha_0$ and $\nu_{\mathrm{char}}$ of approximately 0.564 mmag and 2.50 c/d with standard deviations of 0.313 mmag and 0.84 c/d respectively. For their sample of O-type bright giant and supergiant stars, the mean values were instead 2.99 mmag and 1.37 c/d with standard deviations of 1.47 mmag and 0.55 c/d respectively. The measurements from the TESS data presented in Table 5.4 are most consistent with the giant sample, however they do appear skewed towards the more extreme values of the bright giants/supergiants. This agrees with the luminosity classes of I/III and III reported for the NLC and BLC respectively by Linder et al. (2008). Considering the (dimensionless) $\gamma$ parameter, the mean values reported by Bowman et al. (2020) for the O giants and O bright giants/supergiants were approximately 1.82 and 2.97 with standard deviations of 0.38 and 1.10 respectively. The measurements of $\gamma$ from the TESS photometry which are presented in Table 5.4 are therefore higher than would be expected from the O giants sample, and are generally above average for the O bright giants/supergiants sample. From Eq. 4.24, an increase in $\gamma$ will cause the red noise component to decrease in amplitude more quickly with increasing frequency. This is reflected in the residual periodograms (see Figs. 5.2 and 5.3) and these models appear to fit the residual frequency spectra reasonably well.

### 5.2.1 Variability due to Rossby Modes

The two primary oscillation modes in pulsating stars are the gravity modes (g-modes, thought to be the source of SLF variability in massive stars), with buoyancy as the restoring force, and pressure modes (p-modes), with gas pressure as the restoring force (Aerts et al., 2010). For rotating stars, however, there is an additional oscillatory mode of particular relevance. The equations for non-radial pulsation modes of non-rotating stars yield "trivial" solutions with frequencies of zero. However, due to the introduction of the Coriolis force, the solutions for rotating stars have non-zero frequencies and these solutions are referred to as Rossby modes (r-modes; Papaloizou and Pringle, 1978; Saio, 1982). These have proven challenging to observe directly (Robinson et al., 1982; Kepler, 1984), however have been recently observed in the sun (Sturrock and Bertello, 2010; Sturrock et al., 2015) and $\gamma$ Dor stars (Van Reeth et al., 2016). Saio et al. (2018) argued that r-mode oscillations should be present in B, A, and F-type main sequence binary star systems (in addition to those with spotted stars or g-mode pulsators). In frequency space, r-modes manifest as a group of frequencies just below the rotation frequency of the star (see Fig. 5.8). This leads to the hypothesis that the g-modes of the SLF variability in the light curves of Plaskett's Star are blended with r-modes. The additional power added to the $f < 0.82$ c/d region of the periodogram would naturally lead to an apparent steeper decline in the red noise model with increasing frequency, thereby naturally accounting for the higher observed $\gamma$ values for Plaskett's Star compared to the giant and bright giant/supergiant samples of Bowman et al. (2020).

A more sophisticated asteroseismological analysis, likely focusing on the period spacings and numerical modelling, is required to confirm or reject the presence of r-modes in the photometry of Plaskett's Star. Nonetheless, if this hypothesis can be substantiated then Plaskett's Star would constitute the first O-type star in which r-modes have been directly observed (Saio, private comm.). As both current revised models for Plaskett's Star interpret the BLC as a rapidly-rotating but otherwise ordinary magnetic O-type star, they are both compatible with the presence of r-mode pulsation.
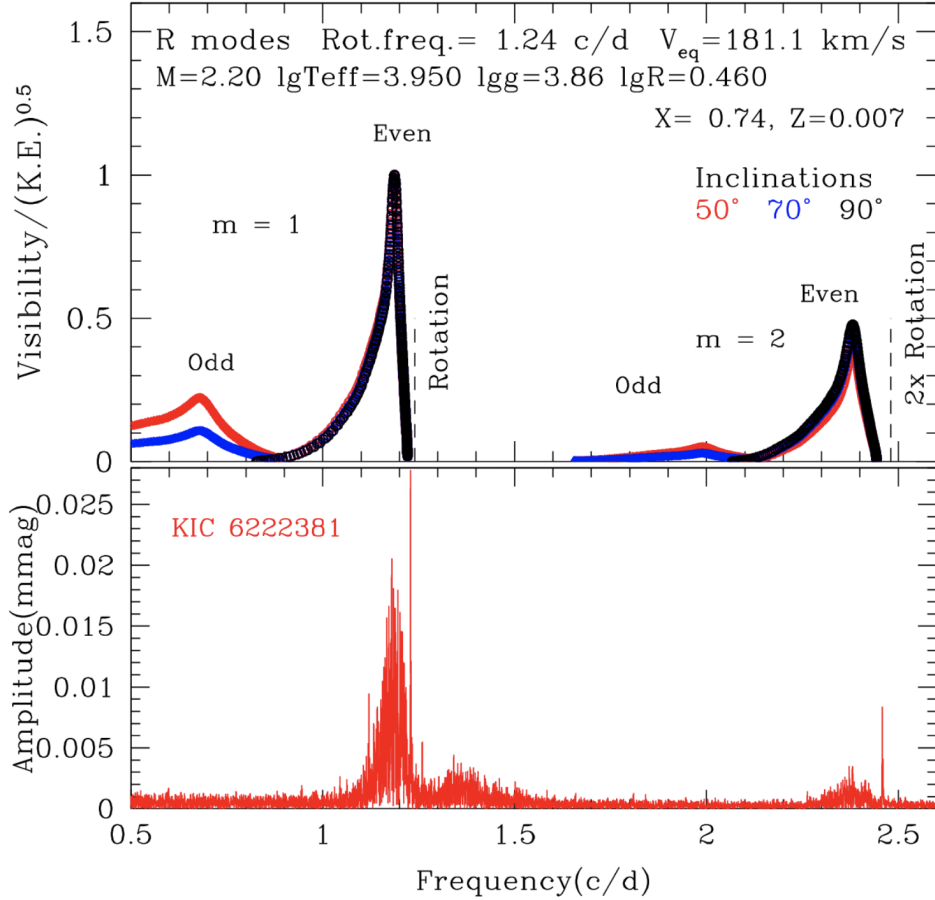
Figure 5.8: (Top) The ratio of visibility, defined as the disc-integrated amplitude of the pressure and temperature perturbations, to the kinetic energy of the r-modes numerically estimated at three inclinations for a 2.2 $M_\odot$ model star with a rotation frequency of 1.24 c/d. (Bottom) The amplitude spectrum of photometry collected by the Kepler space telescope for the A-type star KIC 6222381. This figure was presented by Saio et al. (2018) to argue that KIC 6222381 demonstrates r-modes.

# 6 Interpretation of the Observed Frequencies

The dominant frequencies present in all three datasets were detected at the fundamental frequency and the first harmonic frequency corresponding to the rotation of the BLC. Particularly, this first harmonic is the strongest frequency observed in both the TESS and CoRoT data. This is a consequence of the centrifugal magnetosphere hosted by the BLC that was reported by Grunhut et al. (2022). The magnetospheric structure is modelled to qualitatively consist of two corotating hot, dense regions of centrifugally supported and magnetically confined plasma, which each partially eclipse the star once per rotation. According to formal uncertainties, the measurements corresponding to the rotational frequency between the CoRoT and detrended TESS data differ by approximately $9.5\sigma$[1]. This could be interpreted as a change in the rotational frequency of the BLC over the 10 years separating the datasets. However, this would imply the rotation rate of the BLC has *increased* over the last 10 years and such a change is challenging to explain. Additionally, such a disagreement is not reflected in measurements at the first harmonic of the BLC rotational frequency, where the results of the detrended TESS and CoRoT data agree well within $1\sigma$. This difference could instead be attributable to blending of this peak with a noise peak, which would naturally explain the differences in fundamental frequencies and the agreement of the first harmonic frequencies.

Variability at the orbital period is clearly detected in the CoRoT data. The TESS data, spanning only around 21 days, unsurprisingly didn't yield a clear detection at the orbital period. A nominally plausible candidate for orbital variability is $f_5$ in the results of the SAP data analysis, with a frequency

---

[1]The difference is reduced to approximately $5.7\sigma$ if the SAP TESS data is considered instead of the detrended TESS data.

of 0.0505(21) c/d. However no analogue exists in the self-consistent analysis of the detrended data and this frequency differs from the Linder et al. (2008) orbital frequency by approximately $9\sigma$, according to formal uncertainties. A frequency analysis of the detrended data which extracts 15 frequencies by highest amplitude (with no peak selection significance criterion), as opposed to 10, revealed a frequency at 0.08573(13) c/d with an amplitude of 2.72(34) mmag and significances of 4.19/4.66 (SLF Fit and box average, respectively). Given the proximity of these frequencies with respect to the $1.5/\Delta T$ resolution, their mutual exclusivity between the SAP and detrended data, and the known issues associated with low frequencies in TESS detrending, these two measurements are potentially related. However, it is clear that these two measurements aren't reliable regardless of whether they're associated with the orbital frequency or not.

Both the detrended and SAP TESS data demonstrated variability near 0.14 c/d that is consistent within $1\sigma$ and $2\sigma$, respectively, with the first harmonic of the Linder et al. (2008) orbital frequency. Despite the issues with reliable detection of the fundamental orbital frequency, it isn't entirely surprising given that frequencies higher than approximately 0.01 c/d were observed over a minimum of two cycles. An analogous frequency was also detected in the CoRoT data ($f_6$ of Table E.3), however this frequency was not consistent within formal uncertainties of the first harmonic of the orbital frequency, nor was it deemed to be statistically significant. It is important to note that the analysis of Mahy et al. (2011) identifies a frequency with a similar amplitude that *does* agree with the first harmonic of the orbital frequency, and they also identified variability at several additional nearby frequencies (e.g. 0.112 c/d, 0.158 c/d). The measurements of variability near 0.14 c/d differ in amplitude between the TESS and CoRoT data. The amplitude from the detrended TESS data is approximately 59% greater than the amplitude from the CoRoT data. This could be attributable to differences in bandpasses between the two instruments, particularly given the relatively large fractional uncertainties at these amplitudes.

## 6.1 Orbital Photometric and Radial Velocity Modulation

Measurements of the radial velocity were provided by Linder et al. (2008). No formal uncertainties were given for the Linder et al. (2008) radial veloc-

ities. Those authors remarked that the dispersion was less than 2.0 km/s and 20.0 km/s for the NLC and BLC measurements respectively; these values were adopted as nominal uncertainties for this analysis. Additionally, Linder et al. (2008) reported systemic velocities of $30.6 \pm 1.8$ for the NLC and $-6.0 \pm 9.6$ for the BLC. The data were corrected for their respective systemic velocities and the uncertainties on systemic velocities were propagated to the measurements. The difference in systemic velocities is substantial, however not necessarily surprising given what is now known about the radial velocity of the BLC.

Radial velocities measured from disentangled ESPaDOnS spectra were also kindly provided by Dr. Oleg Kochukhov[2]. The disentangling method used for these spectra was that of Folsom et al. (2010), assuming zero eccentricity and the Linder et al. (2008) orbital frequency. The radial velocities were measured from He II lines at 420.0 nm, 454.2 nm, and 541.1 nm as well as the He I line at 402.6 nm. A single measurement was determined for each spectrum by averaging the measurements across the four lines, and the uncertainty was taken as the standard deviation of the four measurements.

The radial velocity measurements are plotted in Fig. 6.1 and the full set of measurements and timestamps are tabulated in App. F. In light of the evidence for near-zero BLC radial velocities presented by Grunhut et al. (2022) (and reflected in the Kochukhov measurements), only the radial velocity measurements for the NLC were considered.

The orbital period measurement of Linder et al. (2008) was first verified given the new data by phase-folding the NLC radial velocities at 1000 sample periods linearly distributed between 14.2 and 14.6 and performing $\chi^2$ optimizations of sinusoidal models. At each sample period, the amplitude and phase were optimized and the reduced $\chi^2$ was measured. The sample period producing the minimal $\chi^2$ fit was 14.39639 d, which was within $1\sigma$ of the $14.39626 \pm 0.00095$ d measurement reported by Linder et al. (2008).

Directly comparing the photometric variability and radial velocity models is challenging, as the period measured in CoRoT photometry ($P_{\mathrm{orb}} = 14.31 \pm 0.25$) is poorly constrained compared to the period measured in radial velocity. This difference in period means the relative phases will become increasingly meaningless as they're extrapolated farther from the the reference

---

[2]Department of Physics and Astronomy, Uppsala University, Sweden.
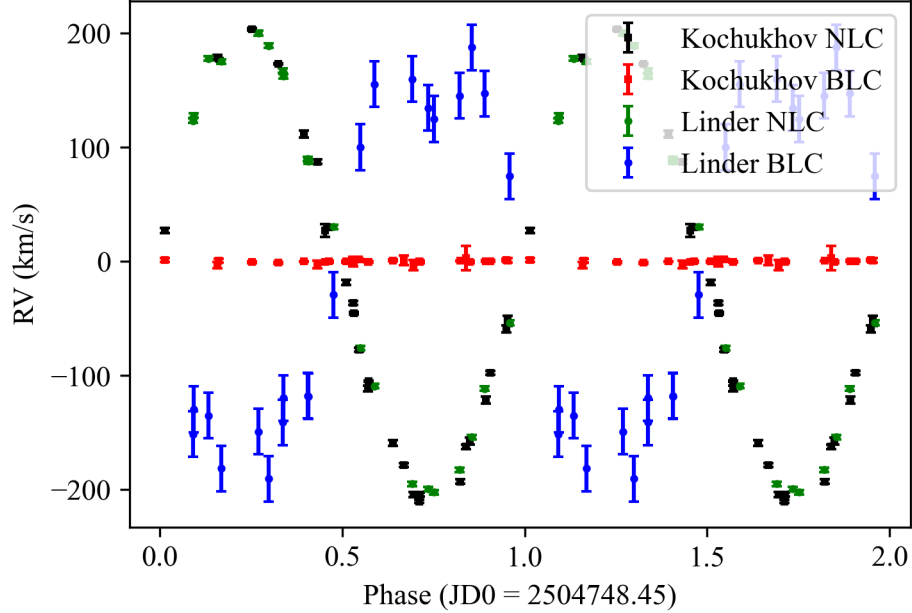
Figure 6.1: The radial velocity measurements from the Linder et al. (2008) analysis and the ESPaDOnS spectra phased according to the Linder et al. (2008) orbital period. For clarity, the data has been duplicated and plotted from phases of 1 to 2 as well.

time(s) of the original measurements. To mitigate this, the phase measurements were both made with respect to the midpoint of the CoRoT timeseries at $JD_0 = 2454765.63$. It was assumed the variability phase inferred through this measurement was independent of the measurement of orbital frequency at this timestamp. Normalized models of the photometric variability at the orbital period and its first harmonic were generated using the orbital period measured from the radial velocities and the amplitudes/phases measured from the CoRoT photometry. These models were generated over a single orbital period starting on JD 2454765.63 alongside an interpolated model of the radial velocity variability. The input parameters are tabulated in Table 6.1 and the resultant models are plotted in Fig. 6.2.

Variability at the orbital frequency probes reflective effects and Doppler boosting. The phases are 0.856(76) and 0.921 for the photometric and radial
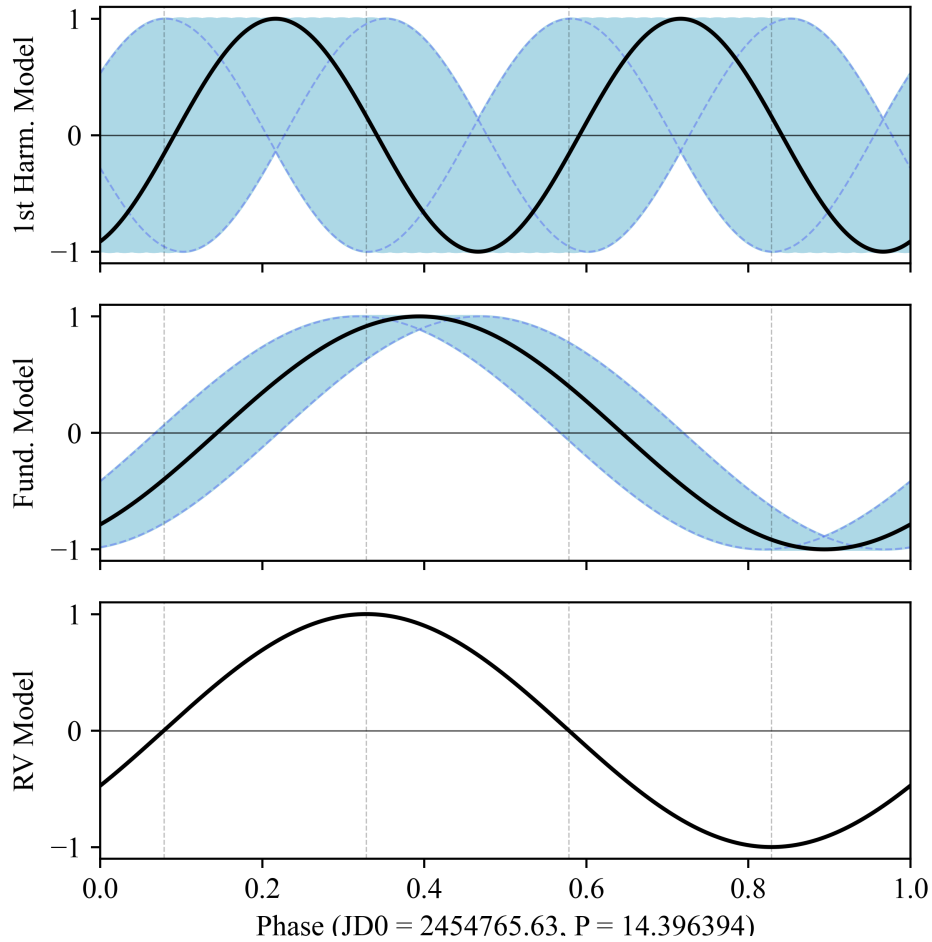
Figure 6.2: Top: A photometric variability model computed at twice the orbital frequency measured from radial velocities and the phase associated with $f_6$ measured from the CoRoT photometry (which was interpreted as the first harmonic of the orbital frequency). Middle: A photometric variability model computed using the orbital frequency measured from radial velocities and the phase measured from the CoRoT photometry. Bottom: The radial velocity model for the NLC. Vertical dashed lines indicate quarter-waves of the radial velocity model, and each panel has a horizontal flat line indicating zero. The dashed blue lines and blue region indicate the $1\sigma$ bounds according to the errors on phase determined by the pre-whitening algorithm.

| Model | $f$ [c/d] | $\phi$ |
|---|---|---|
| Photometric Variability, Orb. Frequency | 0.069462 | 0.856 |
| Photometric Variability, 1st Harm. Orb. Frequency | 0.138924 | 0.817 |
| Radial Velocity Variability | 0.069462 | 0.921 |

Table 6.1: The parameters used to generate models to compare the relative phasing of the radial velocity variability and photometric variability at the orbital period.

velocity models, respectively. Doppler boosting is implied if the phase difference between the two is zero, and reflection is implied if the phase difference is a quarter wave (0.25, in this case). The phase difference is consistent within $1\sigma$ of that indicating Doppler boosting of the BLC, within approximately $2.5\sigma$ of that indicating reflection off the NLC, and within approximately $4.15\sigma$ of that indicating reflection off the BLC. Doppler boosting of the BLC is difficult to reconcile with the near-zero radial velocities of the BLC, however. Additionally, reflection is challenging to reconcile with the similar surface temperatures between the NLC and BLC. Assuming the hypothesized case of a BH+O X-ray binary, surface heating of the NLC may be permitted through the X-ray flux, in which case the temperature increase would lead to enhancements in its optical luminosity (and optical photometric variability as the heated side passes in and out of view).

Photometric variability at the first harmonic of the orbital frequency is reflective of ellipsoidal variability if the maxima in radial velocity correspond to absolute photometric maxima. From Fig. 6.2, it is clear that the phase measurement in the CoRoT photometry was too imprecise to draw any definitive conclusions about whether ellipsoidal variability was observed. If ellipsodial variability were the dominant source of photometric modulation related to the system orbit, that would be reflected in the relative strengths of the orbital frequency and its first harmonic. From the CoRoT photometry, this doesn't appear to be the case. However, the presence of reasonably strong variability at the first harmonic of the orbital frequency in both the TESS and CoRoT photometry, given the absence of a competing explanation, is suggestive there is some degree of ellipsoidal variability present even if its presence cannot be confirmed through phase measurements. An important consequence of the presence of ellipsoidal variability is that the same structural distortion that is responsible for the photometric variability is also that which leads to synchronization and circularization. This is further discussed in Sect. 6.2.1.

## 6.2   Frequencies of Unknown Physical Origin

The TESS data reveals five frequencies of unknown physical origin at 0.2855(13), 0.3910(14), 0.63516(84), 0.7132(10), and 1.1042(11) c/d. None of these frequencies are detected significantly in the CoRoT data, however variability at approximately 0.3957(21) and 0.6494(21) c/d was detected insignificantly. These two frequencies are analogous to the 0.3910(14) c/d and 0.63516(84) c/d frequencies observed in the TESS data. The variability at 0.3910 c/d and 0.63516 c/d in the TESS data likely originate from Plaskett's Star and appear to exhibit stability on the order of 10 years. Variability at 0.3653(16) c/d was measured in the CoRoT data, with no analogue in the TESS data. This is possibly the fifth harmonic of the orbital frequency, however this is unlikely given its moderate amplitude and the lack of a a complete set of intermediate harmonics.

The following discussion focuses on rotation of the NLC, as rotational modulation of the NLC is expected to be a potential source of photometric variability in the system and the rotational period of the NLC is presently unknown. However, variability at any or all of the unknown frequencies may also be the result of stellar pulsation. Stellar pulsation due to g-mode oscillations is generally regarded as responsible for the SLF variability discussed elsewhere in this work, however there are numerous stellar classes which demonstrate regular, periodic variability due to stellar pulsation (e.g. cepheids, slowly pulsating B-type/SPB stars Moffat, 2012). However, oscillation mode identification is both challenging and beyond the scope of this work as it typically relies on analysis of line profile variability in high-resolution spectroscopic observations.

### 6.2.1   Rotation Frequency of the NLC

While the rotation frequency of the BLC determined through magnetospheric modulation is reflected in the photometry, the rotation frequency of the NLC is unknown. This may provide an explanation for the photometric variability of unknown physical origin. However, photometric variability at the rotational frequency of the NLC is only expected if there are inhomogeneities on the stellar surface (e.g. chemical spots) that cause the star to modulate in brightness as it rotates. Additionally, the rotation period may be sufficiently long that rotational modulation is not measurable. Nevertheless, an upper limit to the rotational frequency can be determined by investigating its critical rotation.

The critical rotation period is the rotational period at which the centripetal force and gravitational force at the surface of the star are equivalent. If the NLC were to have a rotational period shorter than the critical rotation period, the centripetal force necessary to keep surface material bound would be higher than the gravitational force and it would be torn apart by centrifugal force. The gravitational force at the surface of a uniform-density star of radius $R$ and mass $M$ on a point particle of mass $m$ is

$$F_G = \frac{GMm}{R^2}. \tag{6.1}$$

The centripetal force required to keep a point particle of mass $m$ bound to a orbit at a radius $R$ with a period of $f$ is

$$F_C = m(2\pi f)^2 R. \tag{6.2}$$

Combining Eqs. 6.1 and 6.2 and imposing the condition that the force of gravity must always exceed the centripetal force yields

$$\frac{GM}{4\pi^2 R^3} \geq f^2. \tag{6.3}$$

To determine the quantity on the left-hand side of Eq. 6.3, both the mass of the object and its radius must be specified. The current proposed models for the structure of the system imply two possible mass-radius pairs, both of which were considered.

For the BH+O binary model, the NLC was assumed to be consistent with the historical model. Linder et al. (2008) reported, assuming the historical model, a mass of $M_{\mathrm{NLC}} \sin^3 i = (45.4 \pm 2.4)$ M$_\odot$ for the NLC. Martins et al. (2005) reported nominal stellar radii of 13.74 R$_\odot$ and 21.10 R$_\odot$ for stars spectral types O8III and O8I respectively. From the Stefan-Boltzmann law (see Eq. 1.1), the ratios of luminosity $L$, radius $R$, and surface temperature $T$ between a target of interest and a reference target (denoted by a subscript $s$) are related by

$$\frac{L}{L_s} = \left(\frac{R}{R_s}\right)^2 \left(\frac{T}{T_s}\right)^4. \tag{6.4}$$

Using the sun as a reference target and the NLC luminosity and temperature reported by Linder et al. (2008) with Eq. 6.4, a radius of 14.08 R$_\odot$ is implied. This is consistent with the nominal stellar radius for an O8III star as per Martins et al. (2005). In this case, the critical rotation frequency of the NLC is approximately 1.38 c/d at an inclination of 90°. Instead considering

the nominal radius for an O8I star, the critical rotation frequency is 0.84 c/d. If an inclination of approximately 70° is instead adopted (Stickland, 1987), these figures are 1.47 and 0.92 c/d.

For the sdO+O binary model, Götberg et al. (2018) reported a wide range of masses and associated radii for potential sdO companions. The surface temperature measured by Linder et al. (2008) of $33.5 \pm 2$ kK constrains the potential sdO masses to approximated 2.7 to 3.3 $M_\odot$, with associated radii from 0.29 to 0.39 $R_\odot$. Assuming a mass of 3 $M_\odot$ and a radius of 0.35 $R_\odot$ for a sdO NLC yields a critical rotation frequency of 13.04 c/d.

The rotational frequency can be inferred through the rotational broadening of the spectral lines. This is sensitive to both a reasonable understanding of the inclination of the system, through the measurement of $v \sin i$, and non-rotational sources of broadening (e.g. thermal, macroturbulent). Nevertheless, assuming a radius of 14.08 $R_\odot$, a typical projected rotational velocity of 65 km/s (Linder et al., 2008), and the Stickland (1987) inclination of 70°, the implied rotation period is approximately 10.3 days. This corresponds to a frequency of 0.097 c/d, and assumes the rotational axis is aligned with the orbital axis.

It is also pertinent to discuss the case where the NLC rotational frequency is synchronous with the orbital frequency. This is plausibly supported by the projected rotational velocity, given that a period of 10.3 days was estimated with relatively poor constraints on inclination and $v \sin i$. Through inhomogeneities on the stellar surface, this can lead to photometric variability at the orbital period at phases that is completely unrelated to the orbital phase. As discussed in Sect. 1.1.6, synchronization for evolved stars is relatively poorly studied. Therefore, discussion of synchronization in Plaskett's Star would be speculative. The timescales associated with orbital circularization are longer than those associated with synchronization according to Zahn (1977). Given that Plaskett's Star has a roughly circular orbit, this suggests that if the orbit of Plaskett's Star was once eccentric, it likely underwent synchronization.

The detection of variability at the first harmonic of the orbital period in the CoRoT photometry has implications for the discussion of synchronization in Plaskett's Star. This variability could be attributable to tidal ellipsoidal distortion, which would also suggest the effects of tidal synchronization and circularization to be strong. Alternatively, this variability could arise due to inhomogeneities on the surface of the NLC if it is rotationally synchronized

with its orbit, in which case it would also be expected to produce photometric variability at the orbital frequency as well as its harmonics. Therefore, the presence of variability at twice the orbital frequency is highly suggestive that the NLC is either synchronized, or is undergoing tidal distortion which will quickly act to quickly synchronize its rotation. In the context of the O+BH model, this behaviour is reasonably consistent with the expected evolutionary history of the system. For the sdO+O model, it's a bit more complex to assess the consequences of this result. Particularly, the BLC is evidently not synchronized and therefore the NLC must have either synchronized much more quickly than the BLC following the RLOF or preserved a synchronized rotation rate through the RLOF. The former case makes sense in the context of an evolution through a "bloated stage" as modelled by El-Badry and Quataert (2021) and Bodensteiner et al. (2020) for HR 6819 as tidal effects would be strong on the diffuse bloated star. However, interpreting the NLC as such an analogous object (to address the inconsistent measurements of $\log g$) would require that both sufficient time has passed since the RLOF that the object could be synchronized, however that it has not sufficiently collapsed to spin up the star with its shrinking moment of inertia.

The rotation of the NLC is compatible with all observed frequencies with unknown physical origin based on the critical rotation frequencies calculated for the NLC in both the BH+O and sdO+O binary models. The rotation of the NLC may also be synchronized with the system orbit, which is supported by the presence of photometric variability at the first harmonic of the orbital frequency. It is, however, difficult to confirm the NLC rotational frequency to be equivalent to any of these observed frequencies. Additionally, there exist no apparant *harmonic structures* of unknown physical origin, which is typical of rotational modulation for stars with chemical spots (private comm., Labadie-Bartz). In the case of the BLC, its rotational period was determined through spectropolarimetric observations of its longitudinal magnetic field modulation. In the case of the seemingly non-magnetic NLC, it's likely that determining its rotational period would require the spectroscopic observation of variability in chemical abundance (due to chemical spots) or line strengths (due to hot spots). This is highly nontrivial due to the disentangling necessary to focus specifically on the NLC.

# 7 Summary and Conclusions

## 7.1 Summary

Frequency analyses have been performed on two high-precision, high-cadence photometric datasets for HD 47129 collected by the TESS and CoRoT missions. To do so, a new Python-based iterative frequency analysis tool called PyPW was developed based on the common signal analysis technique of pre-whitening. This program identified a sinusoidal model for the photometric variability at a single frequency in each iteration. Over several iterations, this permitted the program to progressively construct a comprehensive model for the observed photometric variability as the sum of several sinusoids at different frequencies. PyPW focused on the simultaneous optimization of the commplete variability model at each iteration. Particularly, this program addressed the challenging problem of optimizing all three parameters of each individual sinusoid (frequency, amplitude, and phase) in the complete variability model. This functionality was verified against the well-established Period04 frequency analysis tool, and it was found that both tools produced near-identical results well within formal uncertainties in a fixed 10-frequency pre-whitening. It was found that attempting such an optimization of a variability model containing frequencies which are analytically indistinguishable based on the Loumos and Deeming (1978) resolution criterion led to clearly unphysical results. Additionally, it was found that the choice of when to terminate the iterative analysis and assume the residual light curve to consitute noise has a significant affect on the formal confidence in the results (e.g. significances and uncertainties). Both these issues were addressed by a more sophisticated algorithm for the initial selection of frequencies for the single-frequency models, which enforced the Loumos and Deeming (1978) frequency resolution criterion and a pseudo-noise level approximating SLF noise as described in Bowman et al. (2019a). PyPW, while designed for use with Plaskett's Star in this work, is nevertheless a robust and highly configurable program which is suitable for the analysis of space photometry for other systems demonstrating complex photometric

variability, particularly those demonstrating photometric evidence of binary interaction, multi-mode pulsation, and stochastic low-frequency variability.

SLF variability was observed to be the dominant source of low-frequency noise in both datasets. The SLF model for Plaskett's Star was found to demonstrate an unusually high $\gamma$ parameter when described using the Bowman et al. (2019b) model and compared against the O-type giant and O-type bright giant/supergiant samples of Bowman et al. (2020). The other parameters were found to be consistent with the O-type giant sample of Bowman et al. (2020), trending towards the more extreme values of the O bright giant/supergiant sample. The results of this comparison motivated the hypothesis that there is a contribution from Rossby modes in the rapidly-rotating BLC to the low-frequency power in the residual periodograms. However, confirmation or refutation of this hypothesis was beyond the scope of this work.

Self-consistent analyses were performed on the CoRoT photometry as well as the TESS photometry at two stages of data reduction (pre- and post-detrending). Both analyses of the TESS data were qualititatively consistent however demonstrated small quantitative differences. Strong variability was observed at the rotational frequency of the BLC and harmonics, including a strong first harmonic consistent with the presence of a centrifugal magnetosphere hosted by this star. Strong variability was also observed with frequencies of approximately 0.139 c/d, 0.286 c/d, 0.391 c/d, 0.635 c/d, 0.713 c/d, and 1.104 c/d. The former two frequencies were considered as potentially associated with the orbital motion of the system, however these data were not suitable for reliably studying variability associated with the orbital frequency of the system. It was also determined that the latter four frequencies were compatible with rotation of the NLC under both working hypotheses for the revised structure of the system, with the exception of the variability at 1.104 c/d in the case of a black hole companion. Most frequencies identified in the TESS photometry were consistent with those identified in the CoRoT photometry, noting that some analogous frequencies were detected insignificantly according to the procedure detailed in Sect. 4.3.4.

Variability at the orbital frequency of the system was reliably detected in the CoRoT photometry, however this was not apparent in the TESS data due to its short time baseline. Variability was detected at the first harmonic of the orbital frequency in the TESS data, and a seemingly analogous frequency was also detected insignificantly in the CoRoT data. Variability at the orbital frequency and its harmonic were compared with orbital phases inferred

from disentangled spectra in the interest of determining the physical source of variability at the orbital frequency. All of reflection, ellipsoidal distortion, and Doppler boosting (of the NLC) were found to be compatible with the phasing of the observed photometric variability. Large uncertainties in phase prevented the confident attribution of ellipsoidal distortion as the source of photometric variability at the first harmonic of the orbital frequency. Nevertheless, variability at this frequency was found to either likely arise through ellipsoidal distortion of the NLC or rotational modulation of the NLC due to surface inhomogeneities in the case that its rotation is synchronized with its orbit. Both these scenarios were found to be suggestive of synchronous rotation in the NLC, which is plausible given the 10.4 day rotational period inferred from the poorly constrained projected rotational velocity and inclination. This was found to be of little consequence for the BH+O hypothesis, however was found to support the interpretation of the subdwarf star in the sdO+O model as a bloated sdO star.

In the context of the two new hypothesized models for the system based on the results of Grunhut et al. (2022), no evidence is found particularly favouring one model over the other; the observed photometric variability is consistent with the case that the NLC is a sdO-type star as well as the case where the NLC is in a mutual orbit with an unseen companion. Nevertheless, these results serve to inform future investigations into the structure of Plaskett's Star.

## 7.2 Future Work

The approach to determining the physical cause of variability at the orbital period in this work is rudimentary. That is, the variability was assumed to implicity arise from a single physical source. In reality, there's nothing preventing these phenomena from occuring simultaneously, yielding complex variability that's challenging to interpret through a pre-whitening analysis alone. Therefore, the immediate priority to build upon this work is to perform computer simulations of candidate binary configurations to attempt to reproduce the observed photometric variability thought to be related to the orbital motion of the system. Work has already begun on this using the PHysics Of Eclipsing BinariEs (PHOEBE) package, which is a general, robust, open-source python package for simulating binary systems and their observables (Prša and Zwitter, 2005; Prša et al., 2016; Horvat et al., 2018; Jones et al., 2020; Conroy et al., 2020).

94

The photometric variability due to the rotation of the BLC, which is a result of its centrifugal magnetosphere, cannot be modelled through PHOEBE. Berry et al. (submitted) developed a program for modelling the photometric variability of magnetic massive stars hosting centrifugal magnetospheres. While the analysis of Berry et al. (submitted) focuses on B-type stars, this program is likely also suitable for application with Plaskett's Star. Therefore, this code will be used to model the photometric variability of the BLC of Plaskett's Star in the interest of performing an independent measurement of its magnetic and rotational properties.

For the broader project surrounding Plaskett's Star, it's clear that developing a comprehensive revised understanding of this system will be no trivial task. Ultimately, it's likely that an understanding of Plaskett's Star with equivalent completeness to the historical model will rely on constraints from multiple observing techniques (e.g. spectroscopy, photometry, interferometry) across multiple electromagnetic regimes. In conclusion, Plaskett's Star is a fascinating system with a unique history, and the results of future work on this system are highly anticipated.

# Bibliography

Abt, H. A. and Snowden, M. S., "The Binary Frequency for AP Stars", *The Astrophysical Journal Supplement Series*, 1973, 25, 137.

Aerts, C., Christensen-Dalsgaard, J., and Kurtz, D. W., *Asteroseismology*, Astronomy and Astrophysics Library, Springer, Dordrecht ; New York, 2010.

Aldoretta, E. J., Caballero-Nieves, S. M., Gies, D. R., Nelan, E. P., Wallace, D. J., Hartkopf, W. I., Henry, T. J., Jao, W. C., Maíz Apellániz, J., Mason, B. D., Moffat, A. F. J., Norris, R. P., Richardson, N. D., and Williams, S. J., "The Multiplicity of Massive Stars: A High Angular Resolution Survey With the Guidance Sensor", *The Astronomical Journal*, 2015, 149, 26.

Alecian, E., Wade, G. A., Catala, C., Grunhut, J. H., Landstreet, J. D., Bagnulo, S., Böhm, T., Folsom, C. P., Marsden, S., and Waite, I., "A high-resolution spectropolarimetric survey of Herbig Ae/Be stars - I. Observations and measurements", *Monthly Notices of the Royal Astronomical Society*, 2013, 429, 1001.

Antoci, V., Cunha, M. S., Bowman, D. M., Murphy, S. J., Kurtz, D. W., Bedding, T. R., Borre, C. C., Christophe, S., Daszyńska-Daszkiewicz, J., Fox-Machado, L., García Hernández, A., Ghasemi, H., Handberg, R., Hansen, H., Hasanzadeh, A., Houdek, G., Johnston, C., Justesen, A. B., Kahraman Alicavus, F., Kotysz, K., Latham, D., Matthews, J. M., Mønster, J., Niemczura, E., Paunzen, E., Sánchez Arias, J. P., Pigulski, A., Pepper, J., Richey-Yowell, T., Safari, H., Seager, S., Smalley, B., Shutt, T., Sódor, A., Suárez, J. C., Tkachenko, A., Wu, T., Zwintz, K., Barceló Forteza, S., Brunsden, E., Bognár, Z., Buzasi, D. L., Chowdhury, S., De Cat, P., Evans, J. A., Guo, Z., Guzik, J. A., Jevtic, N., Lampens, P., Lares Martiz, M., Lovekin, C., Li, G., Mirouh, G. M., Mkrtichian, D., Monteiro, M. J. P. F. G., Nemec, J. M., Ouazzani, R. M., Pascual-Granado, J., Reese, D. R., Rieutord, M., Rodon, J. R., Skarka, M., Sowicka, P., Stateva, I., Szabó, R.,

and Weiss, W. W., "The first view of $\delta$ Scuti and $\gamma$ Doradus stars with the TESS mission", *Monthly Notices of the Royal Astronomical Society*, 2019, 490, 4040.

Astropy Collaboration, Price-Whelan, A. M., Lim, P. L., Earl, N., Starkman, N., Bradley, L., Shupe, D. L., Patil, A. A., Corrales, L., Brasseur, C. E., Nöthe, M., Donath, A., Tollerud, E., Morris, B. M., Ginsburg, A., Vaher, E., Weaver, B. A., Tocknell, J., Jamieson, W., van Kerkwijk, M. H., Robitaille, T. P., Merry, B., Bachetti, M., Günther, H. M., Aldcroft, T. L., Alvarado-Montes, J. A., Archibald, A. M., Bódi, A., Bapat, S., Barentsen, G., Bazán, J., Biswas, M., Boquien, M., Burke, D. J., Cara, D., Cara, M., Conroy, K. E., Conseil, S., Craig, M. W., Cross, R. M., Cruz, K. L., D'Eugenio, F., Dencheva, N., Devillepoix, H. A. R., Dietrich, J. P., Eigenbrot, A. D., Erben, T., Ferreira, L., Foreman-Mackey, D., Fox, R., Freij, N., Garg, S., Geda, R., Glattly, L., Gondhalekar, Y., Gordon, K. D., Grant, D., Greenfield, P., Groener, A. M., Guest, S., Gurovich, S., Handberg, R., Hart, A., Hatfield-Dodds, Z., Homeier, D., Hosseinzadeh, G., Jenness, T., Jones, C. K., Joseph, P., Kalmbach, J. B., Karamehmetoglu, E., Kałuszyński, M., Kelley, M. S. P., Kern, N., Kerzendorf, W. E., Koch, E. W., Kulumani, S., Lee, A., Ly, C., Ma, Z., MacBride, C., Maljaars, J. M., Muna, D., Murphy, N. A., Norman, H., O'Steen, R., Oman, K. A., Pacifici, C., Pascual, S., Pascual-Granado, J., Patil, R. R., Perren, G. I., Pickering, T. E., Rastogi, T., Roulston, B. R., Ryan, D. F., Rykoff, E. S., Sabater, J., Sakurikar, P., Salgado, J., Sanghi, A., Saunders, N., Savchenko, V., Schwardt, L., Seifert-Eckert, M., Shih, A. Y., Jain, A. S., Shukla, G., Sick, J., Simpson, C., Singanamalla, S., Singer, L. P., Singhal, J., Sinha, M., Sipőcz, B. M., Spitler, L. R., Stansby, D., Streicher, O., Šumak, J., Swinbank, J. D., Taranu, D. S., Tewary, N., Tremblay, G. R., de Val-Borro, M., Van Kooten, S. J., Vasović, Z., Verma, S., de Miranda Cardoso, J. V., Williams, P. K. G., Wilson, T. J., Winkel, B., Wood-Vasey, W. M., Xue, R., Yoachim, P., Zhang, C., Zonca, A., and Astropy Project Contributors, "The Astropy Project: Sustaining and Growing a Community-oriented Open-source Project and the Latest Major Release (v5.0) of the Core Package", *The Astrophysical Journal*, 2022, 935, 167.

Aurière, M., Wade, G. A., Silvester, J., Lignières, F., Bagnulo, S., Bale, K., Dintrans, B., Donati, J. F., Folsom, C. P., Gruberbauer, M., Hui Bon Hoa, A., Jeffers, S., Johnson, N., Landstreet, J. D., Lèbre, A., Lueftinger, T., Marsden, S., Mouillet, D., Naseri, S., Paletou, F., Petit, P., Power, J., Rincon, F., Strasser, S., and Toqué, N., "Weak magnetic fields in Ap/Bp

stars: Evidence for a dipole field lower limit and a tentative interpretation of the magnetic dichotomy", *Astronomy & Astrophysics*, 2007, 475(3), 1053.

Auvergne, M., Bodin, P., Boisnard, L., Buey, J.-T., Chaintreuil, S., Epstein, G., Jouret, M., Lam-Trong, T., Levacher, P., Magnan, A., Perez, R., Plasson, P., Plesseria, J., Peter, G., Steller, M., Tiphène, D., Baglin, A., Agogué, P., Appourchaux, T., Barbet, D., Beaufort, T., Bellenger, R., Berlin, R., Bernardi, P., Blouin, D., Boumier, P., Bonneau, F., Briet, R., Butler, B., Cautain, R., Chiavassa, F., Costes, V., Cuvilho, J., Cunha-Parro, V., de Oliveira Fialho, F., Decaudin, M., Defise, J.-M., Djalal, S., Docclo, A., Drummond, R., Dupuis, O., Exil, G., Fauré, C., Gaboriaud, A., Gamet, P., Gavalda, P., Grolleau, E., Gueguen, L., Guivarc'h, V., Guterman, P., Hasiba, J., Huntzinger, G., Hustaix, H., Imbert, C., Jeanville, G., Johlander, B., Jorda, L., Journoud, P., Karioty, F., Kerjean, L., Lafond, L., Lapeyrere, V., Landiech, P., Larqué, T., Laudet, P., Le Merrer, J., Leporati, L., Leruyet, B., Levieuge, B., Llebaria, A., Martin, L., Mazy, E., Mesnager, J.-M., Michel, J.-P., Moalic, J.-P., Monjoin, W., Naudet, D., Neukirchner, S., Nguyen-Kim, K., Ollivier, M., Orcesi, J.-L., Ottacher, H., Oulali, A., Parisot, J., Perruchot, S., Piacentino, A., Pinheiro da Silva, L., Platzer, J., Pontet, B., Pradines, A., Quentin, C., Rohbeck, U., Rolland, G., Rollenhagen, F., Romagnan, R., Russ, N., Samadi, R., Schmidt, R., Schwartz, N., Sebbag, I., Smit, H., Sunter, W., Tello, M., Toulouse, P., Ulmer, B., Vandermarcq, O., Vergnault, E., Wallner, R., Waultier, G., and Zanatta, P., "The CoRoT satellite in flight: Description and performance", *Astronomy and Astrophysics*, 2009, 506(1), 411.

Babcock, H. W., "Zeeman Effect in Stellar Spectra.", *The Astrophysical Journal*, 1947, 105, 105.

Baglin, A., Chaintreuil, S., and Vandermarcq, O., "II.1 The CoRoT observations", in CoRot Team and A. Baglin, editors, "The CoRoT Legacy Book", page 29, EDP Sciences, 2016.

Bagnuolo, W. G., Jr. and Barry, D. J., "Plaskett's Star (HD 47129): Still More Curious", *The Astrophysical Journal*, 1996, 469, 347.

Barron, J. A. O. and Wade, G. A., *TESS Photometry of the Of?P Stars HD 148937 and LMC 164-2*, 2021.

Barron, J. A. O., Wade, G. A., Munoz, M. S., David-Uraz, A., Bowman, D. M., Burssens, S., Holgado, G., Petit, V., Simon-Diaz, S., and Mob-

ster Collaboration, *MOBSTER: Identifying Candidate Magnetic O Stars through Rotational Modulation of TESS Photometry*, 2021.

Berdyugina, S. V. and Järvinen, S. P., "Spot activity cycles and flip-flops on young solar analogs", *Astronomische Nachrichten*, 2005, 326, 283.

Bessell, M. S., "UBVRI passbands.", *Publications of the Astronomical Society of the Pacific*, 1990, 102, 1181.

Bessell, M. S., "Standard Photometric Systems", *Annual Review of Astronomy and Astrophysics*, 2005, 43(1), 293.

Blomme, R., Mahy, L., Catala, C., Cuypers, J., Gosset, E., Godart, M., Montalban, J., Ventura, P., Rauw, G., Morel, T., Degroote, P., Aerts, C., Noels, A., Michel, E., Baudin, F., Baglin, A., Auvergne, M., and Samadi, R., "Variability in the CoRoT photometry of three hot O-type stars. HD 46223, HD 46150, and HD 46966", *Astronomy & Astrophysics*, 2011, 533, A4.

Bodensteiner, J., Shenar, T., Mahy, L., Fabry, M., Marchant, P., Abdul-Masih, M., Banyard, G., Bowman, D. M., Dsilva, K., Frost, A. J., Hawcroft, C., Reggiani, M., and Sana, H., "Is HR 6819 a triple system containing a black hole?: An alternative explanation", *Astronomy & Astrophysics*, 2020, 641, A43.

Boisnard, L. and Auvergne, M., "CoRoT in Brief", , 2006, 1306, 19.

Bowman, D. M., Aerts, C., Johnston, C., Pedersen, M. G., Rogers, T. M., Edelmann, P. V. F., Simón-Díaz, S., Van Reeth, T., Buysschaert, B., Tkachenko, A., and Triana, S. A., "Photometric detection of internal gravity waves in upper main-sequence stars: I. Methodology and application to CoRoT targets", *Astronomy & Astrophysics*, 2019a, 621, A135.

Bowman, D. M., Burssens, S., Pedersen, M. G., Johnston, C., Aerts, C., Buysschaert, B., Michielsen, M., Tkachenko, A., Rogers, T. M., Edelmann, P. V. F., Ratnasingam, R. P., Simón-Díaz, S., Castro, N., Moravveji, E., Pope, B. J. S., White, T. R., and De Cat, P., "Low-frequency gravity waves in blue supergiants revealed by high-precision space photometry", *Nature Astronomy*, 2019b, 3, 760.

Bowman, D. M., Burssens, S., Simón-Díaz, S., Edelmann, P. V. F., Rogers, T. M., Horst, L., Röpke, F. K., and Aerts, C., "Photometric detection of internal gravity waves in upper main-sequence stars. II. Combined TESS

photometry and high-resolution spectroscopy", *Astronomy & Astrophysics*, 2020, 640, A36.

Braithwaite, J., "The nature and origin of magnetic fields in early-type stars", , 2014, 302, 255.

Braithwaite, J. and Cantiello, M., "Weak magnetic fields in early-type stars: Failed fossils", *Monthly Notices of the Royal Astronomical Society*, 2013, 428, 2789.

Braithwaite, J. and Spruit, H. C., "A fossil origin for the magnetic field in A stars and white dwarfs", *Nature*, 2004, 431, 819.

Breger, M., Stich, J., Garrido, R., Martin, B., Jiang, S.-Y., Li, Z.-P., Hube, D. P., Ostermann, W., Paparo, M., and Scheck, M., "Nonradial pulsation of the delta Scuti star BU CANCRI in the Praesepe cluster.", *Astronomy and Astrophysics, Vol. 271, p. 482-486 (1993)*, 1993, 271, 482.

Brocksopp, C., Tarasov, A. E., Lyuty, V. M., and Roche, P., "An improved orbital ephemeris for Cygnus X-1", *Astronomy and Astrophysics, v.343, p.861-864 (1999)*, 1999, 343, 861.

Brott, I., de Mink, S. E., Cantiello, M., Langer, N., de Koter, A., Evans, C. J., Hunter, I., Trundle, C., and Vink, J. S., "Rotating massive main-sequence stars. I. Grids of evolutionary models and isochrones", *Astronomy &amp; Astrophysics, Volume 530, id.A115, <NUMPAGES>20</NUMPAGES> pp.*, 2011, 530, A115.

Burssens, S., Simón-Díaz, S., Bowman, D. M., Holgado, G., Michielsen, M., de Burgos, A., Castro, N., Barbá, R. H., and Aerts, C., "Variability of OB stars from TESS southern Sectors 1–13 and high-resolution IACOB and OWN spectroscopy", *Astronomy & Astrophysics*, 2020, 639, A81.

Carter, J. A., Rappaport, S., and Fabrycky, D., "A Third Hot White Dwarf Companion Detected by Kepler", *The Astrophysical Journal*, 2011, 728, 139.

Casares, J., Negueruela, I., Ribó, M., Ribas, I., Paredes, J. M., Herrero, A., and Simón-Díaz, S., "A Be-type star with a black-hole companion", *Nature*, 2014, 505, 378.

Cassinelli, J. P., "Stellar Winds", *Annual Review of Astronomy and Astrophysics*, 1979, 17(1), 275.

Castor, J. I., Abbott, D. C., and Klein, R. I., "Radiation-driven winds in Of stars.", *The Astrophysical Journal*, 1975, 195, 157.

Charbonneau, P. and MacGregor, K. B., "Magnetic Fields in Massive Stars. I. Dynamo Models", *The Astrophysical Journal*, 2001, 559, 1094.

Chen, L., de Grijs, R., and Zhao, J. L., "Mass Segregation in Very Young Open Clusters: A Case Study of NGC 2244 and NGC 6530", *The Astronomical Journal*, 2007, 134, 1368.

Chini, R., Hoffmeister, V. H., Nasseri, A., Stahl, O., and Zinnecker, H., "A spectroscopic survey on the multiplicity of high-mass stars", *Monthly Notices of the Royal Astronomical Society*, 2012, 424, 1925.

Chiosi, C. and Maeder, A., "The Evolution of Massive Stars with Mass Loss", *Annual Review of Astronomy and Astrophysics*, 1986, 24(1), 329.

Conroy, K. E., Kochoska, A., Hey, D., Pablo, H., Hambleton, K. M., Jones, D., Giammarco, J., Abdul-Masih, M., and Prša, A., "Physics of Eclipsing Binaries. V. General Framework for Solving the Inverse Problem", *The Astrophysical Journal Supplement Series*, 2020, 250, 34.

Crowther, P. A., Schnurr, O., Hirschi, R., Yusof, N., Parker, R. J., Goodwin, S. P., and Kassim, H. A., "The R136 star cluster hosts several stars whose individual masses greatly exceed the accepted 150Msolar stellar mass limit", *Monthly Notices of the Royal Astronomical Society*, 2010, 408, 731.

Cumming, A., Marcy, G. W., and Butler, R. P., "The Lick Planet Search: Detectability and Mass Thresholds", *The Astrophysical Journal*, 1999, 526, 890.

Cunha, M. S., Antoci, V., Holdsworth, D. L., Kurtz, D. W., Balona, L. A., Bognár, Z., Bowman, D. M., Guo, Z., Kołaczek-Szymański, P. A., Lares-Martiz, M., Paunzen, E., Skarka, M., Smalley, B., Sódor, Á., Kochukhov, O., Pepper, J., Richey-Yowell, T., Ricker, G. R., Seager, S., Buzasi, D. L., Fox-Machado, L., Hasanzadeh, A., Niemczura, E., Quitral-Manosalva, P., Monteiro, M. J. P. F. G., Stateva, I., De Cat, P., García Hernández, A., Ghasemi, H., Handler, G., Hey, D., Matthews, J. M., Nemec, J. M., Pascual-Granado, J., Safari, H., Suárez, J. C., Szabó, R., Tkachenko, A., and Weiss, W. W., "Rotation and pulsation in Ap stars: First light results from TESS sectors 1 and 2", *Monthly Notices of the Royal Astronomical Society*, 2019, 487, 3523.

David-Uraz, A., Neiner, C., Sikora, J., Bowman, D. M., Petit, V., Chowdhury, S., Handler, G., Pergeorelis, M., Cantiello, M., Cohen, D. H., Erba, C., Keszthelyi, Z., Khalack, V., Kobzar, O., Kochukhov, O., Labadie-Bartz, J., Lovekin, C. C., MacInnis, R., Owocki, S. P., Pablo, H., Shultz, M. E., ud-Doula, A., Wade, G. A., and MOBSTER Collaboration, "Magnetic OB[A] Stars with TESS: Probing their Evolutionary and Rotational properties (MOBSTER) – I. First-light observations of known magnetic B and A stars", *Monthly Notices of the Royal Astronomical Society*, 2019, 487(1), 304.

de Mink, S. E., Sana, H., Langer, N., Izzard, R. G., and Schneider, F. R. N., "The Incidence of Stellar Mergers and Mass Gainers among Massive Stars", *The Astrophysical Journal*, 2014, 782, 7.

Deeming, T. J., "Fourier analysis with unequally-spaced data", *Astrophysics and Space Science*, 1975, 36(1), 137.

Degroote, P., Aerts, C., Ollivier, M., Miglio, A., Debosscher, J., Cuypers, J., Briquet, M., Montalbán, J., Thoul, A., Noels, A., De Cat, P., Balaguer-Núñez, L., Maceroni, C., Ribas, I., Auvergne, M., Baglin, A., Deleuil, M., Weiss, W. W., Jorda, L., Baudin, F., and Samadi, R., "CoRoT's view of newly discovered B-star pulsators: Results for 358 candidate B pulsators from the initial run's exoplanet field data", *Astronomy & Astrophysics*, 2009a, 506(1), 471.

Degroote, P., Briquet, M., Catala, C., Uytterhoeven, K., Lefever, K., Morel, T., Aerts, C., Carrier, F., Auvergne, M., Baglin, A., and Michel, E., "Evidence for nonlinear resonant mode coupling in the $\mathsf{\beta}$ Cephei starHD 180642 (V1449 Aquilae) from CoRoT photometry", *Astronomy & Astrophysics*, 2009b, 506(1), 111.

Donati, J.-F. and Landstreet, J., "Magnetic Fields of Nondegenerate Stars", *Annual Review of Astronomy and Astrophysics*, 2009, 47(1), 333.

Donati, J. F., Mengel, M., Carter, B. D., Marsden, S., Collier Cameron, A., and Wichmann, R., "Surface differential rotation and prominences of the Lupus post T Tauri star RX J1508.6-4423", *Monthly Notices of the Royal Astronomical Society*, 2000, 316, 699.

Donati, J. F., Moutou, C., Farès, R., Bohlender, D., Catala, C., Deleuil, M., Shkolnik, E., Collier Cameron, A., Jardine, M. M., and Walker, G. A. H., "Magnetic cycles of the planet-hosting star $\tau$ Bootis", *Monthly Notices of the Royal Astronomical Society*, 2008, 385, 1179.

Dworetsky, M. M., "A period-finding method for sparse randomly spaced observations or "How Long Is a Piece of String ?"", *Monthly Notices of the Royal Astronomical Society*, 1983, 203, 917.

Ekström, S., Georgy, C., Eggenberger, P., Meynet, G., Mowlavi, N., Wyttenbach, A., Granada, A., Decressin, T., Hirschi, R., Frischknecht, U., Charbonnel, C., and Maeder, A., "Grids of stellar models with rotation: I. Models from 0.8 to 120 $M_\odot$ at solar metallicity ( $Z = 0.014)\star$", *Astronomy & Astrophysics*, 2012, 537, A146.

El-Badry, K. and Quataert, E., "A stripped-companion origin for Be stars: Clues from the putative black holes HR 6819 and LB-1", *Monthly Notices of the Royal Astronomical Society*, 2021, 502(3), 3436.

ESA, "The HIPPARCOS and TYCHO catalogues. Astrometric and photometric star catalogues derived from the ESA HIPPARCOS Space Astrometry Mission", *ESA Special Publication*, 1997a, 1200.

ESA, "VizieR Online Data Catalog: The Hipparcos and Tycho Catalogues (ESA 1997)", *VizieR Online Data Catalog*, 1997b, page I/239.

Faigler, S. and Mazeh, T., "Photometric detection of non-transiting short-period low-mass companions through the beaming, ellipsoidal and reflection effects in Kepler and CoRoT light curves", *Monthly Notices of the Royal Astronomical Society*, 2011, 415, 3921.

Ferraz-Mello, S., "Estimation of Periods from Unequally Spaced Observations", *The Astronomical Journal*, 1981, 86, 619.

Folsom, C. P., Bouvier, J., Petit, P., Lèbre, A., Amard, L., Palacios, A., Morin, J., Donati, J. F., and Vidotto, A. A., "The evolution of surface magnetic fields in young solar-type stars II: The early main sequence (250-650 Myr)", *Monthly Notices of the Royal Astronomical Society*, 2018, 474, 4956.

Folsom, C. P., Kochukhov, O., Wade, G. A., Silvester, J., and Bagnulo, S., "Magnetic field, chemical composition and line profile variability of the peculiar eclipsing binary star AR Aur", *Monthly Notices of the Royal Astronomical Society*, 2010, 407(4), 2383.

Fossati, L., Castro, N., Schöller, M., Hubrig, S., Langer, N., Morel, T., Briquet, M., Herrero, A., Przybilla, N., Sana, H., Schneider, F. R. N., de Koter, A., and Collaboration, t. B., "B fields in OB stars (BOB): Low-resolution FORS2 spectropolarimetry of the first sample of 50 massive stars", *Astronomy & Astrophysics*, 2015, 582, A45.

Friend, D. B. and MacGregor, K. B., "Winds from rotating, magnetic, hot stars. I. General model results.", *The Astrophysical Journal*, 1984, 282, 591.

Frost, A. J., Bodensteiner, J., Rivinius, T., Baade, D., Merand, A., Selman, F., Abdul-Masih, M., Banyard, G., Bordier, E., Dsilva, K., Hawcroft, C., Mahy, L., Reggiani, M., Shenar, T., Cabezas, M., Hadrava, P., Heida, M., Klement, R., and Sana, H., "HR 6819 is a binary system with no black hole: Revisiting the source with infrared interferometry and optical integral field spectroscopy", *Astronomy & Astrophysics*, 2022, 659, L3.

Gaidos, E. J., Henry, G. W., and Henry, S. M., "Spectroscopy and Photometry of Nearby Young Solar Analogs", *The Astronomical Journal*, 2000, 120, 1006.

Gilliland, R. L. and Baliunas, S. L., "Objective Characterization of Stellar Activity Cycles. I. Methods and Solar Cycle Analyses", *The Astrophysical Journal*, 1987, 314, 766.

Giuricin, G., Mardirossian, F., and Mezzetti, M., "Synchronization in early-type spectroscopic binary stars.", *Astronomy and Astrophysics*, 1984, 135, 393.

González, J. F. and Levato, H., "Separation of composite spectra: The spectroscopic detection of aneclipsing binary star", *Astronomy & Astrophysics*, 2006, 448(1), 283.

Götberg, Y., de Mink, S. E., Groh, J. H., Kupfer, T., Crowther, P. A., Zapartas, E., and Renzo, M., "Spectral models for binary products: Unifying subdwarfs and Wolf-Rayet stars as a sequence of stripped-envelope stars", *Astronomy & Astrophysics*, 2018, 615, A78.

Graham, M. J., Drake, A. J., Djorgovski, S. G., Mahabal, A. A., Donalek, C., Duan, V., and Maker, A., "A comparison of period finding algorithms", *Monthly Notices of the Royal Astronomical Society*, 2013, 434, 3423.

Gregory, P. C. and Loredo, T. J., "A New Method for the Detection of a Periodic Signal of Unknown Shape and Period", *The Astrophysical Journal*, 1992, 398, 146.

Grisdale, K. M., "The Role of Stellar Feedback on the Structure of the ISM and Star Formation in Galaxies", Ph.D. thesis, 2017.

Grunhut, J. H., Wade, G. A., Folsom, C. P., Neiner, C., Kochukhov, O., Alecian, E., Shultz, M., Petit, V., MiMeS Collaboration, and BinaMIcS Collaboration, "The magnetic field and magnetosphere of Plaskett's star: A fundamental shift in our understanding of the system", *Monthly Notices of the Royal Astronomical Society*, 2022, 512, 1944.

Grunhut, J. H., Wade, G. A., Leutenegger, M., Petit, V., Rauw, G., Neiner, C., Martins, F., Cohen, D. H., Gagné, M., Ignace, R., Mathis, S., de Mink, S. E., Moffat, A. F. J., Owocki, S., Shultz, M., Sundqvist, J., and MiMeS Collaboration, "Discovery of a magnetic field in the rapidly rotating O-type secondary of the colliding-wind binary HD 47129 (Plaskett's star)", *Monthly Notices of the Royal Astronomical Society*, 2013, 428, 1686.

Grunhut, J. H., Wade, G. A., Neiner, C., Oksala, M. E., Petit, V., Alecian, E., Bohlender, D. A., Bouret, J. C., Henrichs, H. F., Hussain, G. A. J., Kochukhov, O., and MiMeS Collaboration, "The MiMeS survey of Magnetism in Massive Stars: Magnetic analysis of the O-type stars", *Monthly Notices of the Royal Astronomical Society*, 2017, 465, 2432.

Hale, G. E., "On the Probable Existence of a Magnetic Field in Sun-Spots", *The Astrophysical Journal*, 1908, 28, 315.

Harris, C. R., Millman, K. J., van der Walt, S. J., Gommers, R., Virtanen, P., Cournapeau, D., Wieser, E., Taylor, J., Berg, S., Smith, N. J., Kern, R., Picus, M., Hoyer, S., van Kerkwijk, M. H., Brett, M., Haldane, A., del Río, J. F., Wiebe, M., Peterson, P., Gérard-Marchant, P., Sheppard, K., Reddy, T., Weckesser, W., Abbasi, H., Gohlke, C., and Oliphant, T. E., "Array programming with NumPy", *Nature*, 2020, 585(7825), 357.

Heck, A., Manfroid, J., and Mersch, G., "On period determination methods", *Astronomy and Astrophysics Supplement Series*, 1985, 59, 63.

Heger, A., Fryer, C. L., Woosley, S. E., Langer, N., and Hartmann, D. H., "How Massive Single Stars End Their Life", *The Astrophysical Journal*, 2003, 591, 288.

Hertz, P., "NASA Response to the 2019 Astrophysics Senior Review of Operating Missions", , 2019.

Horvat, M., Conroy, K. E., Pablo, H., Hambleton, K. M., Kochoska, A., Giammarco, J., and Prša, A., "Physics of Eclipsing Binaries. III. Spin-Orbit Misalignment", *The Astrophysical Journal Supplement Series*, 2018, 237, 26.

Hunter, J. D., "Matplotlib: A 2D Graphics Environment", *Computing in Science & Engineering*, 2007, 9(3), 90.

Hurley, J. R., Tout, C. A., and Pols, O. R., "Evolution of binary stars and the effect of tides on binary populations", *Monthly Notices of the Royal Astronomical Society*, 2002, 329(4), 897.

Irwin, A. W., Campbell, B., Morbey, C. L., Walker, G. A. H., and Yang, S., "Long-Period Radial-Velocity Variations of Arcturus", *Publications of the Astronomical Society of the Pacific*, 1989, 101, 147.

Jermyn, A. S. and Cantiello, M., "The Origin of the Bimodal Distribution of Magnetic Fields in Early-type Stars", *The Astrophysical Journal*, 2020, 900, 113.

Johnson, H. L. and Morgan, W. W., "Fundamental stellar photometry for standards of spectral type on the Revised System of the Yerkes Spectral Atlas.", *The Astrophysical Journal*, 1953, 117, 313.

Jones, D., Conroy, K. E., Horvat, M., Giammarco, J., Kochoska, A., Pablo, H., Brown, A. J., Sowicka, P., and Prša, A., "Physics of Eclipsing Binaries. IV. The Impact of Interstellar Extinction on the Light Curves of Eclipsing Binaries", *The Astrophysical Journal Supplement Series*, 2020, 247, 63.

Kepler, S. O., "Light and line profile variations die to R-mode pusations with an application to the ZZ Ceti star G 117-B15A.", *The Astrophysical Journal*, 1984, 286, 314.

Keszthelyi, Z., Meynet, G., Georgy, C., Wade, G. A., Petit, V., and David-Uraz, A., "The effects of surface fossil magnetic fields on massive star evolution: I. Magnetic field evolution, mass-loss quenching, and magnetic braking", *Monthly Notices of the Royal Astronomical Society*, 2019, 485(4), 5843.

Khaliullin, K. F. and Khaliullina, A. I., "Synchronization and circularization in early-type binaries on main sequence", *Monthly Notices of the Royal Astronomical Society*, 2010, 401(1), 257.

Kippenhahn, R., Weigert, A., and Weiss, A., *Stellar Structure and Evolution*, Astronomy and Astrophysics Library, Springer Berlin Heidelberg, Berlin, Heidelberg, 2012.

Kobulnicky, H. A., Kiminki, D. C., Lundquist, M. J., Burke, J., Chapman, J., Keller, E., Lester, K., Rolen, E. K., Topel, E., Bhattacharjee, A., Smullen,

R. A., Vargas Álvarez, C. A., Runnoe, J. C., Dale, D. A., and Brotherton, M. M., "Toward Complete Statistics of Massive Binary Stars: Penultimate Results from the Cygnus OB2 Radial Velocity Survey", *The Astrophysical Journal Supplement Series*, 2014, 213, 34.

Kołaczek-Szymański, P. A., Pigulski, A., Michalska, G., Moździerski, D., and Różański, T., "Massive heartbeat stars from TESS: I. TESS sectors 1–16", *Astronomy & Astrophysics*, 2021, 647, A12.

Langer, N., "Presupernova Evolution of Massive Single and Binary Stars", *Annual Review of Astronomy and Astrophysics*, 2012, 50(1), 107.

Lauterborn, D., "Evolution with mass exchange of case C for a binary system of total mass 7 M sun.", *Astronomy and Astrophysics*, 1970, 7, 150.

Lenz, P. and Breger, M., "Period04 User Guide", *Communications in Asteroseismology*, 2005, 146, 53.

Levato, H., "Synchronization in binaries and age.", *The Astrophysical Journal*, 1976, 203, 680.

Lightkurve Collaboration, Cardoso, J. V. d. M., Hedges, C., Gully-Santiago, M., Saunders, N., Cody, A. M., Barclay, T., Hall, O., Sagear, S., Turtelboom, E., Zhang, J., Tzanidakis, A., Mighell, K., Coughlin, J., Bell, K., Berta-Thompson, Z., Williams, P., Dotson, J., and Barentsen, G., "Lightkurve: Kepler and TESS time series analysis in Python", Astrophysics Source Code Library, 2018.

Lignières, F., Petit, P., Böhm, T., and Aurière, M., "First evidence of a magnetic field on Vega: Towards a new class of magnetic A-type stars", *Astronomy & Astrophysics*, 2009, 500(3), L41.

Linder, N., Rauw, G., Martins, F., Sana, H., De Becker, M., and Gosset, E., "High resolution optical spectroscopy of Plaskett's star", *Astronomy & Astrophysics*, 2008, 489(2), 713.

Linder, N., Rauw, G., Pollock, A. M. T., and Stevens, I. R., "The XMM-Newton view of Plaskett's star and its surroundings", *Monthly Notices of the Royal Astronomical Society*, 2006, 370, 1623.

Lomb, N. R., "Least-Squares Frequency Analysis of Unequally Spaced Data", *Astrophysics and Space Science*, 1976, 39(2), 447.

Loumos, G. L. and Deeming, T. J., "Spurious Results from Fourier Analysis of Data with Closely Spaced Frequencies", *Astrophysics and Space Science*, 1978, 56(2), 285.

Lund, M. N., Handberg, R., Buzasi, D. L., Carboneau, L., Hall, O. J., Pereira, F., Huber, D., Hey, D., Van Reeth, T., and T'DA Collaboration, "TESS Data for Asteroseismology: Light-curve Systematics Correction", *The Astrophysical Journal Supplement Series*, 2021, 257, 53.

MacDonald, J. and Mullan, D. J., "Magnetic fields in massive stars: Dynamics and origin", *Monthly Notices of the Royal Astronomical Society*, 2004, 348, 702.

MacGregor, K. B. and Cassinelli, J. P., "Magnetic Fields in Massive Stars. II. The Buoyant Rise of Magnetic Flux Tubes through the Radiative Interior", *The Astrophysical Journal*, 2003, 586, 480.

Maeder, A. and Meynet, G., "Stellar evolution with rotation. VI. The Eddington and Omega -Limits, the rotational mass loss for OB and LBV stars", *Astronomy and Astrophysics*, 2000, 361, 159.

Mahy, L., Gosset, E., Baudin, F., Rauw, G., Godart, M., Morel, T., Degroote, P., Aerts, C., Blomme, R., Cuypers, J., Noels, A., Michel, E., Baglin, A., Auvergne, M., Catala, C., and Samadi, R., "Plaskett's Star: Analysis of the CoRoT photometric data", *Astronomy & Astrophysics*, 2011, 525, A101.

Martins, F., Schaerer, D., and Hillier, D. J., "A new calibration of stellar parameters of Galactic O stars", *Astronomy and Astrophysics*, 2005, 436(3), 1049.

Messina, S. and Guinan, E. F., "Magnetic activity of six young solar analogues I. Starspot cycles from long-term photometry", *Astronomy & Astrophysics*, 2002, 393(1), 225.

Moffat, A. F. J., "Pulsations of Massive Stars", , 2012, 465, 3.

Montgomery, M. H. and O'Donoghue, D., "A derivation of the errors for least squares fitting to time series data", *Delta Scuti Star Newsletter*, 1999, 13, 28.

Morris, S. L., "The ellipsoidal variable stars.", *The Astrophysical Journal*, 1985, 295, 143.

Neiner, C., Morin, J., and Alecian, E., *The "Binarity and Magnetic Interactions in Various Classes of Stars" (BinaMIcS) Project*, eprint: arXiv:1510.02121, 2015.

Newville, M., Stensitzki, T., Allen, D. B., and Ingargiola, A., "LMFIT: Non-Linear Least-Square Minimization and Curve-Fitting for Python", Zenodo, 2014.

Orosz, J. A., McClintock, J. E., Aufdenberg, J. P., Remillard, R. A., Reid, M. J., Narayan, R., and Gou, L., "The Mass of the Black Hole in Cygnus X-1", *The Astrophysical Journal*, 2011, 742, 84.

Paczyński, B., "Evolutionary Processes in Close Binary Systems", *Annual Review of Astronomy and Astrophysics*, 1971, 9, 183.

Palmer, D. M., "A Fast Chi-Squared Technique for Period Search of Irregularly Sampled Data", *The Astrophysical Journal*, 2009, 695, 496.

Pan, K.-K., "Synchronization in the early-type detached binary stars.", *Astronomy and Astrophysics*, 1997, 321, 202.

Papaloizou, J. and Pringle, J. E., "Gravitational radiation and the stability of rotating stars.", *Monthly Notices of the Royal Astronomical Society*, 1978, 184, 501.

Petit, P., Lignières, F., Wade, G. A., Aurière, M., Böhm, T., Bagnulo, S., Dintrans, B., Fumel, A., Grunhut, J., Lanoux, J., Morgenthaler, A., and Van Grootel, V., "The rapid rotation and complex magnetic field geometry of Vega", *Astronomy & Astrophysics*, 2010, 523, A41.

Petit, V., Owocki, S. P., Wade, G. A., Cohen, D. H., Sundqvist, J. O., Gagné, M., Maíz Apellániz, J., Oksala, M. E., Bohlender, D. A., Rivinius, T., Henrichs, H. F., Alecian, E., Townsend, R. H. D., ud-Doula, A., and MiMeS Collaboration, "A magnetic confinement versus rotation classification of massive-star magnetospheres", *Monthly Notices of the Royal Astronomical Society*, 2013, 429, 398.

Plaskett, J. S., "A very massive star", *Monthly Notices of the Royal Astronomical Society*, 1922, 82, 447.

Plavec, M., "Rotation in Close Binaries", *International Astronomical Union Colloquium*, 1970, 4, 132.

Pojmanski, G., "The All Sky Automated Survey", , 1997.

Prša, A., Conroy, K. E., Horvat, M., Pablo, H., Kochoska, A., Bloemen, S., Giammarco, J., Hambleton, K. M., and Degroote, P., "Physics Of Eclipsing Binaries. II. Toward the Increased Model Fidelity", *The Astrophysical Journal Supplement Series*, 2016, 227, 29.

Prša, A., Kochoska, A., Conroy, K. E., Eisner, N., Hey, D. R., IJspeert, L., Kruse, E., Fleming, S. W., Johnston, C., Kristiansen, M. H., LaCourse, D., Mortensen, D., Pepper, J., Stassun, K. G., Torres, G., Abdul-Masih, M., Chakraborty, J., Gagliano, R., Guo, Z., Hambleton, K., Hong, K., Jacobs, T., Jones, D., Kostov, V., Lee, J. W., Omohundro, M., Orosz, J. A., Page, E. J., Powell, B. P., Rappaport, S., Reed, P., Schnittman, J., Schwengeler, H. M., Shporer, A., Terentev, I. A., Vanderburg, A., Welsh, W. F., Caldwell, D. A., Doty, J. P., Jenkins, J. M., Latham, D. W., Ricker, G. R., Seager, S., Schlieder, J. E., Shiao, B., Vanderspek, R., and Winn, J. N., "TESS Eclipsing Binary Stars. I. Short-cadence Observations of 4584 Eclipsing Binaries in Sectors 1–26", *The Astrophysical Journal Supplement Series*, 2022, 258(1), 16.

Prša, A. and Zwitter, T., "A Computational Guide to Physics of Eclipsing Binaries. I. Demonstrations and Perspectives", *The Astrophysical Journal*, 2005, 628, 426.

Reimann, J. D., "Frequency Estimation Using Unequally-Spaced Astronomical Data.", Ph.D. thesis, 1994.

Ricker, G. R., Winn, J. N., Vanderspek, R., Latham, D. W., Bakos, G. Á., Bean, J. L., Berta-Thompson, Z. K., Brown, T. M., Buchhave, L., Butler, N. R., Butler, R. P., Chaplin, W. J., Charbonneau, D., Christensen-Dalsgaard, J., Clampin, M., Deming, D., Doty, J., De Lee, N., Dressing, C., Dunham, E. W., Endl, M., Fressin, F., Ge, J., Henning, T., Holman, M. J., Howard, A. W., Ida, S., Jenkins, J. M., Jernigan, G., Johnson, J. A., Kaltenegger, L., Kawai, N., Kjeldsen, H., Laughlin, G., Levine, A. M., Lin, D., Lissauer, J. J., MacQueen, P., Marcy, G., McCullough, P. R., Morton, T. D., Narita, N., Paegert, M., Palle, E., Pepe, F., Pepper, J., Quirrenbach, A., Rinehart, S. A., Sasselov, D., Sato, B., Seager, S., Sozzetti, A., Stassun, K. G., Sullivan, P., Szentgyorgyi, A., Torres, G., Udry, S., and Villasenor, J., "Transiting Exoplanet Survey Satellite (TESS)", *Journal of Astronomical Telescopes, Instruments, and Systems*, 2015, 1, 014003.

Rivinius, T., Baade, D., Hadrava, P., Heida, M., and Klement, R., "A naked-eye triple system with a nonaccreting black hole in the inner binary", *Astronomy & Astrophysics*, 2020, 637, L3.

Robinson, E. L., Kepler, S. O., and Nather, R. E., "Multicolor variations of the ZZ CET stars.", *The Astrophysical Journal*, 1982, 259, 219.

Saio, H., "R-mode oscillations in uniformly rotating stars", *The Astrophysical Journal*, 1982, 256, 717.

Saio, H., Kurtz, D. W., Murphy, S. J., Antoci, V. L., and Lee, U., "Theory and evidence of global Rossby waves in upper main-sequence stars: R-mode oscillations in many Kepler stars", *Monthly Notices of the Royal Astronomical Society*, 2018, 474, 2774.

Sana, H., "The multiplicity of massive stars: A 2016 view", *Proceedings of the International Astronomical Union*, 2016, 12(S329), 110.

Sana, H., de Mink, S. E., de Koter, A., Langer, N., Evans, C. J., Gieles, M., Gosset, E., Izzard, R. G., Le Bouquin, J. B., and Schneider, F. R. N., "Binary Interaction Dominates the Evolution of Massive Stars", *Science (New York, N.Y.)*, 2012, 337, 444.

Sana, H., Le Bouquin, J. B., Lacour, S., Berger, J. P., Duvert, G., Gauchet, L., Norris, B., Olofsson, J., Pickel, D., Zins, G., Absil, O., de Koter, A., Kratter, K., Schnurr, O., and Zinnecker, H., "Southern Massive Stars at High Angular Resolution: Observational Campaign and Companion Detection", *The Astrophysical Journal Supplement Series*, 2014, 215, 15.

Scargle, J. D., "Studies in astronomical time series analysis. II. Statistical aspects of spectral analysis of unevenly spaced data.", *The Astrophysical Journal*, 1982, 263, 835.

Schneider, F. R. N., Ohlmann, S. T., Podsiadlowski, P., Röpke, F. K., Balbus, S. A., Pakmor, R., and Springel, V., "Stellar mergers as the origin of magnetic massive stars", *Nature*, 2019, 574, 211.

Schwarzenberg-Czerny, A., "On the advantage of using analysis of variance for period search.", *Monthly Notices of the Royal Astronomical Society*, 1989, 241, 153.

Schwarzenberg-Czerny, A., "Accuracy of period determination", *Monthly Notices of the Royal Astronomical Society*, 1991, 253, 198.

Schwarzenberg-Czerny, A., "Optimum Period Search: Quantitative Analysis", *The Astrophysical Journal*, 1999, 516, 315.

Schwarzenberg-Czerny, A., "An astronomer's guide to period searching", *Interplay of Periodic, Cyclic and Stochastic Variability in Selected Areas of the H-R Diagram*, 2003, 292, 383.

Shultz, M., Wade, G., Rivinius, T., Townsend, R., and the MiMeS Collaboration, "Emission from the Centrifugal Magnetospheres of Magnetic B-type Stars", , 2014.

Shultz, M., Wade, G. A., Alecian, E., and BinaMIcS Collaboration, "Detection of magnetic fields in both B-type components of the $\varepsilon$ Lupi system: A new constraint on the origin of fossil fields?", *Monthly Notices of the Royal Astronomical Society*, 2015, 454, L1.

Skilling, J. and Bryan, R. K., "Maximum Entropy Image Reconstruction - General Algorithm", *Monthly Notices of the Royal Astronomical Society*, 1984, 211, 111.

Smith, J. C., Stumpe, M. C., Jenkins, J. M., Van Cleve, J. E., Girouard, F. R., Kolodziejczak, J. J., McCauliff, S. D., Morris, R. L., and Twicken, J. D., "Presearch data conditioning in Kepler Data Processing Handbook: KSCI-19081-003", , 2020.

Smith, N., "Mass Loss: Its Effect on the Evolution and Fate of High-Mass Stars", *Annual Review of Astronomy and Astrophysics*, 2014, 52(1), 487.

Song, H. F., Meynet, G., Maeder, A., Ekström, S., and Eggenberger, P., "Massive star evolution in close binaries: Conditions for homogeneous chemical evolution", *Astronomy & Astrophysics*, 2016, 585, A120.

Sota, A., Maíz Apellániz, J., Morrell, N. I., Barbá, R. H., Walborn, N. R., Gamen, R. C., Arias, J. I., and Alfaro, E. J., "The Galactic O-Star Spectroscopic Survey (GOSSS). II. Bright Southern Stars", *The Astrophysical Journal Supplement Series*, 2014, 211, 10.

Spruit, H. C., "Differential rotation and magnetic fields in stellar interiors", *Astronomy and Astrophysics*, 1999, 349, 189.

Spruit, H. C., "Dynamo action by differential rotation in a stably stratified stellar interior", *Astronomy and Astrophysics*, 2002, 381, 923.

Stellingwerf, R. F., "Period determination using phase dispersion minimization.", *The Astrophysical Journal*, 1978, 224, 953.

Stickland, D. J., "Spectroscopic binary orbits from ultraviolet radial velocities. Paper 2: Plaskett's Star", *The Observatory*, 1987, 107, 68.

Sturrock, P. A. and Bertello, L., "Power Spectrum Analysis of Mount Wilson Solar Diameter Measurements: Evidence for Solar Internal r-Mode Oscillations", *The Astrophysical Journal*, 2010, 725, 492.

Sturrock, P. A., Bush, R., Gough, D. O., and Scargle, J. D., "Indications of R-mode Oscillations in SOHO/MDI Solar Radius Measurements", *The Astrophysical Journal*, 2015, 804, 47.

Taam, R. E. and Sandquist, E. L., "Common Envelope Evolution of Massive Binary Stars", *Annual Review of Astronomy and Astrophysics*, 2000, 38(1), 113.

Tassoul, J.-L., "On Synchronization in Early-Type Binaries", *The Astrophysical Journal*, 1987, 322, 856.

Tassoul, J.-L., "On Orbital Circularization in Detached Close Binaries", *The Astrophysical Journal*, 1988, 324, L71.

Thielemann, F.-K., Isern, J., Perego, A., and von Ballmoos, P., "Nucleosynthesis in Supernovae", *Space Science Reviews*, 2018, 214(3), 62.

Thomas, H.-C., "Consequences of mass transfer in close binary systems.", *Annual Review of Astronomy and Astrophysics*, 1977, 15, 127.

Townsend, R. H. D. and Owocki, S. P., "A rigidly rotating magnetosphere model for circumstellar emission from magnetic OB stars", *Monthly Notices of the Royal Astronomical Society*, 2005, 357, 251.

Townsend, R. H. D., Owocki, S. P., and Ud-Doula, A., "A Rigid-Field Hydrodynamics approach to modelling the magnetospheres of massive stars", *Monthly Notices of the Royal Astronomical Society*, 2007, 382, 139.

Turner, N. H., ten Brummelaar, T. A., Roberts, L. C., Mason, B. D., Hartkopf, W. I., and Gies, D. R., "Adaptive Optics Photometry and Astrometry of Binary Stars. III. a Faint Companion Search of O-Star Systems", *The Astronomical Journal*, 2008, 136, 554.

Turon, C., Creze, M., Egret, D., Gomez, A., Grenon, M., Jahreiß, H., Requieme, Y., Argue, A. N., Bec-Borsenberger, A., Dommanget, J., Mennessier, M. O., Arenou, F., Chareton, M., Crifo, F., Mermilliod, J. C., Morin, D., Nicolet, B., Nys, O., Prevot, L., Rousseau, M., Perryman, M.

A. C., Arlot, J. E., Baglin, A., Barthes, D., Baylac, M. O., Brosche, P., Burnet, M., Delhaye, J., Dettbarn, C., Erbach, M., Figueras, F., Fricke, W., Helmer, L., Hemenway, P., Jordi, C., Lampens, P., Lederle, T., Lub, J., Manfroid, J., Mattci, J. A., Mazurier, J. M., Mermilliod, M., Morrison, L. V., Murray, C. A., Oblak, E., Perie, J. P., Pernier, B., Le Poole, R. S., Quijano, L., Rapaport, M., Sellier, A., Torra, J., Tucholke, H. J., de Vegt, C., Argyle, R. W., Bacchus, P., Baron, N., Calaf, J., Cordoni, J. P., Fabricius, C., Feaugas, J. C., Fehlberg, H. J., Florkowski, D. R., de Geus, E., Gibbs, P., Hartmann, L., Jauncey, D. L., Johnston, K. J., Marouard, M., Mekkas, A., Muinos, J. L., Nunez, J., Ochsenbein, F., de Orus, J. J., Paredes, J. M., Penston, M. J., Petersen, C., Peyrin, Y., Robin, A., Roman, V., Rossello, G., Schwan, H., Sinachopoulos, D., White, G. L., Zacharias, N., Hog, E., Kovalevsky, J., van Leeuwen, F., Lindegren, L., Schutz, A., and Schrijver, H., "Version 2 of the HIPPARCOS input catalogue", *Bulletin d'Information du Centre de Donnees Stellaires*, 1993, 43, 5.

Twicken, J. D., Caldwell, D. A., Jenkins, J. M., Tenenbaum, P., Smith, J. C., Wohler, B., Rose, M., Ting, E. B., Vanderspek, R., Morgan, E., Rudat, A., Fausnaugh, M., Fleming, S., and Quintana, E., "TESS Science Data Products Description Document", *NASA*, 2020, EXP-TESS-ARC-ICD-0014(Rev F), 101.

ud-Doula, A., "3D MHD Simulations of Magnetospheres from Obliquely Rotating Magnetic Massive Stars", , 2021.

ud-Doula, A., Owocki, S. P., and Townsend, R. H. D., "Angular momentum loss and stellar spin-down in magnetic massive stars", , 2009, 259, 423.

van Kerkwijk, M. H., Rappaport, S. A., Breton, R. P., Justham, S., Podsiadlowski, P., and Han, Z., "Observations of Doppler Boosting in Kepler Light Curves", *The Astrophysical Journal*, 2010, 715, 51.

Van Reeth, T., Tkachenko, A., and Aerts, C., "Interior rotation of a sample of $\gamma$ Doradus stars from ensemble modelling of their gravity-mode period spacings", *Astronomy & Astrophysics*, 2016, 593, A120.

Vanbeveren, D., De Loore, C., and Van Rensbergen, W., "Massive stars", *Astronomy and Astrophysics Review*, 1998, 9(1-2), 63.

VanderPlas, J. T., "Understanding the Lomb-Scargle Periodogram", *The Astrophysical Journal Supplement Series*, 2018, 236, 16.

Virtanen, P., Gommers, R., Oliphant, T. E., Haberland, M., Reddy, T., Cournapeau, D., Burovski, E., Peterson, P., Weckesser, W., Bright, J., van der Walt, S. J., Brett, M., Wilson, J., Millman, K. J., Mayorov, N., Nelson, A. R. J., Jones, E., Kern, R., Larson, E., Carey, C. J., Polat, İ., Feng, Y., Moore, E. W., VanderPlas, J., Laxalde, D., Perktold, J., Cimrman, R., Henriksen, I., Quintero, E. A., Harris, C. R., Archibald, A. M., Ribeiro, A. H., Pedregosa, F., van Mulbregt, P., SciPy 1.0 Contributors, Vijaykumar, A., Bardelli, A. P., Rothberg, A., Hilboll, A., Kloeckner, A., Scopatz, A., Lee, A., Rokem, A., Woods, C. N., Fulton, C., Masson, C., Häggström, C., Fitzgerald, C., Nicholson, D. A., Hagen, D. R., Pasechnik, D. V., Olivetti, E., Martin, E., Wieser, E., Silva, F., Lenders, F., Wilhelm, F., Young, G., Price, G. A., Ingold, G.-L., Allen, G. E., Lee, G. R., Audren, H., Probst, I., Dietrich, J. P., Silterra, J., Webber, J. T., Slavič, J., Nothman, J., Buchner, J., Kulick, J., Schönberger, J. L., de Miranda Cardoso, J. V., Reimer, J., Harrington, J., Rodríguez, J. L. C., Nunez-Iglesias, J., Kuczynski, J., Tritz, K., Thoma, M., Newville, M., Kümmerer, M., Bolingbroke, M., Tartre, M., Pak, M., Smith, N. J., Nowaczyk, N., Shebanov, N., Pavlyk, O., Brodtkorb, P. A., Lee, P., McGibbon, R. T., Feldbauer, R., Lewis, S., Tygier, S., Sievert, S., Vigna, S., Peterson, S., More, S., Pudlik, T., Oshima, T., Pingel, T. J., Robitaille, T. P., Spura, T., Jones, T. R., Cera, T., Leslie, T., Zito, T., Krauss, T., Upadhyay, U., Halchenko, Y. O., and Vázquez-Baeza, Y., "SciPy 1.0: Fundamental algorithms for scientific computing in Python", *Nature Methods*, 2020, 17(3), 261.

Wade, G. A. and MiMeS Collaboration, "Review: Magnetic Fields of O-Type Stars", *Proceedings of a conference held at Special Astrophysical Observatory, Nizhny Arkhyz, Russia,*, 2015, 494, 30.

Wade, G. A., Neiner, C., Alecian, E., Grunhut, J. H., Petit, V., de Batz, B., Bohlender, D. A., Cohen, D. H., Henrichs, H. F., Kochukhov, O., Landstreet, J. D., Manset, N., Martins, F., Mathis, S., Oksala, M. E., Owocki, S. P., Rivinius, T., Shultz, M. E., Sundqvist, J. O., Townsend, R. H. D., ud-Doula, A., Bouret, J.-C., Braithwaite, J., Briquet, M., Carciofi, A. C., David-Uraz, A., Folsom, C. P., Fullerton, A. W., Leroy, B., Marcolino, W. L. F., Moffat, A. F. J., Nazé, Y., Aurière, M., Bagnulo, S., Bailey, J. D., Barbá, R. H., Blazère, A., Böhm, T., Catala, C., Donati, J.-F., Ferrario, L., Harrington, D., Howarth, I. D., Ignace, R., Kaper, L., Lüftinger, T., Prinja, R., Vink, J. S., Weiss, W. W., and Yakunin, I., "The MiMeS Survey of Magnetism in Massive Stars: Introduction and overview", *Monthly Notices of the Royal Astronomical Society*, 2016, 456(1), 2.

Weinberg, D., Coil, A., Donahue, M., Fortney, J., Fujieh, M., Humphreys, R., McConnell, M., O'Meara, J., Oppenheimer, R., Pope, A., and Sanders, W., "2019 Astrophysics Senior Review - Senior Review Subcommittee Report", Technical report, NASA, 2019.

Weiss, W. W., Rucinski, S. M., Moffat, A. F. J., Schwarzenberg-Czerny, A., Koudelka, O. F., Grant, C. C., Zee, R. E., Kuschnig, R., Mochnacki, S., Matthews, J. M., Orleanski, P., Pamyatnykh, A., Pigulski, A., Alves, J., Guedel, M., Handler, G., Wade, G. A., and Zwintz, K., "BRITE-Constellation: Nanosatellites for Precision Photometry of Bright Stars", *Publications of the Astronomical Society of the Pacific*, 2014, 126, 573.

Wichmann, R., "Nightfall User Manual", , 1998.

Willmer, C. N. A., "The Absolute Magnitude of the Sun in Several Filters", *The Astrophysical Journal Supplement Series*, 2018, 236, 47.

Woosley, S. E., Heger, A., and Weaver, T. A., "The evolution and explosion of massive stars", *Reviews of Modern Physics*, 2002, 74, 1015.

Zahn, J.-P., "Tidal friction in close binary systems.", *Astronomy and Astrophysics*, 1977, 57, 383.

Zahn, J.-P., Brun, A. S., and Mathis, S., "On magnetic instabilities and dynamo action in stellar radiation zones", *Astronomy and Astrophysics*, 2007, 474(1), 145.

Zechmeister, M. and Kürster, M., "The generalised Lomb-Scargle periodogram: A new formalism for the floating-mean and Keplerian periodograms", *Astronomy & Astrophysics*, 2009, 496(2), 577.

Zhang, D., "A Review of the Theory of Galactic Winds Driven by Stellar Feedback", *Galaxies*, 2018, 6, 114.

Ziolkowski, J., "Determination of the masses of the components of the HDE 226868/Cyg X-1 binary system.", *Monthly Notices of the Royal Astronomical Society*, 2014, 440, L61.

# Appendices

# A   Detrending TESS Data

The *Lightkurve* python package (version 2.3.0), a comprehensive software suite for downloading, extracting, and detrending data from Kepler and TESS. It provides three primary methods for detrending, which may employ TESS CBVs or an equivalent user-defined product.

The *CBVCorrector* class of *Lightkurve* provides a robust and highly streamlined detrending process (see the Lightkurve documentation: `https://docs.lightkurve.org/reference/api/lightkurve.correctors.CBVCorrector.html`). *CBVCorrector* provides the functionality to optimize the CBV amplitudes through L2 regularized fits with a variable tuning parameter and targeted underfitting/overfitting metrics. The overfitting metric measures the full-band power in the power spectrum before and after the detrending is applied; If the power increases as a result of the detrending, it's likely the data was overfit. The underfitting metric measures the correlations between the detrended light curve and the light curves of nearby stars. If the detrending amplitudes were insufficient, there should still exist some CCD or camera-wide trends in the detrended light curve which will yield a correlation with nearby SAP light curves and therefore identify underfitting. Both metrics are tuned such that 0 corresponds to severe underfitting/overfitting, values above 0.8 are considered acceptable, and 1.0 is the maximum and ideal values. The *CBVCorrector* algorithm attempts to optimize the tuning parameter of the L2 regression fit such that it produces acceptable overfitting and underfitting metrics. The two overfitting metrics have the effect of "squeezing" the tuning parameter towards an ideal value, with the overfitting metric acting against a tuning parameter permitting inflated CBV amplitudes and the underfitting metric acting against a tuning parameter forcing the CBV amplitudes to zero.

Fig. A.1 shows the behaviour of the overfitting and underfitting metrics with variable L2-Normalization penalty for the extracted TESS light curve. The underfitting metric demonstrates a weak negative correlation with the L2 tuning parameter, however is at a near-ideal value at all values for the

tuning parameter. The overfitting metric, on the other hand, demonstrates a very strong dependence on tuning parameter. In fact, tuning parameters that produce non-neglegible CBV amplitudes produce severe overfitting. The behaviour of the tuning parameters indicate

1. this light curve is not significantly correlated with the those of nearby stars, and
2. non-neglegible CBV amplitudes introduce additional power into the light curve.

This would seem to indicate the extracted SAP data requires no detrending, which is reflected in Fig. A.2. The *CBVCorrector*-detrended data is essentially identical to the SAP light curve, therefore this detrending method was not used and an analysis of the SAP photometry was included in this work.
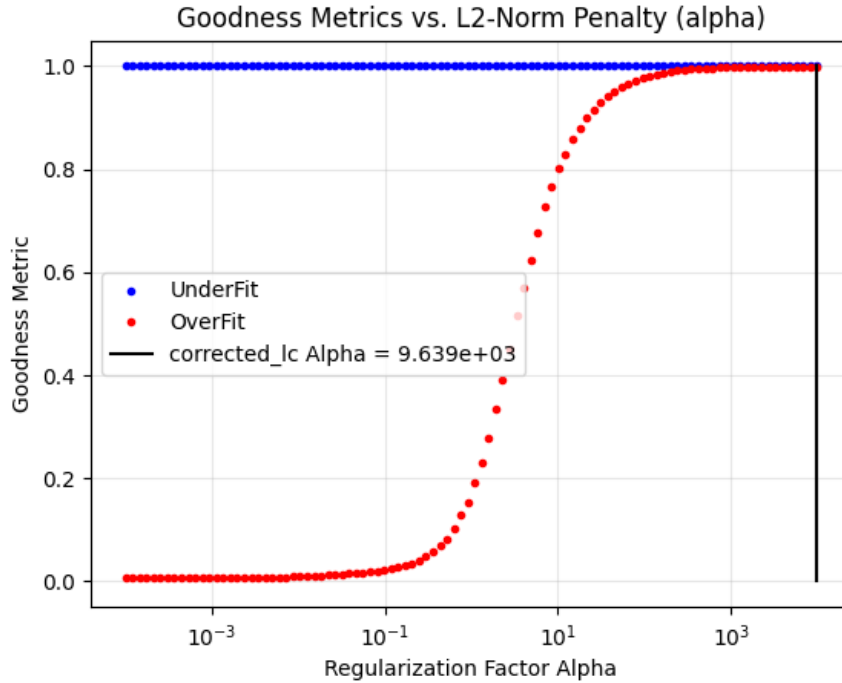


Figure A.1: The response of the overfitting and underfitting metrics with variable L2 tuning parameter when the *CBVCorrector* algorithm is applied to the TESS data.
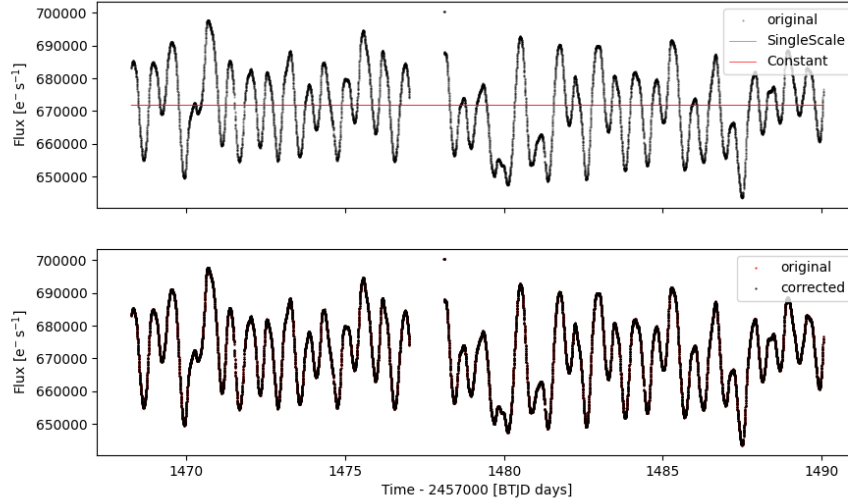
Figure A.2: A diagnostic plot of the detrending of TESS data with *CBVCorrector* using 8 single-scale CBVs as regressors. Top: The amplitude-scaled CBVs plotted over the SAP light curve. Bottom: The detrended data plotted over the original data. The CBV amplitudes here are effectively zero and therefore the data doesn't appear to have been modified by the CBV detrending, in contrast to the detrending with *RegressionCorrector*.

The *RegressionCorrector* class provides another method of detrending TESS and Kepler data. This algorithm performs a linear regression of the light curve against an arbitrary matrix of column vectors. The CBVs can be input as the column vectors, or the user can provide their own trend measurements. This method lacks the protection against overfitting inherent in the *CBVCorrector* algorithm, therefore is at high risk of overfitting. The primary consequence of overfitting is the introduction of noise into the detrended light curve. Depending on the noise characteristics of the regressors, this may or may not be a concern. In the case of single-scale CBVs the injected noise occupies primarily high-frequency bands. These don't overlap with the regions containing variability of interest for Plaskett's Star, therefore this is an acceptable trade-off. Fig. A.3 illustrates the results of performing a *RegressionCorrector* detrending. This is considered the optimal detrending for the research goals of this work.

There is one frequency of interest that may be affected by CBV amplitudes that aren't carefully managed. The orbital period of the system is approximately 14.4 days and photometric variability of $\approx 6$ mmag was detected by (Mahy et al., 2011) and this work in the CoRoT photometry. CBVs are generated on a per-orbit basis and therefore demonstrate quasi-periodicity at $P \approx 13.5$ d and the clear potential to interfere with the orbital modulation. However, the short duration of TESS sectors ($\approx 27$ days) precludes the reliable detection of this frequency on the basis that two cycles would span 28.8 days. Therefore, while the observation of the orbital frequency in the TESS data is an interesting edge case of the CBV detrending process, it's ultimately of minimal scientific value.
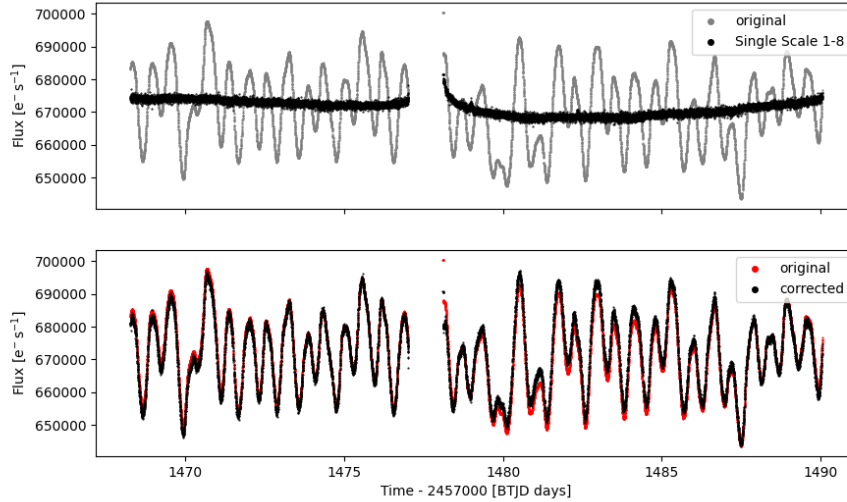


Figure A.3: A diagnostic plot of the detrending of TESS data with *Regression-Corrector* using 8 single-scale CBVs as regressors. Top: The amplitude-scaled CBVs plotted over the SAP light curve. Bottom: The detrended data plotted over the original data.

A detrending using background pixels to develop custom regressors for use with *RegressionCorrector* was considered. This type of detrending is challenging to use with 2-minute cadence data as the TPFs contain too few background pixels and is much more applicable with the 30-minute cadence data and FFIs. For this reason, this type of detrending was not explored.

# B TESS Co-trending Basis Vectors

CBVs are provided individually for each CCDs for every TESS sector and represent systematic trends observed across all targets observed with that camera and CCD. These are provided in the form of sets of pseudo-light curves which demonstrate the same sampling in time as targets observed during their corresponding sector. To detrend a TESS SAP light curve, the CBVs must be appropriately scaled (see App. A). This appendix provides the CBVs which are relevant to the TESS observations of Plaskett's Star. More specifically, Plaskett's Star was observed in sector 6 with CCDs 3 of camera 1.
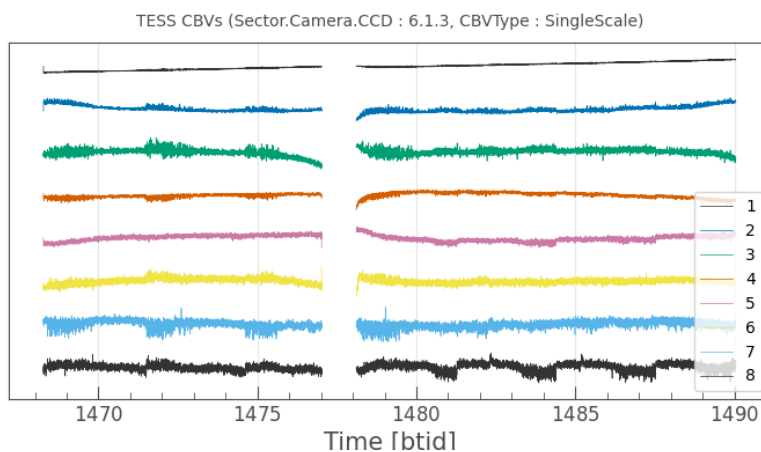


Figure B.1: TESS single-scale CBVs 1-8 for sector 6, camera 1, and CCD 3. These CBVs were used for the TESS light curve extraction.
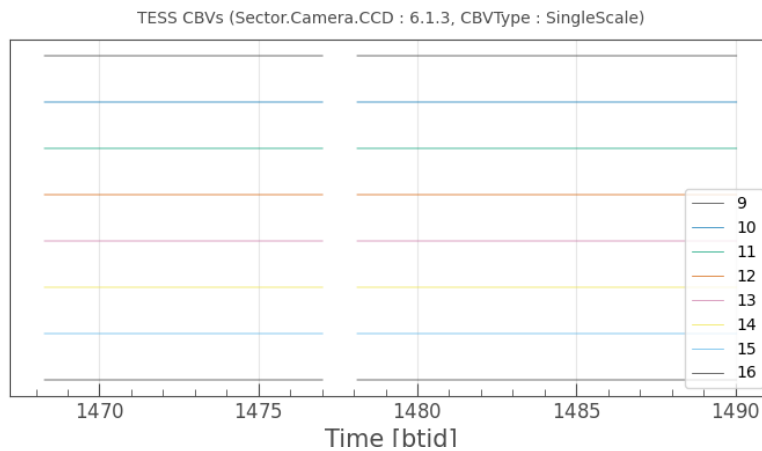
Figure B.2: TESS single-scale CBVs 1-8 for sector 6, camera 1, and CCD 3. These were not used in the data extraction.
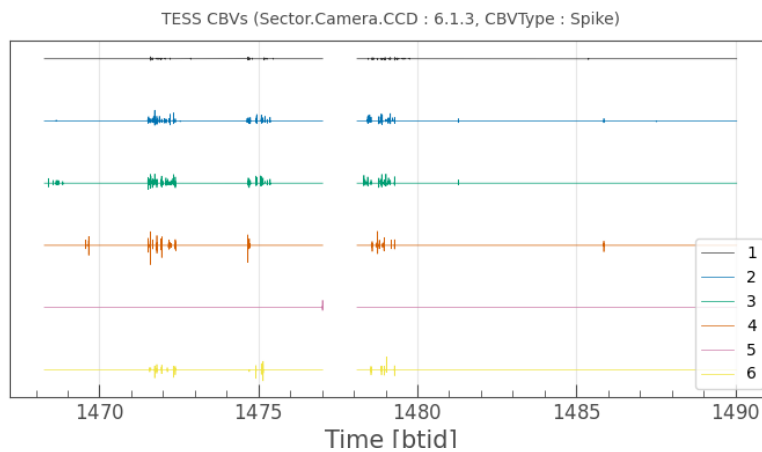


Figure B.3: TESS spike CBVs for sector 6, camera 1, and CCD 3. These were not used in the data extraction as these spike discontinuities did not appear to be present in the SAP light curve.

Figure B.4: TESS multi-scale low-frequency CBVs for sector 6, camera 1, and CCD 3. The single-scale CBVs were used instead of the multi-scale in this work.



Figure B.5: TESS multi-scale medium-frequency CBVs for sector 6, camera 1, and CCD 3. The single-scale CBVs were used instead of the multi-scale in this work.

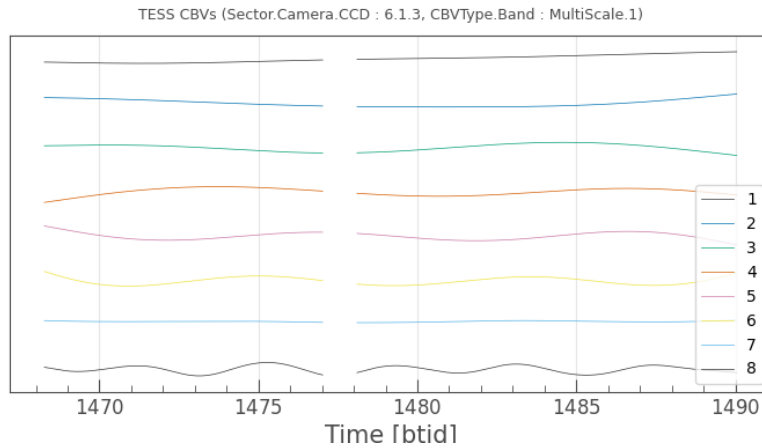TESS CBVs (Sector.Camera.CCD : 6.1.3, CBVType.Band : MultiScale.3)

Figure B.6: TESS multi-scale high-frequency CBVs for sector 6, camera 1, and CCD 3. The single-scale CBVs were used instead of the multi-scale in this work.
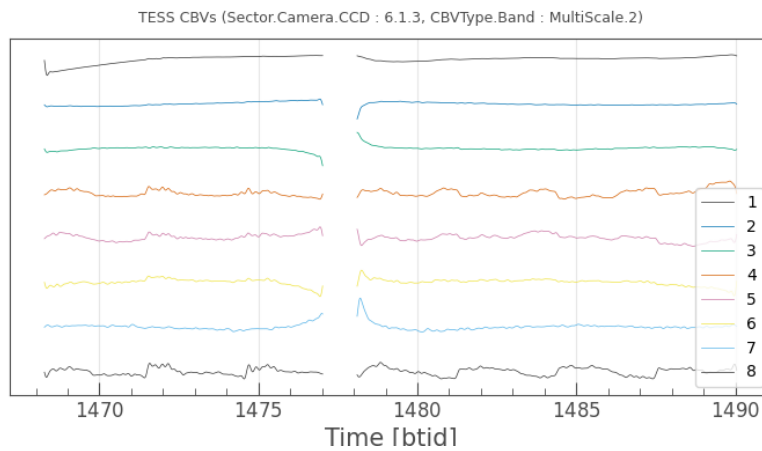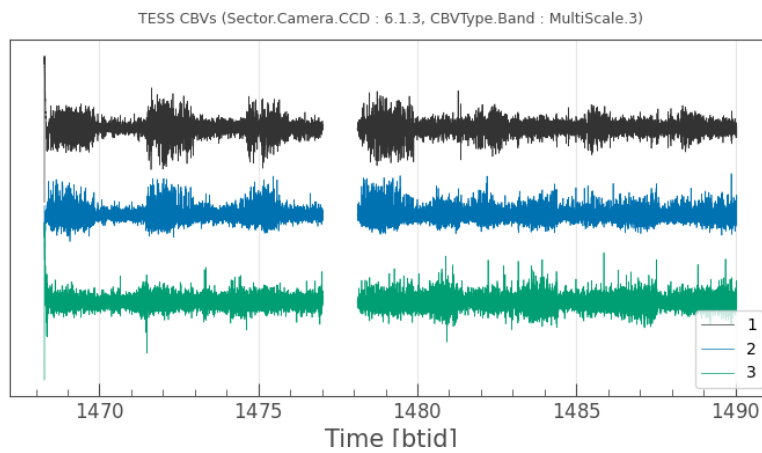
# C   Aperture Masks for TESS Data Extractions

When constructing a light curve for a specific target from a series of CCD images, it is necessary to identify all pixels which are illuminated by that target. If too few pixels are selected, the SNR will be adversely affected. If too many pixels are selected, variability contributions from nearby background sources may be introduced or exacerbated. While there are no bright targets near Plaskett's Star (see Fig. 3.6), the aperture mask is one of the two subjective choices of TESS photometry extraction (the other being the approach to detrending). It was therefore deemed important to explore several aperture masks to examine how the choice of aperture mask affected the frequency analysis results. This appendix presents eight masks which were explored using a fixed 20-frequency pre-whitening with peak selection strictly according to the highest-amplitude criterion. It was found that the results in all cases were nearly identical and well within analytical uncertainties. The aperture mask used in constructing the SAP TESS light curve (and consequently the detrended TESS light curve) is shown in Fig. 3.7.
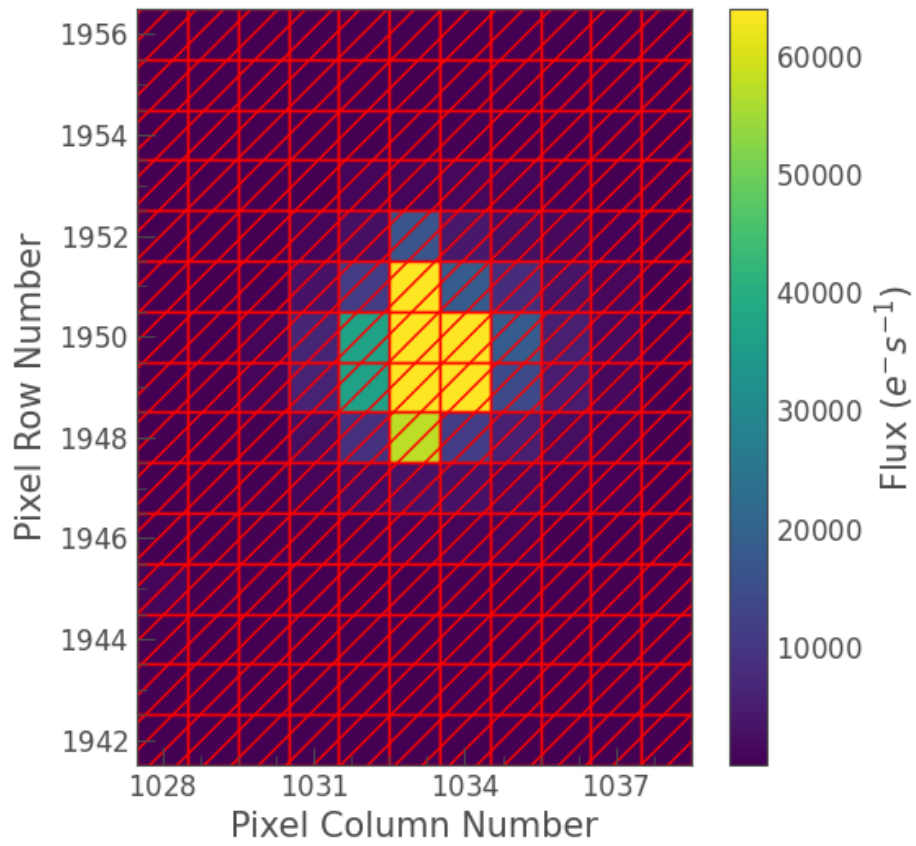
Figure C.1: A mask including all pixels in the TPF
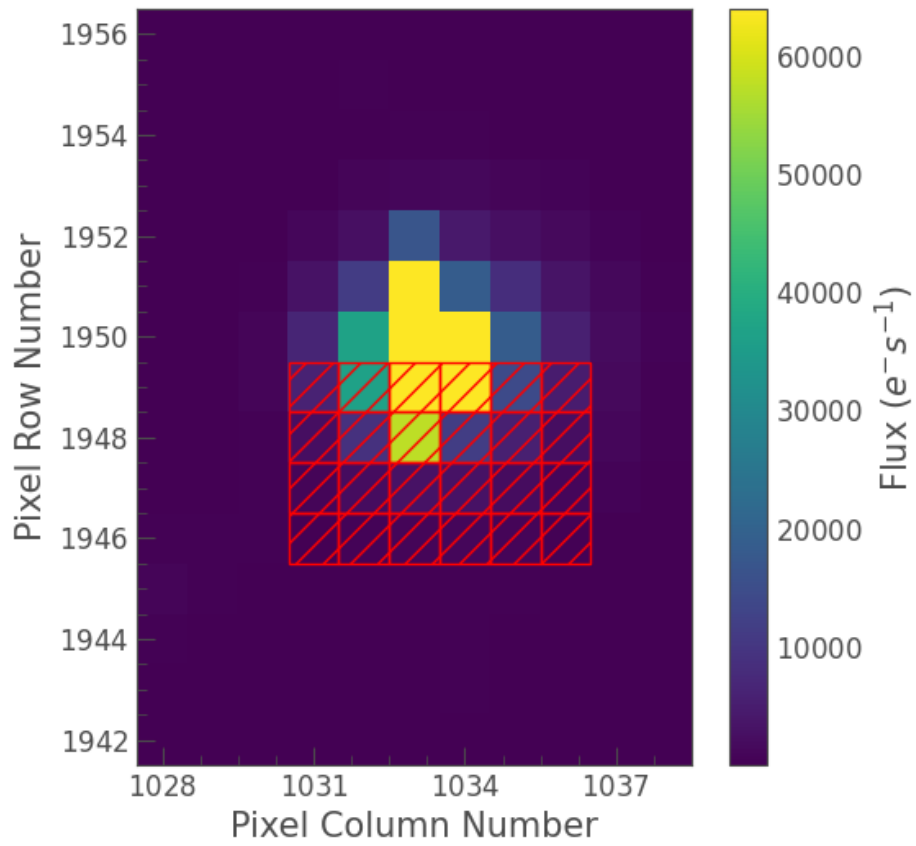
Figure C.2: A mask including the bottom half of the star
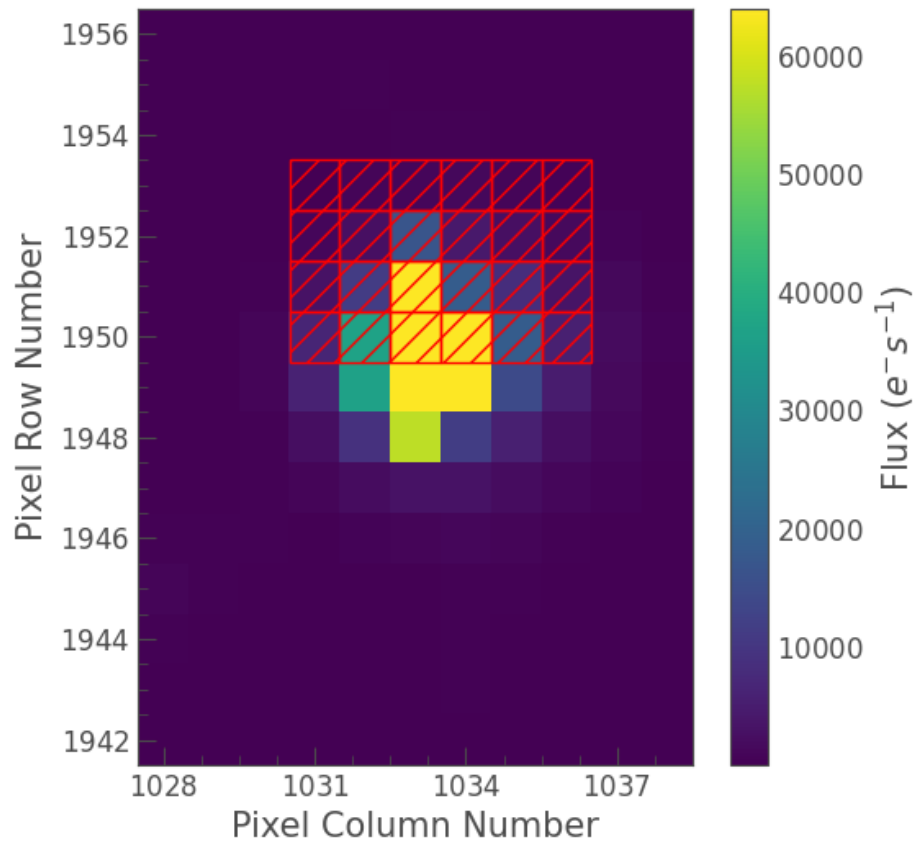
Figure C.3: A mask including the top half of the star
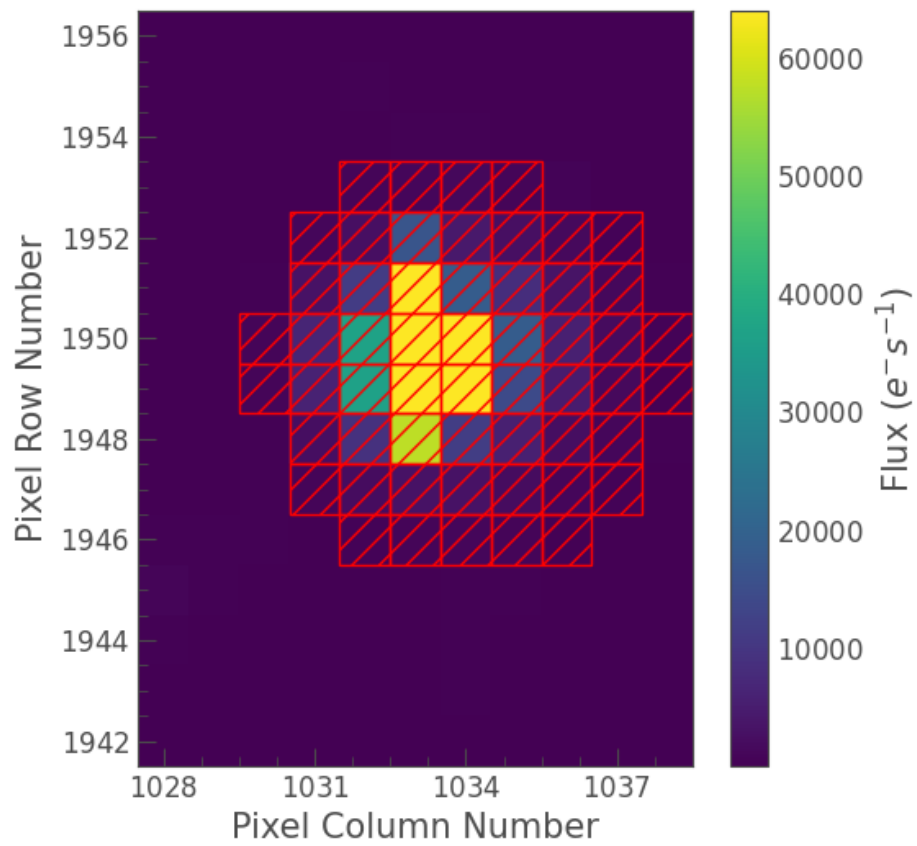
Figure C.4: A mask including all pixels with greater than the average flux of the TPF
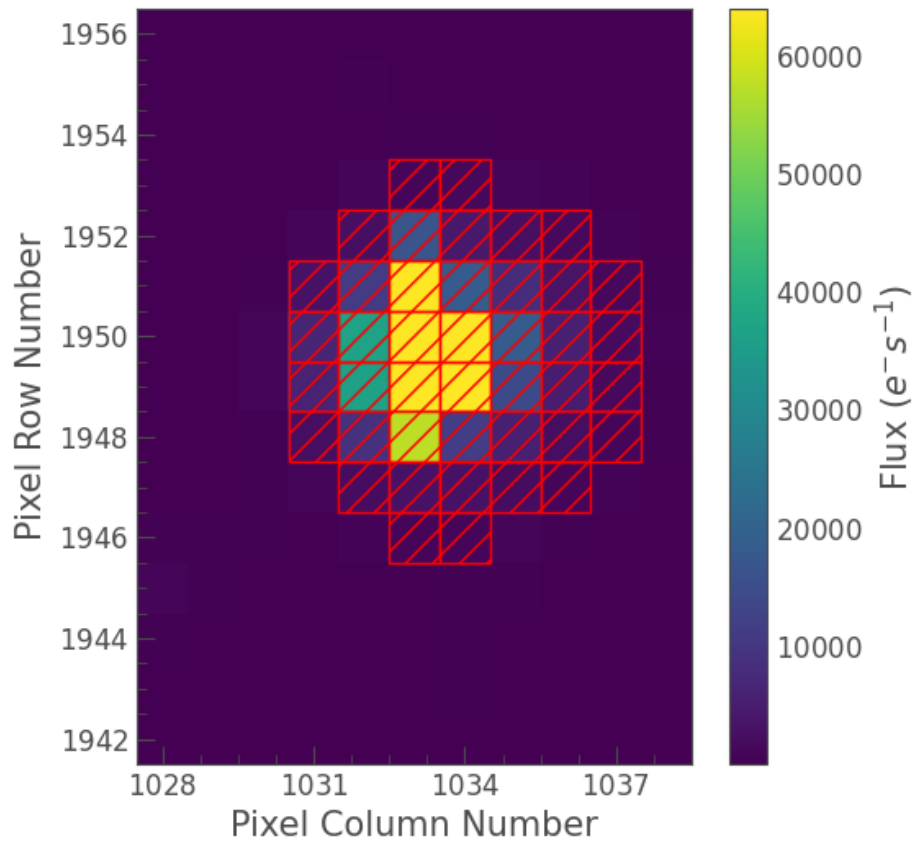
Figure C.5: A mask including all pixels with greater than 3 times the average flux of the TPF
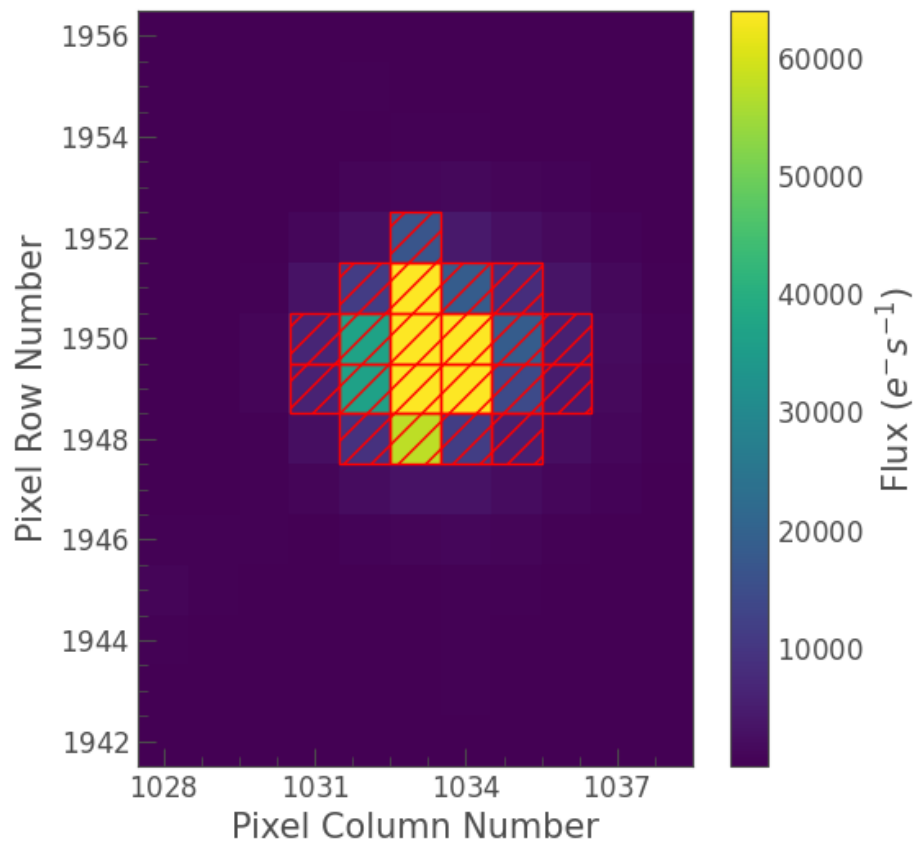
Figure C.6: A mask including all pixels with greater than 15 times the average flux of the TPF
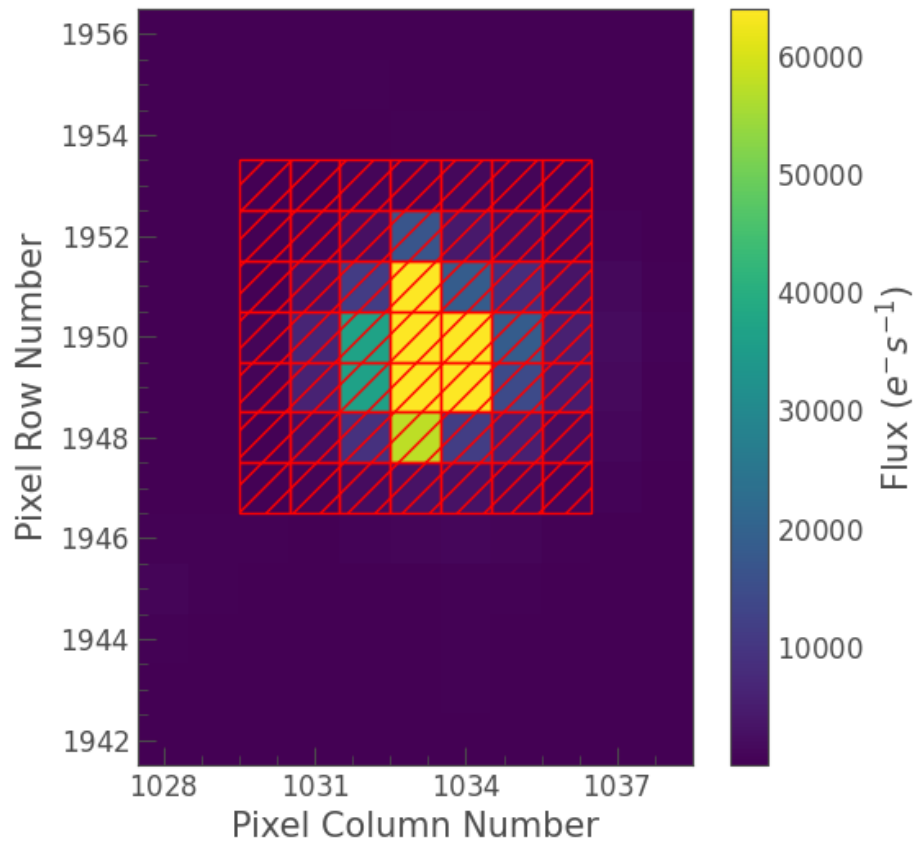
Figure C.7: A broad manually defined mask
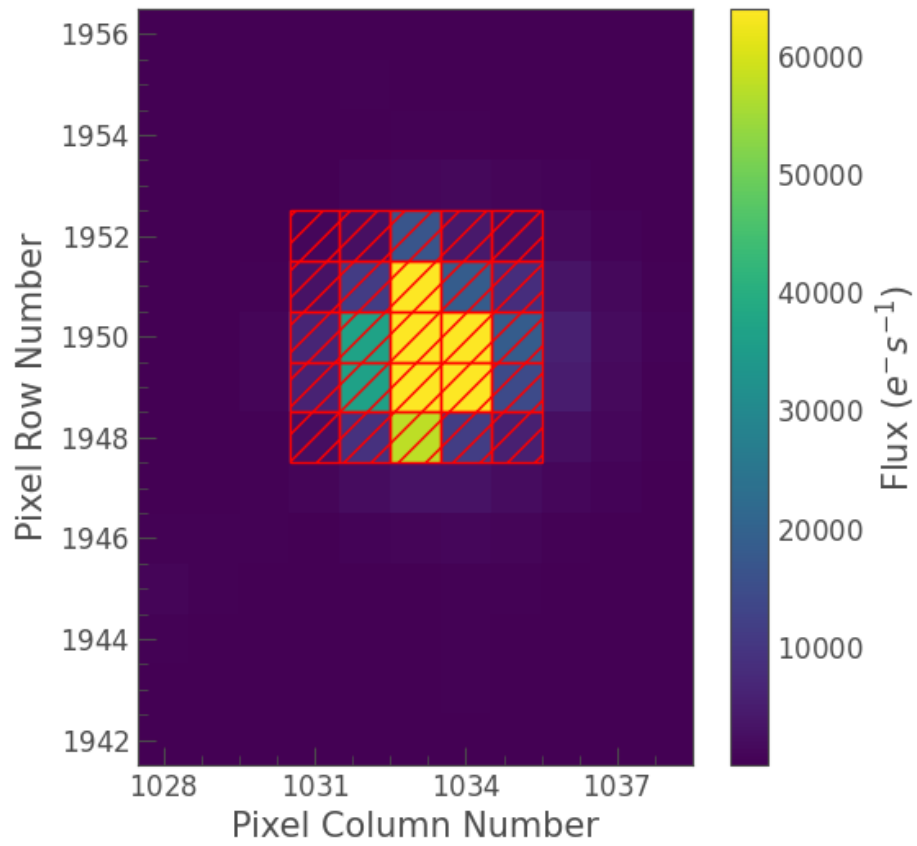
Figure C.8: A tight manually defined mask

# D   Illustration of the Pre-Whitening Process with a Synthetic Light Curve

To demonstrate the pre-whitening process, a sample 2-frequency synthetic light curve was generated using parameters Table D.1 and a sinusoidal variability model (see Eq. 4.15). This was constructed solely of signal (e.g. no synthetic noise is included) and is pictured in Fig. D.1. It's important to remark that a synthetic light curve, with or without added noise, makes a poor benchmark for a LS pre-whitening analysis.

| n | Frequency | Amplitude | Phase |
|---|-----------|-----------|-------|
| 1 | 0.1       | 0.5       | 0.2   |
| 2 | 0.35      | 0.3       | 0.7   |

Table D.1: The input frequencies for the two-frequency demonstration light curve. Each frequency-amplitude-phase set was used to generate a sinusoidal single-frequency model according to Eq. 4.15, and the two single-frequency models were summed to yield the demonstration light curve.
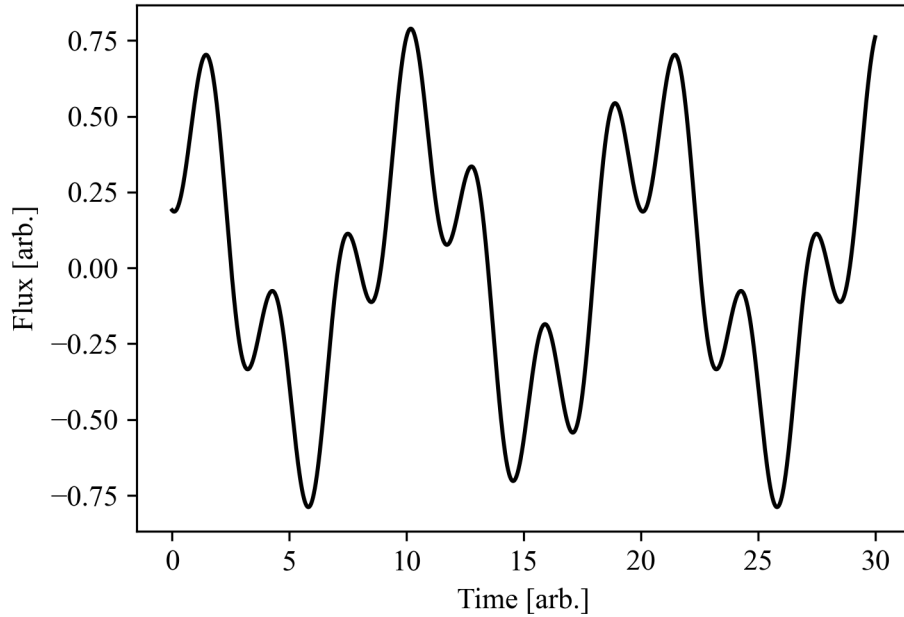
Figure D.1: A synthetic light curve consisting of two summed sinusoids.

## Iteration 1

The first stage of pre-whitening is to compute a LS periodogram and identify the frequency of interest. In this case, the frequency is identified by highest amplitude (Fig. D.2). The second stage is to perform a single-frequency fit on the light curve (Fig. D.3). The third stage is a multi-frequency fit, however this is equivalent to the single-frequency fit on the first iteration. The fourth stage of each iteration is to compute a residual light curve by subtracting the single-frequency fit (Fig. D.4)
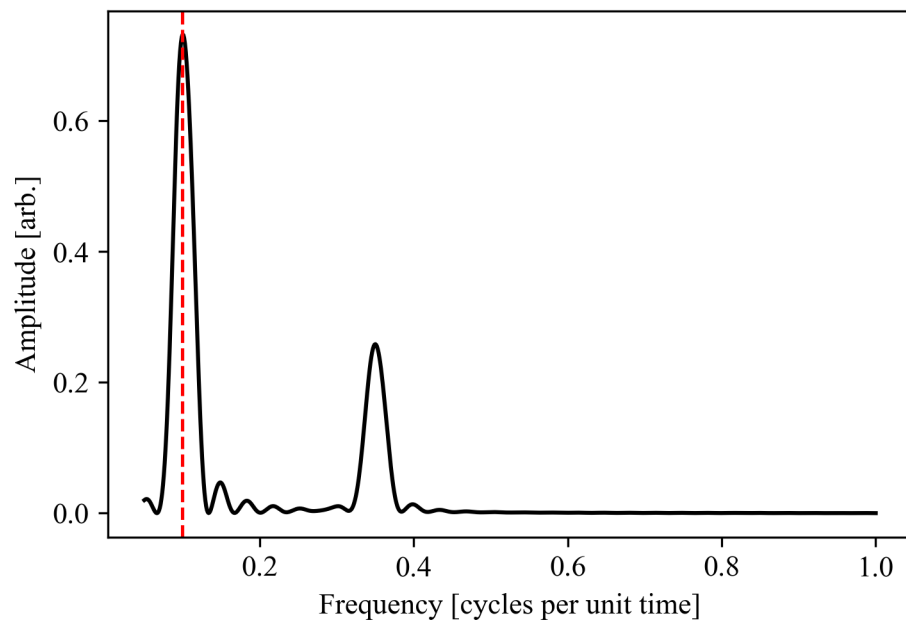
Figure D.2: A periodogram computed for the synthetic light curve in Fig. D.1
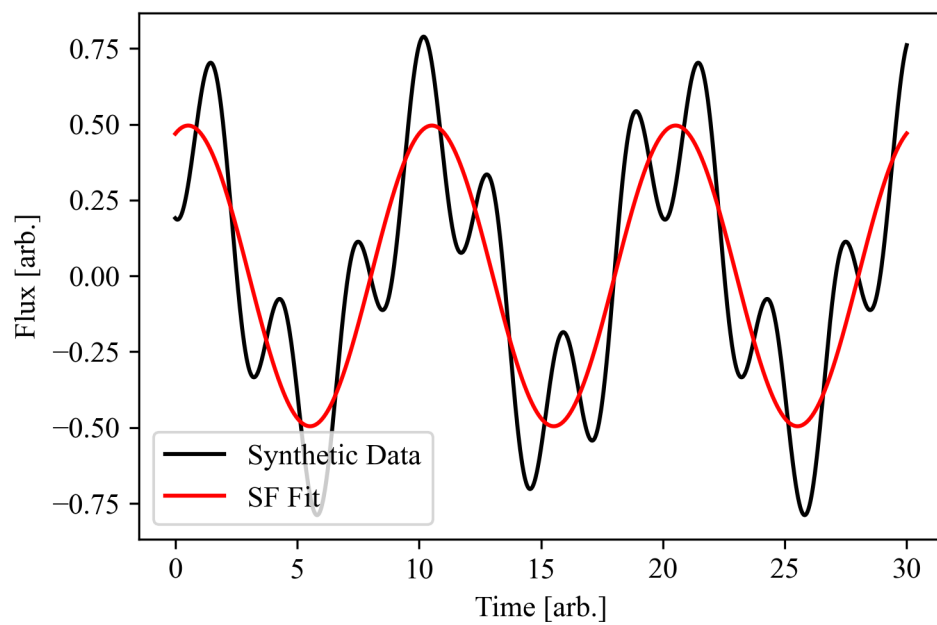
Figure D.3: A single-frequency optimized model plotted over the synthetic light curve for the first iteration.
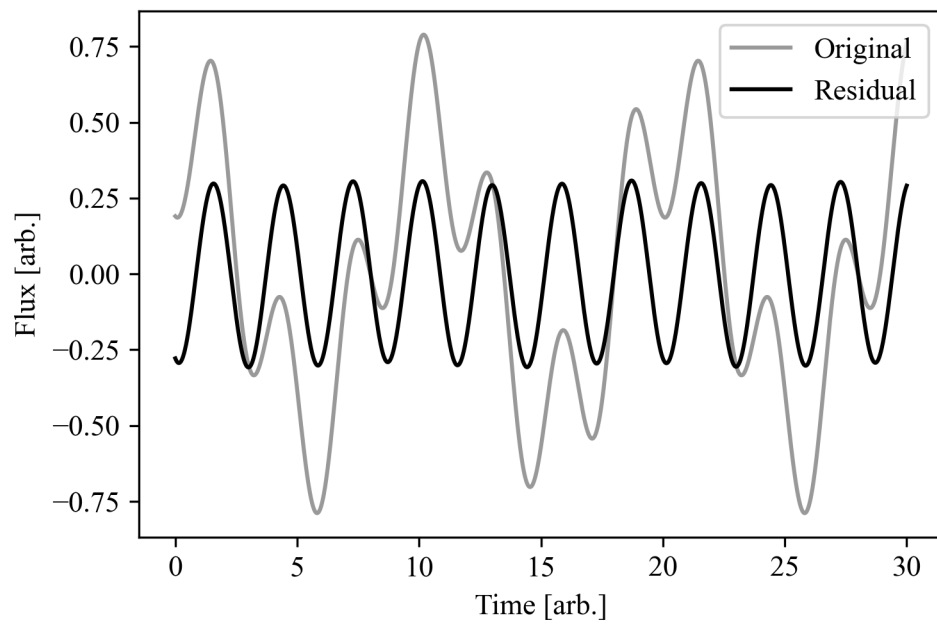
Figure D.4: The residual synthetic light curve after subtracting the first single-frequency model

## Iteration 2

The second iteration operates primarily on the residual light curve and its periodogram. Again, the first stage computes a periodogram and identifies the highest (and only remaining, in this case) frequency (Fig. D.5) The single-frequency optimization is performed on the residual light curve (Fig. D.6). The third stage, which was skipped in the first iteration, conducts a multi-frequency optimization on the original light curve (Fig. D.7). As illustrated by the perfect fit of the multi-frequency variability model, both periodic components have been extracted and the pre-whitening is complete. The parameters measured by pre-whitening are identical to the parameters used to generate the initial light curve, given in Table D.1, to at least 9 decimal places.
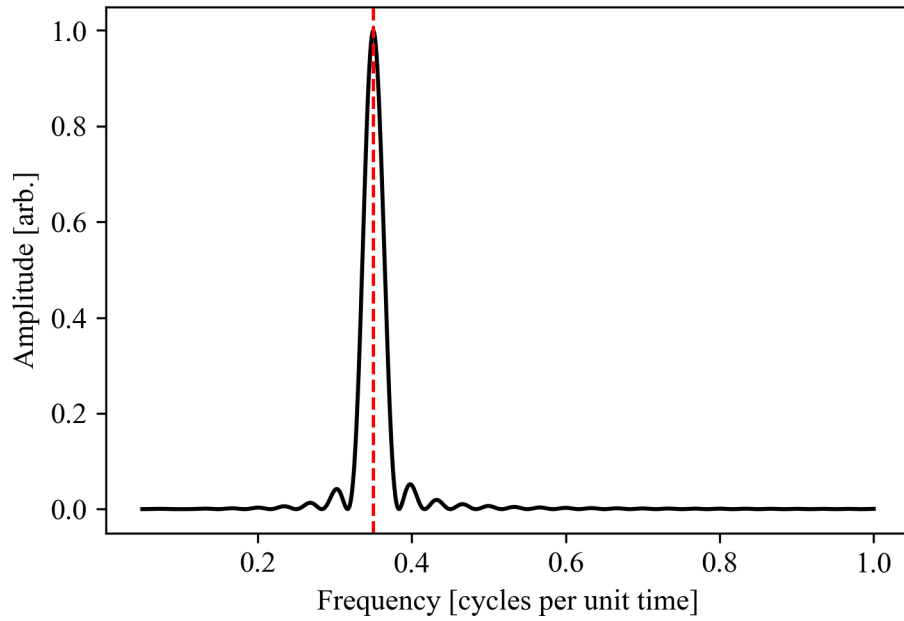


Figure D.5: The residual periodogram with the highest frequency identified.
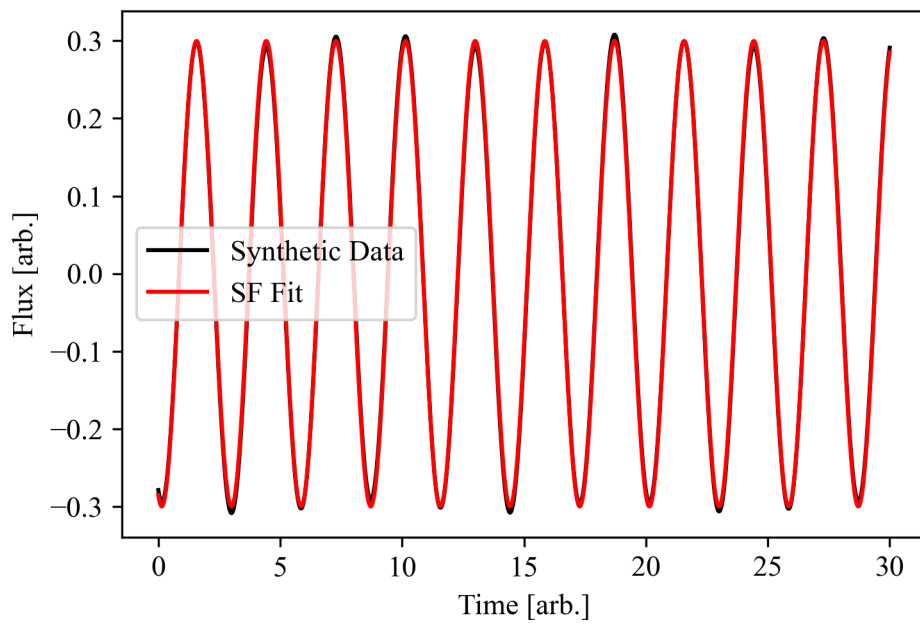
Figure D.6: A single-frequency optimized model plotted over the residual synthetic light curve for the second iteration.
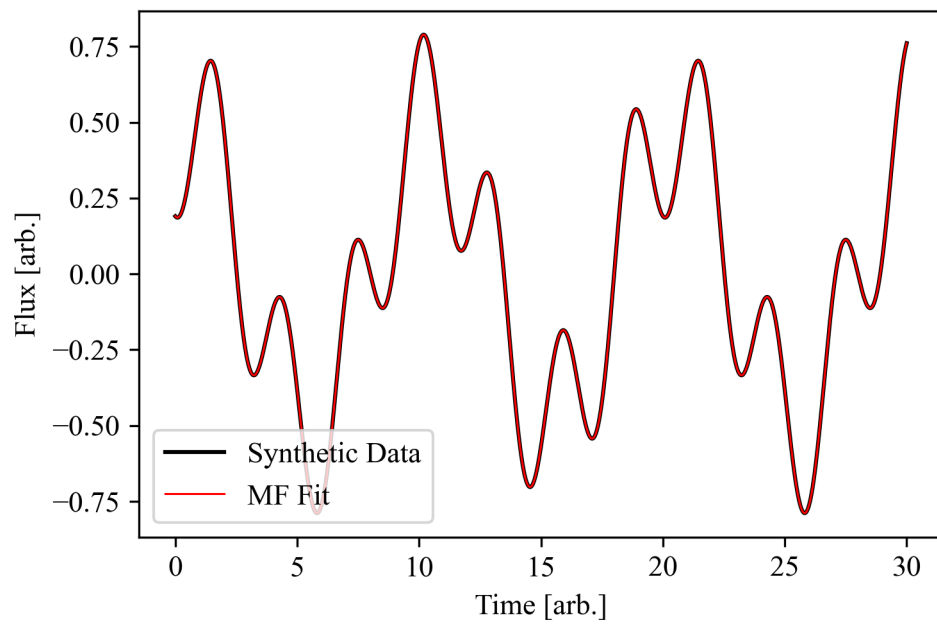
Figure D.7: A multi-frequency optimized model (complete variability model) plotted over the synthetic light curve for the second iteration.

# E  Full Frequency Lists

When conducting frequency analysis through pre-whitening, it is common to detect frequencies which are determined to be statistically insignificant at the conclusion of the analysis. The ratio of significant to insignificant frequencies is generally dependent on the approach and implementation to the frequency analysis. For example, approximately 72% of the frequencies identified in the CoRoT photometry of Plaskett's Star by Mahy et al. (2011) were found to be statistically insignificant. This work placed specific focus on minimizing the number of extracted frequencies which are not reasonably expected to be significant on the basis that estimates of analytical uncertainties are dependent on the residual light curve. Nevertheless, all three datasets analyzed in this work yielded frequencies which were determined to be statistically significant. The full lists of frequencies, including both significant and insignificant results, are shown for the TESS SAP, detrended TESS, and CoRoT data in Table E.1, Table E.2, and Table E.3 respectively.

| Index | Frequency [c/d] | Amplitude [mmag] | Phase | Sig. (SLF) | Sig. (Avg.) | Remarks |
|---|---|---|---|---|---|---|
| 1 | 1.64543(29) | 17.56(19) | 0.623(11) | 21.69 | 19.29 | $2f_{\rm rot,BLC}$ |
| 2 | 0.80902(45) | 11.34(20) | 0.839(17) | 12.7 | 13.9 | $f_{\rm rot,BLC}$ |
| 3 | 0.63516(84) | 6.14(20) | 0.020(32) | 6.85 | 8.6 | |
| 4 | 0.13872(88) | 5.81(20) | 0.652(34) | 6.49 | 7.8 | $2f_{\rm orb}$? |
| 5 | 1.1042(11) | 4.64(20) | 0.181(43) | 5.22 | 4.54 | |
| 6 | 0.7132(10) | 4.95(20) | 0.953(40) | 5.52 | 6.79 | |
| 7 | 0.2855(13) | 3.82(20) | 0.846(53) | 4.26 | 5.19 | $4f_{\rm orb}$? |
| 8 | 0.3910(14) | 3.49(20) | 0.854(58) | 3.89 | 5.21 | $6f_{\rm orb}$? |
| 9 | 0.4411(17) | 3.01(20) | 0.499(67) | 3.36 | 4.21 | |
| 10 | 0.8701(17) | 3.02(20) | 0.035(67) | 3.38 | 3.51 | |
| 11 | 3.2940(23) | 2.17(20) | 0.918(93) | 14.72 | 12.3 | $4f_{\rm rot,BLC}$ |
| 12 | 2.4631(24) | 2.14(20) | 0.093(94) | 5.11 | 5.45 | $3f_{\rm rot,BLC}$ |
| 13 | 4.9393(73) | 0.70(20) | 0.88(28) | 11.43 | 9.62 | $6f_{\rm rot,BLC}$ |
| 14 | 5.763(12) | 0.42(20) | 0.26(48) | 7.51 | 7.09 | $7f_{\rm rot,BLC}$ |
| 15 | 4.098(13) | 0.37(20) | 0.43(54) | 4.71 | 3.69 | $5f_{\rm rot,BLC}$ |
| 16 | 4.148(17) | 0.30(20) | 0.04(67) | 3.85 | 3.16 | Assoc. $f_{15}$ |
| 17 | 3.804(16) | 0.31(20) | 0.68(65) | 3.29 | 2.69 | |
| 18 | 5.073(23) | 0.22(20) | 0.72(91) | 3.71 | 3.3 | |
| 19 | 7.397(26) | 0.19(20) | 0.463(48) | 3.61 | 3.66 | $9f_{\rm rot,BLC}$ |
| 20 | 9.056(27) | 0.19(20) | 0.442(89) | 3.51 | 6.89 | $11f_{\rm rot,BLC}$ |

Table E.1: The full list of significant and insignificant frequencies extracted from the detrended TESS data.

| Index | Frequency [c/d] | Amplitude [mmag] | Phase | Sig. (SLF) | Sig. (Avg.) | Remarks |
|---|---|---|---|---|---|---|
| 1 | 1.64551(61) | 17.45(41) | 0.621(24) | 20.86 | 19.45 | $2f_{\rm rot,BLC}$ |
| 2 | 0.81054(94) | 11.40(41) | 0.814(36) | 11.92 | 11.98 | $f_{\rm rot,BLC}$ |
| 3 | 0.6329(17) | 6.05(42) | 0.066(69) | 6.29 | 7.09 | |
| 4 | 0.1407(16) | 6.41(42) | 0.617(65) | 6.66 | 6.67 | $2f_{\rm orb}$? |
| 5 | 0.0505(21) | 5.06(42) | 0.572(83) | 5.26 | 5.19 | $f_{\rm orb}$? |
| 6 | 1.1048(24) | 4.43(42) | 0.174(95) | 4.68 | 4.47 | |
| 7 | 0.7128(24) | 4.35(42) | 0.951(97) | 4.52 | 4.92 | |
| 8 | 0.2861(27) | 3.92(42) | 0.80(10) | 4.08 | 4.61 | $4f_{\rm orb}$? |
| 9 | 0.3982(31) | 3.40(42) | 0.77(12) | 3.53 | 4.44 | $6f_{\rm orb}$? |
| 10 | 0.8740(33) | 3.26(42) | 0.98(12) | 3.4 | 3.33 | |
| 11 | 2.4626(47) | 2.26(42) | 0.10(18) | 5.47 | 5.75 | $3f_{\rm rot,BLC}$ |
| 12 | 3.2942(48) | 2.22(42) | 0.92(19) | 14.11 | 12.3 | $4f_{\rm rot,BLC}$ |
| 13 | 4.940(16) | 0.64(42) | 0.86(66) | 9.12 | 8.02 | $6f_{\rm rot,BLC}$ |
| 14 | 5.764(24) | 0.44(42) | 0.25(95) | 6.99 | 6.2 | $7f_{\rm rot,BLC}$ |
| 15 | 4.108(29) | 0.36(42) | 0.32(17) | 4.04 | 2.77 | $5f_{\rm rot,BLC}$ |
| 16 | 5.002(41) | 0.26(42) | 0.86(61) | 3.79 | 3.52 | Assoc. $f_{13}$ |
| 17 | 7.398(54) | 0.20(42) | 0.45(12) | 3.31 | 4.27 | $8f_{\rm rot,BLC}$ |

Table E.2: The full list of significant and insignificant frequencies extracted from the SAP TESS data.

| Index | Frequency [c/d] | Amplitude [mmag] | Phase | Sig. (SLF) | Sig. (Avg.) | Remarks |
|---|---|---|---|---|---|---|
| 1 | 1.64586(51) | 15.33(48) | 0.124(32) | 22.15 | 20.71 | $2f_{\rm rot,BLC}$ |
| 2 | 0.81992(70) | 11.26(49) | 0.925(43) | 9.77 | 9.46 | $f_{\rm rot,BLC}$ |
| 3 | 0.0699(12) | 6.54(49) | 0.356(75) | 5.46 | 5.48 | $f_{\rm orb}$ |
| 4 | 0.3957(21) | 3.77(49) | 0.53(13) | 3.14 | 3.2 | |
| 5 | 0.6494(21) | 3.74(49) | 0.48(13) | 3.16 | 3.23 | |
| 6 | 0.1467(21) | 3.64(49) | 0.32(13) | 3.04 | 2.88 | $2f_{\rm orb}$ |
| 7 | 0.3653(16) | 4.82(49) | 0.69(10) | 4.02 | 4.09 | |
| 8 | 0.9335(24) | 3.31(49) | 0.51(14) | 2.93 | 2.68 | |
| 9 | 2.4663(25) | 3.11(49) | 0.72(15) | 12.14 | 12.04 | $3f_{\rm rot,BLC}$ |
| 10 | 0.8923(26) | 2.98(49) | 0.76(16) | 2.61 | 2.4 | |
| 11 | 3.2920(56) | 1.42(49) | 0.95(34) | 12.64 | 8.7 | $4f_{\rm rot,BLC}$ |
| 12 | 5.763(14) | 0.55(49) | 0.95(90) | 11.58 | 9.8 | $7f_{\rm rot,BLC}$ |
| 13 | 4.106(19) | 0.42(49) | 0.07(19) | 6.01 | 4.75 | $5f_{\rm rot,BLC}$ |
| 14 | 3.309(14) | 0.54(49) | 0.18(92) | 4.84 | 3.32 | Assoc. $f_{11}$ |
| 15 | 4.939(25) | 0.31(49) | 0.48(60) | 5.79 | 5.33 | $6f_{\rm rot,BLC}$ |
| 16 | 3.971(31) | 0.25(49) | 0.23(98) | 3.39 | 2.69 | |
| 17 | 4.504(35) | 0.22(49) | 0.37(20) | 3.75 | 3.31 | |
| 18 | 4.711(37) | 0.21(49) | 0.31(36) | 3.72 | 3.05 | |
| 19 | 4.883(45) | 0.17(49) | 0.44(86) | 3.2 | 2.93 | |
| 20 | 6.589(51) | 0.16(49) | 0.36(18) | 3.54 | 4.2 | $8f_{\rm rot,BLC}$ |
| 21 | 8.226(63) | 0.12(49) | 0.04(98) | 2.98 | 4.25 | $10f_{\rm rot,BLC}$ |
| 22 | 7.408(63) | 0.12(49) | 0.37(97) | 2.93 | 3.74 | $9f_{\rm rot,BLC}$ |

Table E.3: The full list of significant and insignificant frequencies extracted from the CoRoT data.

# F   Radial Velocities from Disentangled ESPaDOnS Spectra

Radial velocities from a sample of 27 spectra collected with ESPaDOnS and first analyzed in Grunhut et al. (2022) were disentangled to yield measurements of radial velocity for both the BLC and NLC. This work was performed by Dr. Oleg Kochukhov using the methodology described in Folsom et al. (2010) and he kindly provided the radial velocity measurements detailed in the following five tables for the comparison with the photometric data, the results of which are described in Sect. 6.1. The disentangling was independently conducted for each of the 4026 Å, 4200 Å, 4542 Å, and 5411 Ålines. Table F.5 gives the average radial velocity for each time stamp, with the uncertainty taken to be the standard deviation of the measurements for the individual lines.

| HJD | $V_{\rm r,BLC}$ | $V_{\rm r,NLC}$ |
| --- | --- | --- |
| | [km/s] | [km/s] |
| 2455961.8587 | -1.26 | 178.11 |
| 2455966.8770 | 0.25 | -14.86 |
| 2455967.7681 | -0.87 | -105.98 |
| 2455969.7754 | 0.25 | -211.60 |
| 2456000.4172 | 20.41 | -163.88 |
| 2456001.3654 | 1.31 | -97.25 |
| 2456010.3588 | -6.85 | -33.66 |
| 2456012.3442 | -2.01 | -178.00 |
| 2456196.0910 | 0.91 | 90.01 |
| 2456198.0940 | -0.49 | -110.98 |
| 2456199.0822 | -0.11 | -163.01 |
| 2456202.1011 | 1.32 | -160.40 |
| 2456261.1258 | 0.78 | -59.42 |
| 2456262.0667 | -0.23 | 28.50 |
| 2456264.1275 | -1.16 | 177.69 |
| 2456272.1203 | -0.08 | -207.27 |
| 2456282.9362 | 0.52 | 30.85 |
| 2456284.1161 | 0.92 | -79.74 |
| 2456288.0983 | 0.92 | -196.00 |
| 2456289.1047 | 1.21 | -116.53 |
| 2456289.9822 | 0.06 | -55.48 |
| 2456343.8555 | 0.50 | -206.49 |
| 2456351.8749 | 0.50 | 203.03 |
| 2456352.9186 | -0.63 | 173.30 |
| 2456353.9110 | -0.34 | 106.61 |
| 2456354.7520 | -0.71 | 33.52 |
| 2456355.8974 | -0.23 | -44.20 |

Table F.1: Radial velocities measured from the ESPaDOnS spectra for the He II 4026 Å line.

| HJD | $V_{\mathrm{r,BLC}}$ [km/s] | $V_{\mathrm{r,NLC}}$ [km/s] |
|---|---|---|
| 2455961.8587 | -0.77 | 178.00 |
| 2455966.8770 | -0.72 | -18.95 |
| 2455967.7681 | -0.78 | -105.52 |
| 2455969.7754 | -0.27 | -208.09 |
| 2456000.4172 | -1.33 | -160.69 |
| 2456001.3654 | 0.21 | -96.29 |
| 2456010.3588 | 0.75 | -38.58 |
| 2456012.3442 | -0.47 | -177.12 |
| 2456196.0910 | -1.45 | 85.13 |
| 2456198.0940 | 0.25 | -109.96 |
| 2456199.0822 | 0.43 | -159.17 |
| 2456202.1011 | 0.30 | -159.29 |
| 2456261.1258 | 0.97 | -55.06 |
| 2456262.0667 | 0.05 | 28.89 |
| 2456264.1275 | -0.24 | 177.71 |
| 2456272.1203 | 0.53 | -203.41 |
| 2456282.9362 | 0.44 | 29.61 |
| 2456284.1161 | 0.99 | -77.11 |
| 2456288.0983 | 0.34 | -191.37 |
| 2456289.1047 | -0.87 | -121.42 |
| 2456289.9822 | -0.07 | -47.93 |
| 2456343.8555 | 0.24 | -205.33 |
| 2456351.8749 | -0.29 | 202.89 |
| 2456352.9186 | 0.02 | 173.57 |
| 2456353.9110 | 0.45 | 114.07 |
| 2456354.7520 | 0.12 | 25.34 |
| 2456355.8974 | -0.08 | -43.91 |

Table F.2: Radial velocities measured from the ESPaDOnS spectra for the He II 4200 Å line.

| HJD | $V_{\mathrm{r,BLC}}$ [km/s] | $V_{\mathrm{r,NLC}}$ [km/s] |
|---|---|---|
| 2455961.8587 | 3.66 | 178.10 |
| 2455966.8770 | 1.10 | -19.93 |
| 2455967.7681 | 0.16 | -104.82 |
| 2455969.7754 | -0.10 | -210.72 |
| 2456000.4172 | 0.86 | -164.92 |
| 2456001.3654 | 0.36 | -100.97 |
| 2456010.3588 | 2.21 | -36.69 |
| 2456012.3442 | 8.10 | -180.01 |
| 2456196.0910 | -8.10 | 88.76 |
| 2456198.0940 | -0.25 | -108.96 |
| 2456199.0822 | 0.87 | -158.69 |
| 2456202.1011 | -1.23 | -157.68 |
| 2456261.1258 | 0.44 | -64.01 |
| 2456262.0667 | 1.73 | 23.68 |
| 2456264.1275 | -7.17 | 178.14 |
| 2456272.1203 | 0.87 | -204.96 |
| 2456282.9362 | 0.40 | 29.20 |
| 2456284.1161 | 2.20 | -75.39 |
| 2456288.0983 | 0.80 | -192.81 |
| 2456289.1047 | 0.10 | -125.24 |
| 2456289.9822 | -1.04 | -57.44 |
| 2456343.8555 | -3.08 | -205.60 |
| 2456351.8749 | -1.20 | 205.74 |
| 2456352.9186 | -2.61 | 174.12 |
| 2456353.9110 | -0.08 | 113.50 |
| 2456354.7520 | -0.23 | 31.45 |
| 2456355.8974 | -0.04 | -46.54 |

Table F.3: Radial velocities measured from the ESPaDOnS spectra for the He II 4542 Å line.

| HJD | $V_{\mathrm{r,BLC}}$ | $V_{\mathrm{r,NLC}}$ |
|---|---|---|
| | [km/s] | [km/s] |
| 2455961.8587 | 1.21 | 176.50 |
| 2455966.8770 | -1.12 | -20.35 |
| 2455967.7681 | -0.06 | -104.36 |
| 2455969.7754 | 0.05 | -211.58 |
| 2456000.4172 | -8.69 | -160.18 |
| 2456001.3654 | -0.45 | -96.20 |
| 2456010.3588 | 3.52 | -36.46 |
| 2456012.3442 | -1.33 | -177.05 |
| 2456196.0910 | -2.04 | 85.77 |
| 2456198.0940 | -0.54 | -115.60 |
| 2456199.0822 | 2.04 | -155.98 |
| 2456202.1011 | -1.23 | -152.19 |
| 2456261.1258 | 2.77 | -57.80 |
| 2456262.0667 | 3.42 | 27.66 |
| 2456264.1275 | -3.87 | 182.49 |
| 2456272.1203 | -2.18 | -202.94 |
| 2456282.9362 | -1.28 | 30.29 |
| 2456284.1161 | 2.34 | -77.86 |
| 2456288.0983 | 0.39 | -191.83 |
| 2456289.1047 | 0.84 | -122.36 |
| 2456289.9822 | 4.40 | -47.90 |
| 2456343.8555 | -10.62 | -200.93 |
| 2456351.8749 | -1.54 | 202.66 |
| 2456352.9186 | -1.37 | 171.93 |
| 2456353.9110 | 0.15 | 112.99 |
| 2456354.7520 | -0.15 | 19.01 |
| 2456355.8974 | 0.02 | -46.78 |

Table F.4: Radial velocities measured from the ESPaDOnS spectra for the He II 5411 Å line.

| HJD | $V_{\rm r,NLC}$ [km/s] | $V_{\rm r,BLC}$ [km/s] |
|---|---|---|
| 2455961.8587 | $177.68 \pm 0.68$ | $0.710 \pm 1.94$ |
| 2455966.8770 | $-18.52 \pm 2.17$ | $-0.12 \pm 0.87$ |
| 2455967.7681 | $-105.17 \pm 0.62$ | $-0.39 \pm 0.45$ |
| 2455969.7754 | $-210.50 \pm 1.44$ | $-0.02 \pm 0.19$ |
| 2456000.4172 | $-162.42 \pm 2.02$ | $2.81 \pm 1.76$ |
| 2456001.3654 | $-97.68 \pm 1.94$ | $0.35 \pm 0.63$ |
| 2456010.3588 | $-36.35 \pm 1.75$ | $-0.09 \pm 4.02$ |
| 2456012.3442 | $-178.55 \pm 1.46$ | $1.07 \pm 4.09$ |
| 2456196.0910 | $87.42 \pm 2.03$ | $-2.67 \pm 3.32$ |
| 2456198.0940 | $-111.37 \pm 2.54$ | $-0.26 \pm 0.31$ |
| 2456199.0822 | $-159.24 \pm 2.54$ | $0.81 \pm 0.79$ |
| 2456202.1011 | $-157.37 \pm 3.18$ | $-0.21 \pm 1.08$ |
| 2456261.1258 | $-59.07 \pm 3.25$ | $1.24 \pm 0.90$ |
| 2456262.0667 | $27.18 \pm 2.07$ | $1.25 \pm 1.46$ |
| 2456264.1275 | $179.01 \pm 2.02$ | $-3.11 \pm 2.70$ |
| 2456272.1203 | $-204.64 \pm 1.69$ | $-0.22 \pm 1.18$ |
| 2456282.9362 | $29.99 \pm 0.63$ | $0.02 \pm 0.75$ |
| 2456284.1161 | $-77.52 \pm 1.56$ | $1.61 \pm 0.66$ |
| 2456288.0983 | $-193.00 \pm 1.81$ | $0.61 \pm 0.25$ |
| 2456289.1047 | $-121.39 \pm 3.14$ | $0.32 \pm 0.79$ |
| 2456289.9822 | $-52.19 \pm 4.33$ | $0.84 \pm 2.01$ |
| 2456343.8555 | $-204.59 \pm 2.15$ | $-3.24 \pm 4.49$ |
| 2456351.8749 | $203.56 \pm 1.27$ | $-0.63 \pm 0.80$ |
| 2456352.9186 | $173.23 \pm 0.80$ | $-1.15 \pm 0.98$ |
| 2456353.9110 | $111.79 \pm 3.02$ | $0.05 \pm 0.29$ |
| 2456354.7520 | $27.33 \pm 5.67$ | $-0.24 \pm 0.30$ |
| 2456355.8974 | $-45.36 \pm 1.31$ | $-0.08 \pm 0.09$ |

Table F.5: The averaged radial velocities from the ESPaDOnS spectra.